The Hong Kong Polytechnic University

Department of Industrial and Systems Engineering

Microstructural Dependence of Magnetic Properties of Nd-based Bulk Metallic Glasses

Yong HU

A thesis submitted in partial fulfillment of the requirements for the degree of Doctor of Philosophy

October 2008

DECLARATION

I hereby declare that this thesis is my own work and that, to the best of my knowledge and belief, it reproduces no material previously published or written, nor material that has been accepted for the award of any other degree or diploma, except where due acknowledgement has been made in the text.

_____ (Signed)

Yong HU (Name of student)

Abstract

With unique amorphous structures, bulk metallic glasses exhibit a series of novel physical and chemical properties, and attract considerable research interest. Among the family of bulk metallic glasses, rare earth-transition metal (RE-TM) based bulk metallic glasses (BMGs) are known to exhibit large coercivity at room temperature, and the coercivity is very sensitive to the variation in microstructure. Although a considerable amount of research effort has been spent in studying their magnetic properties, the origin of their large coercivity, and the relationship between their microstructure and magnetic properties are still not fully understood.

In this project, the dependence of magnetic properties on the microstructures of Nd-based BMGs has been investigated. Different microstructures of the BMGs were realized by minor alloying, adjusting the cooling rate and varying the temperatures. It is found that the glass-forming ability of $(Nd_{60}Fe_{30}Al_{10})_{100-x}Ni_x$ alloys can be significantly enhanced with the addition of Ni. The content of the non-magnetic phases is increased by adding Ni, which strengthens the effect as a pinning center to the magnetic phase and increases the coercivity in the BMGs. The cooling rate induced evolution in microstructure, from amorphous to partial crystalline precipitation, was also observed in one as-cast $Nd_{60}Fe_{30}Al_{10}$ sample. A featureless amorphous phase was observed at the periphery, and a network-like structure, consisting of the Fe-rich, Nd-rich and amorphous regions, was formed in the center of the sample. As a consequence of different microstructures, two magnetic

structures were observed at the periphery and the center of the cross section, respectively.

At room temperature, the as-cast $Nd_{55}Fe_{28}Al_9Ni_8$ BMG, which consists of nanoclusters no larger than 5nm embedded in amorphous matrix, exhibits one magnetic phase behavior. However, the appearance of an apparent step in the hysteresis loops at low temperature implies the presence of at least two ferromagnetic phases in the alloy. Based on Monte Carlo simulation, the coercivity of the clusters of the BMG is found to be closely related to the change of temperature and the anisotropy of the clusters. By overlapping the hysteresis loops of the two cluster systems at different temperatures, a step is also observed in the hysteresis loop when the system is at low temperature. This result is consistent with the experimental findings.

The findings of the present investigation do not only result in a better understanding of the microstructure-magnetic properties of the BMG, but also lay down a good foundation for further improving their magnetic properties by tailoring their microstructures.

Publications Arising from the Research

[1] Y. Hu, L. Liu, K.C. Chan, Y.Z. Yang ,Effect of Ni addition on glass forming ability and thermal stability of Nd–Fe–Al–Ni bulk metallic glasses, *Journal of Alloys and Compounds* 419 (2006) 251–255

[2] Y. Hu, L.Liu, K.C. Chan, Y.Z. Yang, Cooling rate induced variation in microstructure and magnetic structure of $Nd_{60}Fe_{30}Al_{10}$ glass forming alloy, *Materials Letters*, 61(2007)3909-3912

[3] Y. Hu, K.C. Chan, L. Liu, Y.Z. Yang, Dual magnetic phases in Nd-based bulk metallic glass, *Materials Letters*, 62(2008) 4012-4014

[4] Y. Hu, K.C. Chan, L. Liu, Y.Z. Yang, Investigation of two magnetic phases in bulk metallic glass alloys by Monte Carlo simulation, in preparation

Acknowledgement

First and foremost, I would like to thank Prof. K. C. Chan, my chief supervisor, for his continuous support and encouragement during my study. I would also thank Prof. L. Liu, my co-supervisor, of the Huazhong University of Science and Technology, for his inspiration and suggestions.

I am also grateful to Mr. S.Y. Lau of Materials Engineering Laboratory, Mr. M. N. Yueng of Materials Research Center, Dr. K.H. Pang of Department of Applied Physics, Prof. Y. Z. Yang of Guangdong University of Technology, Dr. L. Xia of Shanghai University, Mr. X. G. Li and Dr. W. Y. Chueng of the Chinese University of Hong Kong, for their help and advice during my experiments.

Finally, I would like thank the staff and research students in the Department of Industrial and Systems Engineering for their support and help.

Table of Contents

List of Figures

List of Tables

Chapter 1 Introduction

1.1 Background

Rare-earth (RE) permanent magnets, as excellent magnetically hard materials, are ideally suited to generate magnetic fields due to their characteristics such as spontaneous polarization, large values of the coercivity, anisotropy fields and near-square hysteresis loops [1].Thus, permanent magnets have been applied in daily life in such areas as sensors, actuators, generators and so on. As one of the most popular permanent magnets, $Nd_2Fe_{14}B$, in 1995, only 10 years after discovery, its worldwide sales were close to 500 million US dollars [2].

However, up to the present, permanent magnet systems prepared by melt-spinning, depositing and mechanical milling, are usually in small size such as ribbons, films and powders [3]. To design a magnetic device of large size, a necessary process is to bind or sinter these ribbons, films and/or powders into bulk forms. The applications of these permanent magnets are undoubtedly limited due to their small dimensions and/or complicated manufacturing processes. Thus, it is very interesting and significant to develop magnetically hard materials in large size in a simple process.

Recently, the discovery of magnetically hard bulk metallic glasses has attracted increasing interest not only due to their scientific significance but also because of their potential applications. In addition to their good magnetic properties, their manufacturing cost can be cut down dramatically by one step, net shape casting.

Even though high coercivities ranging from 291 to 321kA/m were found in rare-earth based magnetically hard bulk metallic glasses at room temperature [4-6], many issues still remain to be resolved in these alloys [7-11]. One of the key issues is that their magnetic properties are still not comparable with those in $Nd_{14}Fe_7B$ permanent magnets, and they need to be further improved. Academically, the origin of hard magnetic properties in bulk metallic glasses is still not clear, although considerable effort has been spent on understanding their hard magnetic properties.

It is well known that magnetic properties are closely related to the microstructure of the materials, and different microstructures in bulk metallic glasses can be obtained by minor-alloying and controlling the process and working conditions. It is of great significance to understand the relationship between the microstructure and magnetic properties of RE-TM based BMGs so as to improve their magnetic properties by tailoring their microstructures.

1.2 Objectives

The present project aims to study and gain a better understanding of the dependence of magnetic properties on the microstructure of magnetic bulk metallic glasses. The specific objectives of the project are:

1. to synthesize magnetically hard bulk metallic glass with enhanced properties through minor-alloying;
2. to investigate the effect of minor alloying on microstructure, thermal, and magnetic properties of the as-cast bulk metallic glasses;
3. to investigate the effect of cooling rate on the microstructures and magnetic properties of the as-cast bulk metallic glasses;
4. to examine the magnetic behavior of the bulk metallic glasses at different temperatures;
5. to predict the magnetic behavior of bulk metallic glass by Monte Carlo simulation.

1.3 Organization of the thesis

This thesis consists of 10 chapters. Chapter 1 gives a brief introduction of the background of present studied bulk metallic glasses and the objectives of the thesis. The literature review on the development and characteristics such as glass forming ability, microstructure and magnetism of bulk metallic glasses are given in Chapter 2. The effects that may affect the microstructure and therefore the magnetic properties of bulk metallic glasses are reviewed. Besides, the simulation work on magnetic metallic glass and the Monte Carlo simulation technique are reviewed in this chapter. In Chapter 3, experimental procedures including sample preparation and characterization are described. From Chapters 4 to 7, the results of the investigations are analyzed and discussed. The effect of minor-alloying on glass forming ability and magnetic properties of bulk metallic glass alloys is presented in Chapter 4. The effect of cooling rate on the microstructure and magnetic structure of the bulk metallic glasses is investigated and described in Chapter 5. The effect of temperature on the microstructure and magnetic properties of Nd-based bulk metallic glasses is also experimentally investigated and the results are shown and discussed in Chapter 6. The results of Monte Carlo simulation on the dual magnetic phase related irregular hysteresis loop in the bulk metallic glasses at low temperature is demonstrated in Chapter 7. An overall conclusion to the study is given in Chapter 8. Some work, which is of significance and suggested to be carried out in the future, is given in

Chapter 9. In the last chapter, the originality of the present investigation and contribution to knowledge in the studied field are stated briefly.

Chapter 2 Literature Review

2.1 Bulk Metallic Glass

2.1.1 History of Bulk Metallic Glasses

Metallic glass was first successfully prepared from a molten alloy by Klement et al in 1960 when rapid quenching technology (RQT) was employed to cool the molten Au-Si alloy into an amorphous structure bypassing the occurrence of crystallization [12]. In their report, minute flakes, approximate 10 μm thick, were obtained by quenching a molten Au-Si alloy, containing 25 atomic % Si, from about 1,600K to room temperature. X-ray diffraction patterns showed the flakes to be in an amorphous state. Although the flakes were so unstable at room temperature that partial decomposition occurred, even at room temperature, within 24 hours, their success evoked a new explosive development in the metallurgy industry. Due to the absence of a periodic arrangement in the atoms, metallic glasses possessing unique characteristics have become a research subject of increasing interest, being motivated both from a basic as well as an applied point of view. By using rapid quenching technology, such as single-roll melt-spinning, a cooling rate at least 10^2K/s, and typically of the order of 10^6K/s, can be achieved. Due to the high cooling rate, the nucleation and the growth of crystalline phases are bypassed and the disordered structure in the liquid state is then frozen and kept in the solid state that

forms the metallic glass. The arrangement of atoms in metallic glasses does not form a periodic lattice as in crystalline materials, and no traditional symmetry is found in the structure of metallic glasses. Due to this unique disordered structure, metallic glasses exhibit various kinds of characteristics such as soft magnetic properties [13] and corrosion resistance [14]. Especially, the engineering application of soft magnetic materials replacing Silicon-Steel strips in transformers or other magnetic cores resulted in a revolution in the electric power industries. Although metallic glasses are of significant academic and practical value [15-19], samples prepared by rapid quenching are still in ribbon form, which will undoubtedly limit their applications. Thus, there have been many attempts to develop metallic glasses in large size over the past decades.

In 1969, Chen and Turnbull found that Pd-Au-Si alloys can be made up to 1mm thick by dropping the melting alloys onto a metal substrate [20]. This alloy should be the first piece of bulk metallic glass. A “bulk” metallic glass is always regarded as one which can be prepared with dimensions above the millimeter scale. A few years later, Pd-based bulk metallic glasses with diameters up to 3mm were produced by water quenching the molten alloy in a sealed quartz tube, as reported by Chen [21]. The cooling rate of water quenching was estimated to be less than 10^3K/s. In 1984, a fluxing treatment with molten B_2O_3, employed by Kui, Greer and Turnbull, significantly reduced the impurities in the Pd-Ni-P alloy. The maximum thickness of the bulk metallic glass with fluxing treatment was reported to be about 10mm and the cooling rate was estimated to be as low as 10K/s [19， 22, 23]. However, besides

the academic interest, no practical application was found in these Pd based bulk metallic glasses. One of the reasons might be that the noble metals such as Pd and Au are too expensive. In the late 1980s, a new explosive age for studying bulk metallic glasses was rapidly evoked by Inoue's group in Japan. A new series of metallic glass used common elements as the base, such as Nd-[5], Mg-[24], Ln-[25], Zr-[26], Fe-[27-29] and Co-[30], and with large glass forming ability were successfully synthesized. These new alloys, which always consist of more than three kinds of metallic elements, can be prepared from various technologies such as water quenching, copper mold casting and die casting. The cooling rate in these technologies are about several hundreds degrees Kelvin per second, which is much lower with respect to the cooling rate of melt spinning. More recently, some binary bulk metallic glasses consisting of only two elements, such as Zr/Cu or Ni/Nb, were developed at almost the same time by different research groups [31-34], which should trigger more research work in developing new bulk metallic glass systems.

Among various bulk metallic glass systems, rare earth based bulk metallic glasses have raised great interest due to their hard ferromagnetism at room temperature [5-6]. Differing from previous bulk metallic glasses systems exhibiting a wide supercooled liquid region before crystallization, it was also reported that glass transition and the supercooled liquid region were not observed during the thermal scanning, using a differential scanning calorimeter, even though a large size can be easily obtained in these bulk metallic glasses. For example, $Nd_{60}Fe_{30}Al_{10}$ bulk metallic glasses can be easily prepared in large size up to 12mm, and high

coercivities ranging from 291 to 321kA/m were measured at room temperature [35]. The research interest in RE-bulk metallic glasses has been focusing on their anomalous thermal behavior and hard ferromagnetism. Wei et al. have investigated the glass transition and crystallization behaviour of RE-based bulk metallic glasses by dynamic mechanical thermal analysis (DMTA) [36]. Although a large supercooled liquid region ranging from 80 to 130 K was observed in their investigation, Inoue has proposed that the apparent glass transition temperature may not be observed if the glass transition temperature is higher than the crystallization temperature. More recently, Xia et al. have reported that a distinguishable glass transition temperature was observed by a differential scanning calorimeter in Nd-based bulk metallic glass, with a modification in composition [37]. Much effort has also been made in studying the ferromagnetism of these BMGs. Different mechanisms have been proposed to describe their hard magnetic properties, and relevant details are discussed in Sections 2.2 and 2.3.

2.1.2 Glass Forming Ability

2.1.2.1 Origin of glass forming ability

Figure 2-1 illustrates the relationship between the enthalpy, the volume of liquid and the temperature of a material. It can be seen that there are two ways for a liquid to solidify [38]. If the cooling rate is high enough, the crystallization will be bypassed and the liquid state structure will be kept by freezing. With a narrow transition region, the volume or enthalpy of a non-equilibrium structure will decrease

rapidly with the decrease of the temperature. At the same time, if the system is cooled down slowly, the nucleation will occur in a time scale which is large enough and crystallization will occur. Usually, the glass forming ability of bulk metallic glass is superior to that of binary metallic glass. The origin of the high glass forming ability in bulk metallic glass can be understood from four aspects, i.e., structure, thermodynamics, kinetics and valence concentration.

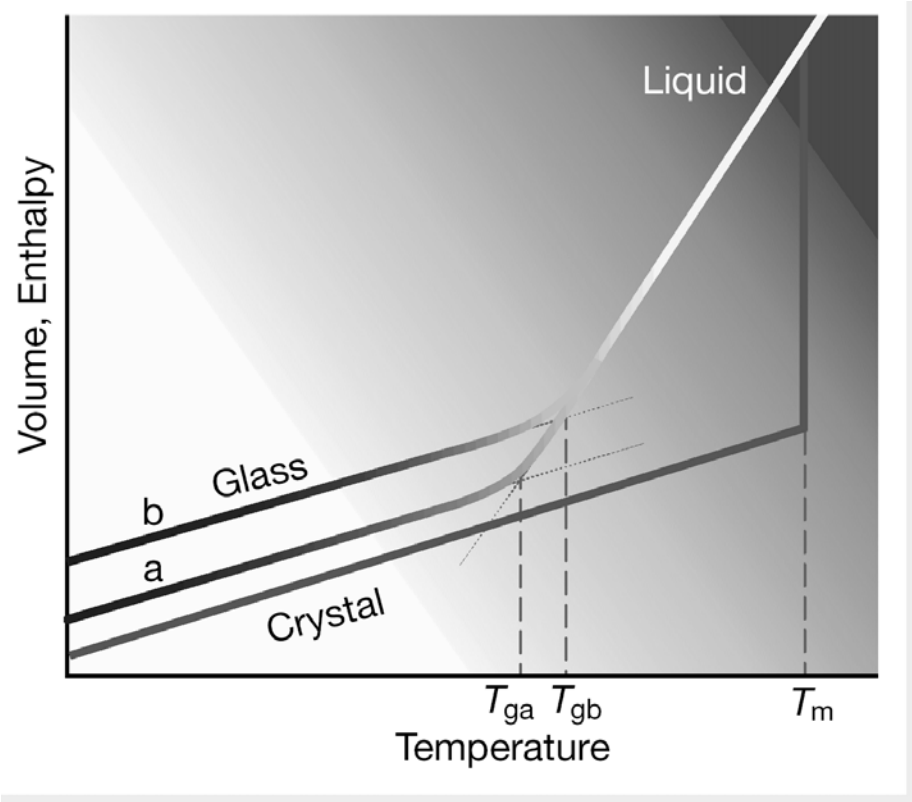

Figure 2-1 Dependence of a cooling liquid's volume (*V*) and enthalpy *(H)* on temperature at constant pressure. T_m is the melting temperature. A slow cooling rate produces a glass transition at T_{ga}; a faster cooling rate leads to a glass transition at T_{gb} [38].

Structurally, one of the most significant differences between bulk metallic glass and traditional metallic glass is that bulk metallic glass systems are always composed of more than three elements, with a great difference in the atomic size.

Table 2-1 shows a comparison in density of bulk metallic glasses in an as-cast state and those with full crystallization [39]. It is found that there is a difference of about 0.3~0.54% in the value of density between the as-cast and full crystallized bulk metallic glasses, which is much less than the density difference of about 2% for binary metallic glasses made by the traditional ultra-high rapid cooling technology. The small difference in the density of as-cast and full-crystallized bulk metallic glasses implies that bulk metallic glasses have a random highly packed structure. This structure has a higher solid-liquid interface energy which will depress nucleation of the crystalline phase. At the same time, it will increase the viscosity when the temperature decreases and the long term diffusion of atoms in the system will also become difficult to achieve. As a result, the growth of crystalline phases will be frustrated. Peker et al. has investigated the effect of the addition of Be on the glass forming ability of a Zr-based bulk metallic glass [40]. The atom radius of Be is known to be much smaller than that of Zr and Ti atoms (the difference in atomic radius being larger than 20%) [40]. Small atoms like Be added into the system will fill the space, leading to a decrease in the free volume of the metallic glass, and an increase in the coefficient of viscosity in the supercooled state. It will increase the solid-liquid interface energy and depress the long distance diffusion in the BMG.

Table 2-1Difference between the density of as cast and fully crystallized Zr- and Pd- based bulk metallic glasses [39]

Alloy (state)	ρ_{cast}(Mg/m^3) (Amorphous)	$\rho_{relaxed}$(Mg/m^3) (Amorphous)	ρ_{crysta}(Mg/m^3) (Crystal)	$\Delta\rho_{relaxed}$(%) [a]	$\Delta\rho_{crysta}$(%) [b]
$Zr_{60}Al_{10}Cu_{30}$	6.72	-	6.74	-	0.30
$Zr_{55}Al_{15}Ni_{25}$	6.36	-	6.38	-	0.31
$Zr_{55}Cu_{30}Al_{10}Ni_5$	6.82	6.83	6.85	0.15	0.44
$Pd_{40}Cu_{30}Ni_{10}P_{20}$	9.27	9.28	9.31	0.11	0.54
$Zr_{55}Ti_5Ni_{10}Cu_{20}Ni_{10}$	6.62	-	6.62	-	0.30
$Zr_{52.5}Ti_5Al1_{2.5}Cu_{20}Ni_{10}$	6.52	-	6.65	-	0.45

[a] $\Delta\rho_{relaxed}=(\rho_{relaxed}-\rho_{cast})/\rho_{cast}$

[b] $\Delta\rho_{crysta}=(\rho_{crystal}-\rho_{cast})/\rho_{cast}$

From the thermodynamics perspective, the formation of a glass structure in an alloy implies that the driving force for crystallization in the supercooled region of the alloy is low, and the crystallization is depressed during the cooling process. The thermodynamic driving force of the crystallization is given by the difference in Gibbs free energy between the supercooled liquid and the corresponding crystalline phase. The Gibbs free energy difference is calculated by integrating the measured specific heat capacity difference between the supercooled liquid and the crystal, taking the enthalpy and entropy of fusion into account, which can be expressed by the following the equation[41]:

$$\Delta G_{l-x} = \Delta H_f - T\Delta S_f - \int_T^{T_f} \Delta c_p{}^{l-x}(T)dT + T\int_T^{T_f} \Delta c_p{}^{l-x}(T)d\ln T \qquad (2\text{-}1)$$

where ΔH_f and ΔS_f are the enthalpy and entropy of fusion, respectively, at a

temperature T_f. T_f is the temperature where the Gibbs free energy of the crystal and the liquid are equal. Δc_p is the difference in specific heat capacities between the liquid and crystal. .

From this equation, it is found that a low free energy ΔG_{l-x} can be obtained by a large ΔS_f and a small ΔH_f. A multi-component system is expected to have larger solid/liquid interfacial energy which favors a large ΔS_f and a small ΔH_f.

Besides the thermodynamic considerations, the glass forming ability can also be understood from the kinetic view of nucleation and growth of crystals. According to the classic homogeneous nucleation theory, there is a critical nucleation energy ΔG^* which will determine the probability of nuclei formation P [42]:

$$\Delta G^* = -\frac{16\pi\sigma^3}{3\Delta G_{l-x}{}^2} \tag{2-2}$$

$$P \propto \exp[-\frac{16\pi\sigma^3}{3\Delta G_{l-x}{}^2 k_B T}] \tag{2-3}$$

where, σ is the interfacial energy between the solid and liquid phases, $16\pi/3$ is the shape factor of a spherical nucleus and k_B is the Boltzmann constant. From Equation (2-3), it is clear that a small thermodynamic driving force contributes directly to a low probability of nucleation and therefore results in excellent thermal stability against crystallization.

However, the probability of nucleation is always high in real situations due to the presence of impurities and other factors. In order to evaluate the glass forming ability, both the rates of nucleation and growth should be considered. If steady-state nucleation is assumed, the crystallization is determined by the product of the

nucleation contribution and the crystalline growth contribution according to the nucleation rate (*I*) and the crystal growth rate (*U*) [43]:

$$I = \frac{10^{30}}{\eta}\exp[-b\alpha^3\beta/(T_r(1-T_r)^2] \qquad [\mathrm{cm^{-3}s^{-1}}] \tag{2-4}$$

$$U = \frac{10^2 f}{\eta}[1-\exp(-\beta\Delta T_r/T_r(T/T_m))] \qquad [\mathrm{cm^{-1}s^{-1}}] \tag{2-5}$$

where, T_r is the reduced temperature (T/T_m), ΔT_r is the difference in temperature from T_m, b is a shape factor, being $16\pi/3$ for a spherical nucleus, η is viscosity, and f is the fraction of nucleus sites at the growth interface, α and β are dimensionless parameters related to the liquid /solid interfacial energy (σ), while ΔH_f and ΔS_f can be expressed as $\alpha = (N_0V)^{1/3}\sigma/\Delta H_f$ and $\beta = \Delta S_f/R$ respectively. N_0, V and R are the Avogadro number, the atomic volume, and the gas constant, respectively. In these relationships, η, α and β are three important parameters. Their increase will decrease the value of *I* and *U*, i.e., depress the nucleation and growth rate, leading to an increase of GFA. The increase of α and β also implies an increase in σ and ΔS_f and a decrease in ΔH_f, which is consistent with the interpretation of achieving a high GFA, from the thermodynamic point of view.

Electronically, in order to obtain a low energy state in a system, the total kinetic energy of the valence electrons should also be reduced. Nagel and Tauc [44] treated metallic glass as a nearly free electron metal and the influence of valence electrons on the structure factors has been used to understand the stability of a metallic glass against crystallization. They proposed that a metallic glass will be stabilized when the

Fermi level (E_F) is located at a minimum in the density-of-state curve. This will occur when the Fermi surface and the diffused pseudo-Brillouin zone boundary of the glassy phase coincide, which is similar to that in the Hume-Rothery intermediate phases. The Hume–Rothery phase is electronically stabilized when a pseudogap is formed across the E_F. The Fermi surface–Brillouin zone (FS–BZ) interaction, denoted as $2k\mathrm{f} \approx k\mathrm{p}$, where kf is the momentum of electrons at the Fermi level and kp is the width of the Brillouin zone, is believed to be a mechanism directly related to the formation of the pseudogap at E_F [45-47].

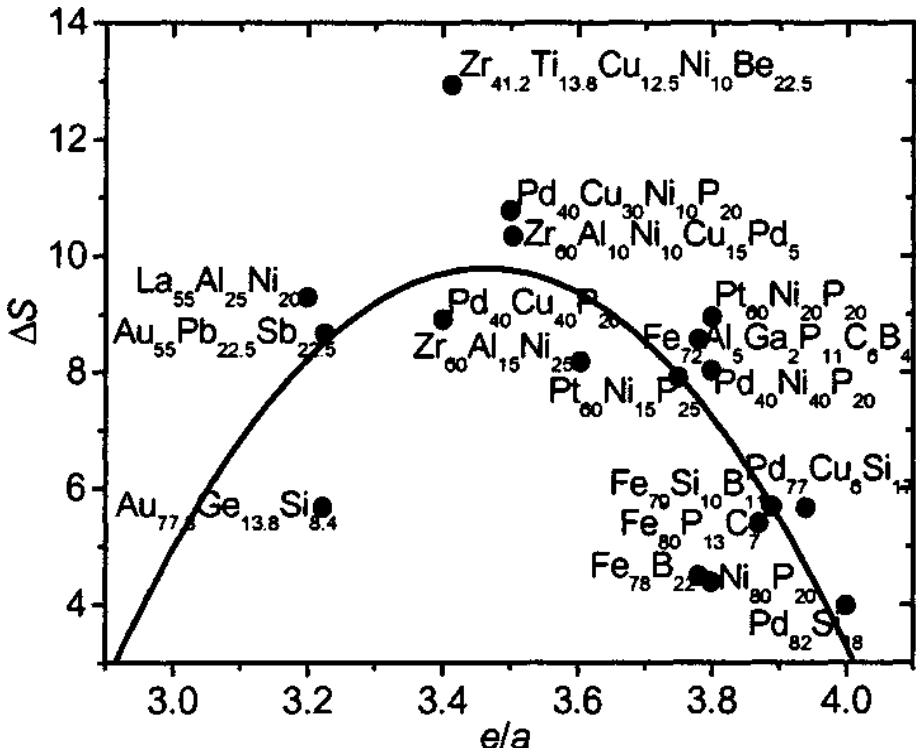

Figure 2-2 Functional dependence of ΔS on e/a [48]

Regarding the stabilization of metallic glasses, Jiang et al suggested that when the liquid and the corresponding crystal have a similar structure even though the crystal may usually be in a metastable state, the enthalpy difference may be very small if the

liquid has a special *e*/*a* value (*e* and *a* denote valence and atom number in a unit cell, respectively) with the most negative ΔH. According to their suggestion, a relation between entropy and valence concentration in many bulk metallic glasses can be plotted. Those alloys with a value of 3.5 in *e/a* are believed to have large tendency to form bulk metallic glasses (See Figure 2-2). According to the theory of valence concentration, Wang et al successfully developed a series of Zr-based bulk metallic glasses [49-52].

2.1.2.2 Criteria of glass forming ability

The critical cooling rate (R_c) and the maximum sample thickness (Z_{max}) are two simple indicators of GFA. Although they are fundamental parameters, they are difficult to measure precisely and do not tell much about the potential of an alloy system to form an amorphous structure. A more reliable and measurable gauge of GFA has to be developed for bulk metallic glasses. Turnbull and his coworkers have observed that glass transition occurs at a rather well-defined critical temperature, which varies only slightly as the heating rate is changed [53]. They have proposed the reduced glass transition temperature:

$$T_{rg} = T_g / T_m$$

where, T_g is the glass transition temperature, T_m is the melting temperature or liquidus temperature T_l. This equation can be used as a criterion for determining the GFA of alloys [53]. When the interval between T_g and T_m decreases, the value of T_{rg}

increases, so that the probability of being able to cool through the interval between T_m and T_g without crystallization is enhanced, leading to an increase in GFA. According to the Turnbull's criterion, a liquid with $T_g/T_m = 2/3$ becomes very inactive in crystallization within the laboratory-time scale and can only crystallize within a very narrow temperature range. Such a molten alloy can then be easily undercooled at a low cooling rate into a glassy state. Up to now, Turnbull's criterion for the suppression of crystallization in undercooled melts remains one of the best "rules of thumb" for predicting the GFA of any alloy. It has played a key role in the development of various metallic glasses.

However, in some RE-TM (rare earth-transition metal) based bulk metallic glasses, such as $Nd_{60}Fe_{30}Al_{10}$ and $Nd_{70}Co_{20}Al_{10}$ alloys, cylinders of 12mm diameter have been prepared [4, 35]. Differing from other bulk metallic glasses, no glass transition temperature before the crystallization temperature was observed in these bulk metallic glasses. Inoue attributed the high GFA of these alloys to the large reduced crystallization temperature defined as [4]:

$$T_{rx}=T_x/T_m$$

where, T_x is crystallization temperature, T_m is the melting temperature or liquidus temperature T_l [4]). More recently, Lu and Liu have also introduced a new parameter, defined as $T_x/(T_g+T_l)$ to evaluate the GFA of an alloy[54].

Besides, the valence concentration criterion on glass forming ability, originating from the stability of the electronic structure in the alloy, is also considered [48, 49]. Deduced from the Hume-Rothery rule [55], this criterion proposes that a suitable

value of electron concentration *e/a*, should be selected to lower the system energy during the designing of new bulk metallic glasses.

However, the criteria mentioned above for the evaluation of GFA are not always effective while applied to the determination of the GFA of different kinds of bulk metallic glasses. Some empirical rules have been derived to achieve a GFA based on the accumulated experimental results on the formation of bulk metallic glasses, i.e.,

(1) multicomponent alloy systems consisting of more than three elements,

(2) significantly different size ratios of about 12% among the three main constituent elements, and

(3) negative heats of mixing among the three main constituent elements [56].

However, searching for a simple and reliable gauge to quantify GFA for metallic glasses is still one of the hottest topics in this field.

2.1.3 Microstructure

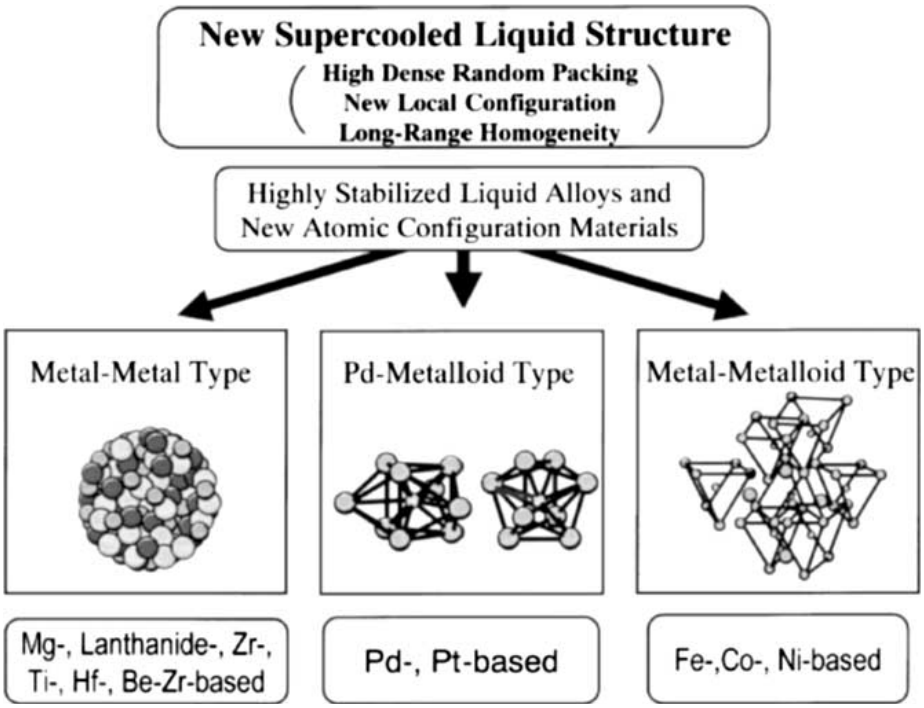

Figure 2-3 Different atomic configurations of three types of BMGs [57].

It is known that in order to achieve a large glass forming ability in forming bulk metallic glasses, alloys are expected to be composed of more than three elements, with large differences in size. Due to this mutli-component system, a new supercooled liquid structure, characterized by a high degree of dense randomly packing, with a new local configuration as well as long range homogeneity, is formed in bulk metallic glass forming systems [57]. The structure features provide a reasonable explanation for the excellent GFA of BMG forming alloys. The conventional metallic glasses with poor GFA have their corresponding crystalline compounds similar to the amorphous alloys in their local structures and

compositions [58]. For these alloys, the cooling rates are the most important factors to inhibit the nucleation and growth of the competing crystalline phases. For the BMG formers, however, the critical cooling rates are much lower, and their local microstructural characterization therefore becomes a decisive factor for its glass-forming ability. The configurations are different among the three types of BMGs as shown in Figure 2-3 [57]. According to the alloy components, Inoue has classified the structures of bulk metallic glasses into three types, metal-metal type alloys, metal-metalloid-type alloys and Pd-metalloid alloys [59].

In the metal–metal alloy, high-resolution TEM, XRD, and neutron diffraction studies reveal that this kind of bulk metallic glass consists of icosahedral clusters [60-62]. The critical size for a transition from an icosahedral cluster to an icosahedral phase is around 8 nm [59]. When the BMG is annealed in the supercooled liquid region, the icosahedral quasicrystalline phase (I-phase) precipitates in the primary crystallization step, and the I-phase transforms to a stable crystalline phase at higher temperatures [60-63]. The precipitation of the I-phase is due to the structural heredity of the local structure of the BMG. The existence of icosahedral clusters provides seeds for the precipitation of the I-phase and indicates the importance of the icosahedral cluster as the fundamental structural unit. Analysis based on nucleation theory has revealed that the activation energy for the nucleation of the I-phase is smaller than that for nucleation of crystals in the undercooled alloy [64].

The icosahedral clusters (or icosahedral short-range order) in the amorphous state will provide an additional barrier for the nucleation of the crystalline phases. Since the I-phase with a five-fold rotational symmetry will be incompatible with the translational symmetry of the normal crystalline phases, therefore it has to be dissociated before the formation of the crystalline phases can occur. From a kinetics point of view, the crystallization of BMG requires a substantial redistribution of the component elements across the icosahedral liquid. The highly dense, randomly packed structure of the BMG in its supercooled state results in extremely slow atomic mobility [65], thus making a large scale redistribution of atoms very difficult. This fundamental structural discontinuity between the crystalline and the amorphous state suppresses the nucleation and the growth of the crystalline phase from the supercooled liquid, resulting in an excellent GFA.

For the metal–metalloid-type glassy alloys, for instance Fe(Co)–Nb–B, a network atomic configurations consisting of trigonal prisms which are connected with each other through glue atoms comprising Zr, Nb, Ta or lanthanide metal, are commonly found. Fe-based BMGs form primary crystals of the complex f.c.c.-$Fe_{23}B_6$ phase with a large lattice parameter of 1.1 nm and a unit volume consisting of 96 atoms [57].

Pd-based BMGs do not satisfy the three empirical rules proposed by Inoue, and the structural investigation shows that Pd–Cu–Ni–P BMGs consist of two large clustered units of a trigonal prism caped with three half-octahedra for the Pd–Ni–P

and a tetragonal dodecahedron for the Pd–Cu–P region, as shown in Figure 2-3. Based on the phenomenon of the distinctly different GFA between Pd-Ni-Cu-P and Pd–Ni–P, the coexistence of the two large differing clustered units seems to play an important role in the stabilization of the supercooled liquid for the Pd-based alloy. This is in turn is attributed to the strong bonding nature of the metal–metalloid atomic pairs in the clustered units and the difficulty of rearrangement among the two kinds of clustered units.

Strictly speaking, as a special bulk metallic system, the structure of RE-TM bulk metallic glasses may not be fully amorphous. In the study of $Pr_{60}Fe_{30}Al_{10}$ and $Nd_{70}Fe_{20}Al_{10}$ bulk metallic glasses, although the X-ray diffraction results do not show any crystalline precipitates, a high density of short-range ordered cluster regions is observed in the alloy, by HRTEM. In order to clarify the kind of atomic pairs in the observed short-range clusters, the radial distribution functions (RDF) of $Nd_{70}Fe_{20}Al_{10}$ show that the atomic pairs in the clusters are Nd-Fe and Nd-Nd. The clustered amorphous structure containing Nd-Fe and Nd-Nd atomic pairs is believed to contribute to the hard magnetic properties in these rare earth based bulk metallic glasses. Nd-based bulk metallic glasses are considered to contain a relaxed amorphous structure, which may result in the hard magnetic properties [65]. With the help of TEM and small angle neutron scattering, the structure observed by Schneider is shown to be finely dispersed nanocrystalline Nd-rich phase embedded in a Fe-rich glassy matrix in the as-cast $Nd_{60}Fe_{30}Al_{10}$ bulk metallic glass [66]. However, in the investigation of the abnormal glass forming ability in $Nd_{60}Fe_{30}Al_{10}$ bulk metallic

glass, Sun et al. have reported that the metastable A1 phase is formed in the alloy due to the positive heat of mixing between Nd and Fe [67]. The A1 phase has also been reported by other researchers to be amorphous or nanocrystalline and to exhibit hard magnetic behavior [68]. In order to fully understand the microstructure of RE-TM bulk metallic glasses, more in-depth work still needs to be carried out.

2.1.4 Properties and Applications

In the early development stage of metallic glasses, only ribbons or wire could be synthesized by rapid melt-spinning due to the limitations in cooling rate and equipment, and the limited composition systems,. The applications of these metallic glasses are mostly in the magnetically soft fields. The typical metallic glasses are $Fe_{40}Ni_{40}P_{14}B_6$, $Fe_{32}Ni_{36}Cr_{14}P_{12}B_6$ and $Fe_{29}Ni_{49}P_{14}B_6Si_2$ for applications in recording heads or transformer cores with the trade mark “Metglas” [69-71].

Since the discovery of bulk metallic glasses which can be formed into complicated shapes by die casting, a number of applications have been explored. The first application of BMG is for golf club heads. A BMG head has been found to be twice as hard and four times as elastic as a Ti driver. About 99% of the impact energy from a BMG head can be transferred to the ball (compared to 70% for Ti). Moreover, BMG heads have higher strength-to-weight ratio which allows the mass to be distributed differently, enabling various shapes and sizes of the head. By utilizing the efficient energy transfer characteristics, BMGs are also applied in other high-end

sporting goods such as tennis rackets, and the applications for baseball bats, bicycle frames, hunting bows, and even edged tools such as axes are being explored [72].

The advantages of producing thin complex plates in net-shape from bulk metallic glasses enable the alloy to be produced for consumer electronics cases. With the trend of miniaturization of personal electronic devices, such as MP3 players and personal digital assistants (PDA), there is a pressing need to make the casing thinner while retaining sufficient mechanical strength. BMGs exhibit obvious advantages over polymeric materials and conventional light alloys. Mobile phones and digital still cameras with BMG casing are already being developed [73].

Besides the applications in daily life, the applications of bulk metallic glasses are also extended into the military regime, such as antitank penetrators. Unlike crystalline materials which flatten into mushroom shapes after impact, the sides of W-reinforced metallic glass composites head will shear away and sharpen. Apart from the self-sharpening behavior, it is more environmentally safe to use metallic glass for replacing the depleted-uranium antitank penetrators which are radiation hazards [73].

Another interesting application of BMGs is in the biomedical field. The unique properties of BMGs for orthopedic applications include: (1) biocompatibility (2) excellent wear resistance; (3) high strength-to-weight ratio compared to titanium and/or stainless steel; (4) more than twice the strength of titanium or stainless steel; (5) possibility of precision net-shape casting with desirable surface texture which results in significant reduction in post-processing. Some of the products taking advantage of these improvements include reconstructive devices, fractured fixations, spinal

implants and instrumentation [73]. One of the latest industries attracted by the BMG is the fine jewelry industry. The BMGs can achieve a stunning surface finish which is catching the attention of high-end jewelry makers worldwide [73].

In the near future, BMGs materials will become more and more significant for basic research and applications, with the further developments in this field [73]. In summary, Table 2-2 gives some possible application fields for BMGs.

Table 2-2 Possible application fields for BMGs [72- 75]

Properties	Application field
High strength	Machinery structural materials
High hardness	Cutting materials
High fracture toughness	Die materials
High impact fracture energy	Tool materials
High elastic energy	Sporting goods materials
High corrosion resistance	Corrosion resistance materials
High reflection ratio	Optical precision materials
High hydrogen storage	Hydrogen storage materials
Good soft magnetism	Soft magnetic materials
High Hard magnetism	Hard magnetic materials
Efficient electrode	Electrode materials
High viscous flowability	Writing appliance materials

High acoustic attenuation	Acoustic absorption materials
Self-sharping property	Penetrator
High wear resistance and biocompatiable	Medical devices materials

2.2 Magnetism of Bulk Metallic Glasses

2.2.1 Basic Magnetic Theory

2.2.1.1 M-H hysteresis loop

The fundamental magnetic properties of a material are generally characterized according to its response, which is usually the magnetization *M*, to an applied magnetic field *H*. Figure 2-4 shows a schematic *M*-*H* hysteresis loop, where the intrinsic coercivity H_c is defined as the reversed field which reduces the magnetization to zero. M_s is the saturated magnetization in the applied field and M_r is the residual magnetization while the applied field is decreased to zero. A material is regarded as magnetically soft if a small applied field will result in magnetization saturation, however, a large applied field should be employed to saturate the magnetization of a hard magnetic material. There is no strict criterion to distinguish soft materials from hard materials. Broadly, hard magnetic materials are those with intrinsic coecivities H_c above 10kA/m while soft magnetic materials are those with coercivities below 1kA/m [76].

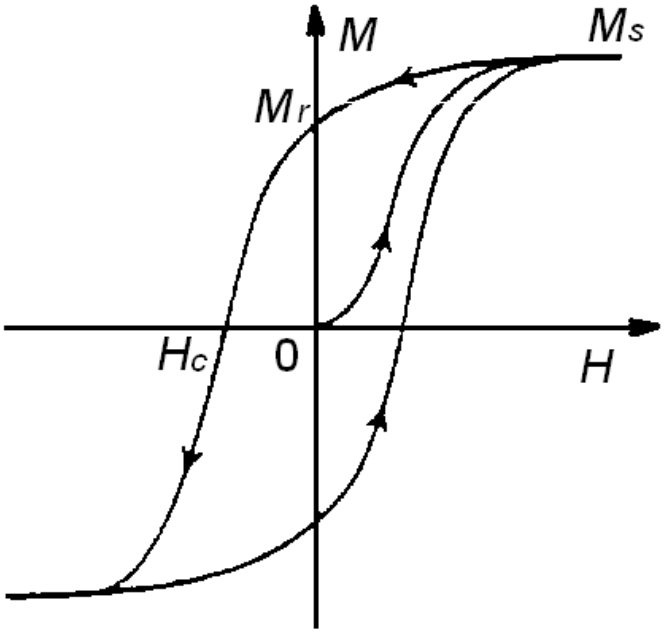

Figure 2-4 Schematic M-H hysteresis loop

2.2.1.2 Magnetic Domain

Weiss first introduced magnetic domains to explain ferromagnetism [77]. According to the assumption of Weiss, there is an internal magnetic field in ferromagnetic substances, which is also known as the Weiss molecular field. This field is formed by the neighboring molecules, and acts in conjunction with the external field and can produce many visible ferromagnetic phenomena. Even in the absence of an external field, the atomic magnetic moments will be aligned parallel so that the magnetization with the domains is almost saturated. However, the direction of alignment varies from one domain to another which will reduce the energy

generated by the molecular field. The boundary between two adjacent magnetic domains is called a domain wall.

2.2.1.3 Magnetic exchange interaction and random magnetic anisotropy

While discussing the magnetic ordering in ferromagnetic materials, two factors determining the magnetism should be considered: the exchange interaction and the magnetic anisotropy. On the one hand, the ferromagnetic exchange contributes to the parallel orientation of neighboring magnetic moments; on the other hand, the anisotropy aligns the magnetization along some preferred directions [78, 79].

The exchange interaction is described by the Heisenberg Hamiltonian function,

$$H_{ex} = -\sum_{\alpha\beta} J_{\alpha\beta}\, \hat{J}_{\alpha} \cdot \hat{J}_{\beta}\,, \tag{2-6}$$

where $\hat{J}_{\alpha}$ is the operator of the angular momentum of the α-th magnetic ion, and the coefficients $J_{\alpha\beta}$ rapidly go to zero as the distance between α-th and β-th ion increases. Eq.(2-6) can also be expressed mathematically as,

$$H_{ex} = -\frac{1}{(g\mu B)^2}\int d^3r \int d^3r'\, J(r-r')\, \hat{M}(r) \cdot \hat{M}(r')\,, \tag{2-7}$$

where $\hat{M}(r)$ is the operator of the magnetization, for the case of the coherent behavior of a large number of elementary magnetic moments. $\hat{M}(r)$ can be treated as a classical vector,

$$M(r) = \frac{1}{v} < \int_{v} d^3r'\, \hat{M}(r') >\,, \tag{2-8}$$

where v is a microscopic volume centered at r. The size of v is defined by the range of the ferromagnetic exchange, r_{ex}. The value of r_{ex} depends on the nature

of the exchange interaction and is typically smaller than the correlation length of the amorphous alloy r_0.

The rotation of $M(r)$ in an amorphous ferromagnet typically occurs on the scale $R_f >> r_{ex}$. Similarly to that mentioned above, as the distance between α-th and β-th increases, the coefficients $J_{\alpha\beta}$ will rapidly go to zero. According to a given static $M(r)$-configuration, the exchange interaction energy of the ferromagnet is given by:

$$E_{ex} = \frac{A}{M_0^{\,2}} \int d^3 r \frac{\partial M}{\partial r_i} \cdot \frac{\partial M}{\partial r_i}, \tag{2-9}$$

where A is the exchange constant,

$$A = \frac{2\pi M_0^{\,2}}{3(g\mu B)^2} \int_0^\infty dr r^4 J(r). \tag{2-10}$$

In rare-earth (RE) – transition-metal (TM) alloys, the Heisenberg Hamiltonian exchange interaction $H_{ex} = -\sum_{\alpha\beta} J_{\alpha\beta} \hat{J}_\alpha \cdot \hat{J}_\beta$ describes exchange interactions between TM–TM, RE–TM and RE–RE. It was found that the exchange constant between RE and TM atoms (A_{RT}) systematically decreases with increasing T-concentration [80, 81]. This variation of A_{RT} has been discussed in terms of the hybridization between the 3d (TM) and 5d (RE) states. This behavior was observed for the amorphous $Gd_{1-x}Co_x$ system [82].

On the other hand, the magnetic anisotropy arising from long-range crystallinity has been investigated extensively. However, the basis for developing the theory disappears due to the absence of a long-range ordered atom configuration in amorphous materials. In fact, in amorphous materials, the electrostatic field

contributing to magnetic anisotropy still forms because of the existence of charges of neighboring atoms or ions, as well as conduction electrons. The 3d electrons in TM ions with non-zero orbital angular momentum are known to interact strongly with the electrostatic field, exceeding the interaction resulting from exchange and spin-orbit coupling. The latter interactions are believed to restrict the ionic moment to certain preferred directions called easy axes, which are determined by the local electrostatic field gradients, and is the origin of magnetic anisotropy. For the case of RE metals of 4f electrons, the spin-orbit interaction dominates over the electrostatic field interaction and originates the magnetic anisotropy. According to the assumption of Harris et al, randomness of the anisotropy field is the most important characteristic of the amorphous state, that results from the topological disorder of a random close-packing structure in amorphous alloys. Based on this assumption, Harris, Plischke and Zuckermann proposed a model for random magnetic anisotropy [83], and the electrostatic field interaction is represented as Hamiltonian,

$$H = -\sum_i D_i (\hat{n}_i \cdot \hat{S}_i)^2 \tag{2-12}$$

where D_i is an anisotropy parameter and $\hat{n}_i$ is a unit vector randomly chosen for each site which gives the local easy axes. $\hat{S}_i$ is the total spin of the ion at each site.

Considering the exchange interaction, together with random magnetic anisotropy, the Hamiltonian function is written as,

$$H_{ex} = -\sum_{\alpha\beta} J_\alpha \hat{J}_{\alpha\beta} \cdot J_\beta - \sum_i D_i (\hat{n}_i \cdot \hat{S}_i)^2, \tag{2-13}$$

where the effect of external field is not calculated.

2.2.2 Magnetism in Hard Magnetic Bulk Metallic Glasses

The origin of hard magnetic properties in bulk metallic glasses has attracted great interest due to their potential applications, as well as the significance in fundamental research. It is known that extreme magnetic softness is usually associated with the disorder and homogeneity of the amorphous state, which lacks structural inhomogeneities, such as grain boundaries and other defects, that may block the domain wall motion during the magnetization process. In the 1990s, high performance Fe–Nd–B-based permanent magnets have been intensively studied. The discovery of improved coercivity of the magnetic BMGs by small additions of Al has brought much research attention to Nd-Fe-Al alloy systems [5, 84].

In original work in 1996, Inoue ascribed the high coercivity to the relaxed amorphous structure consisting of clusters, and the homogeneous dispersion of Ln-Fe and Ln-Fe-Al clusters with large random magnetic anisotropy that will result in the high coercivity in Ln-rich bulk metallic glasses [35, 65]. Since then, there have been great efforts to study the origin of high coercivity, but more work has yet to be done to fully understand the phenomenon. Among the explanations for high coercivity, the magnetic-exchange coupling interaction among magnetically ordered Fe-rich clusters with large random magnetic anisotropy, has been suggested by several authors [66, 85-87] as a possible explanation of the hard properties of bulk

Nd–Fe–Al samples. Schneider et al. have reported the existence of a Nd-rich nanocrystalline phase embedded in a Fe-rich glassy matrix of a bulk sample and assumed that such a system will exhibit hard magnetic properties if the length scale of the aggregate is similar to the magnetic correlation length [66]. Ding attributed the high coercivity to the large magnetic anisotropy which is probably produced by Nd atoms [85].

According to the random anisotropy model [88], amorphous materials with local large random magnetic anisotropy may exhibit high coercivity if the anisotropic magnetic entity (i.e. the magnetic cluster) has a size comparable with the exchange-coupling correlation length. In these conditions, the magnetic vector is strongly constrained by the orientation of the local anisotropy. In other words, hard magnetic properties are expected if the cluster size matches the single domain size. On the contrary, if the cluster size is much smaller than the exchange length, its magnetic anisotropy is averaged over various directions and the coercivity becomes weak.

Besides, to explain the large temperature-dependence of coercivity, which is usually related to a thermally activated magnetization process, the pinning of the domain walls has also been considered as the origin of the magnetic hardness of this alloy system [89-91]. The high coercivity in the bulk materials could arise mainly from impediments to the domain wall motion caused by magnetic inhomogeneities, such as non-magnetic precipitates, structural defects, cavities or any region with magnetic properties different from the matrix [92]. Particularly in $Nd_{60}(Fe,Co)_{30}Al_{10}$ bulk metallic glass, the coercive mechanism is supposed to be related to the

precipitation of Nd and $Nd(Fe,Al)_2$ in the nanocrystalline state. Being paramagnetic at room temperature, these particles, with an estimated diameter of 10 nm, may act as pinning centres for the domain walls of the ferromagnetic amorphous matrix. In this case, the coercive field is the critical field required to release the wall from the pin. This hypothesis is supported by the thermomagnetic behaviour of the samples which exhibit two Curie temperatures (i.e. two ferromagnetic- to-paramagnetic transitions), one above room temperature and another in the low temperature range, at about 50–60 K[89]. This behaviour evidences a phase separation in the nominally amorphous Nd–Fe–Al or (Nd, Y)–Fe–Al samples. According to these authors, the amorphous or nanocrystalline low-Tc phase, may strongly impede the domain wall motion if its size is comparable with the domain wall width of the amorphous ferromagnetic matrix.

Among the compositions suitable to be amorphised with ferromagnetic properties at room temperature, $Nd_{70}Fe_{20}Al_{10}$ has been studied extensively in view of its favourable combination of good GFA and good hard magnetic properties. The origin of the coercivity for this alloy has been ascribed to the pinning of the domain wall due to the precipitates in the metallic matrix. In fact, the XRD and DSC results show that all samples contain a significant amount of amorphous fractions, but crystallisation of Nd cannot be completely avoided even by rapid solidification. Since crystalline Nd is paramagnetic, the ferromagnetic behaviour of the samples is related to the presence of the amorphous phase [93].

The influence of thermal treatments on the hysteresis behaviour of $Nd_{70}Fe_{20}Al_{10}$ bulk metallic glasses has been also studied. As an example, the room-temperature

hysteresis loops of a master alloy and an as-cast sample subject to annealing at 350 °C have been reported. Both samples are ferromagnetic and exhibit hard magnetic properties in the as-prepared conditions [94]. The coercive field values turn out to be quite different: higher values of H_c are observed in the master alloy, while a lower value has been measured in the conical as-cast sample. Fully crystallized samples exhibit the typical magnetization behaviour of paramagnets. The magnetically hard behavior arises mainly from impediments to the domain wall motion caused by non-magnetic precipitates in the nanocrystalline state, embedded in the ferromagnetic amorphous matrix, acting as pinning centers. A reduction of H_c resulting from the thermal treatments is observed in both samples, especially in the master alloy. Conversely, an increase of magnetisation is observed with increase of the annealing temperature. This effect can be related to variations in composition of the residual amorphous matrix induced by the thermal treatments, resulting from the segregation of Nd atoms in nanocrystalline forms. The coercive field reduction can be ascribed to an increase of the size of Nd precipitates which are segregated from the matrix during the alloy solidification and are responsible for the pinning mechanism of the domain walls.

The optimal dimension for a non-magnetic precipitate to give rise to the maximum hardening effect has to be of the order of the domain wall width [89]. A further increase beyond this optimal size will cause a decrease in the pinning effect. With these findings, the annealing treatment is expected to induce a growth of the pre-existing Nd nanocrystals and a reduction of their effectiveness as pinning centres,

their size already being above the optimal one.

Up to now, the magnetism of hard magnetic bulk metallic glasses is still not very clear and further investigation needs to be done in this field.

2.2.3 Effects of Minor-alloying, Cooling Rate and Temperature on Microstructure and Magnetic Properties in Bulk Metallic Glass Forming Alloys

2.2.3.1 Introduction

It is well known that the formation of the microstructure in BMGs can be affected by a number of factors, namely the composition (including impurities) [72, 95-97], the cooling rate [98], and many other process conditions, such as pressure and radiation [99, 100]. Especially, since the microstructure and properties of hard magnetic bulk metallic glasses are closely related to the chemical composition and cooling rate, these effects will be reviewed separately in this chapter. Besides, the magnetic properties are strongly dependent on the temperature. The temperature dependent magnetic behavior of bulk metallic glasses will also be reviewed.

2.2.3.2 Minor-alloying

Minor addition or minor-alloying techniques have been widely used in metallurgical industries to modify the microstructure of materials. For example, the minor addition of rare earth materials has been widely used as a good scavenging flux in the steel melting and casting processes, because the reactions between rare earth elements and harmful impurities are thermodynamically favored, compared to those between impurities and Fe. A small amount of rare earth materials in the steel

melts have the role of scavenging, deoxidization and grain refinement and so on.

For BMGs, the composition is known to be critical to their GFA and their properties. The minor addition technique has been widely applied to modify their compositions so as to improve the glass formation, thermal stability and properties of BMGs [101]. Table 2-2 lists some examples of minor additions in the field of BMG for different purposes.

Table 2-3 Some examples on minor additions in the field of BMG for different purposes

Function	Addictives	Base Alloy	Reference
Enhancing the GFA	Ni	$Ce_{70-x}Al_{10}Cu_{20}M_x$	[102]
	Al	$(Cu_{50}Zr_{50})_{100-x}M_x$	[103]
Scavenging the oxygen	Tb	$Mg_{65}Cu_{25}Tb_{10}$	[104]
Forming BMG-based composites	WC, SiC, W, or Ta	$Zr_{57}Nb_5Al_{10}Cu_{15.4}Ni_{12.6}$	[105]
	C	$Zr_{41}Ti_{14}Cu_{12.5}Ni_{10}Be_{22.5}$	[106]
Enhancing the thermal stability	C	$Zr_{41}Ti_{14}Cu_{12.5}Ni_{10}Be_{22.5}$	[107]
Enhancing the ductility	Ln	Fe-Mo-C-B-Ln	[108]
Improving the magnetic properties	Ni	$Fe_{61}Co_7Zr_{9.5}Mo_{5-x}Ni_xW_2B_{15.5}$	[109]
	Fe	$Pr_{60}Al_{10}Ni_{10}Cu_{20-x}Fe_x$	[110]

Although the GFA and properties of some BMGs have been successfully enhanced by the minor-alloying technique, the mechanism of the addition of minor elements still retains its mystique. For example, the approaches in fabricating bulk metallic glasses are still mostly empirical in nature. Some empirical rules are proposed as follows:

(1) Multi-component systems consisting of more than three elements;

(2) Significant difference in atomic sizes with the size ratios above about 12% for the three main constituent elements;

(3) Negative heats of mixing among the three main constituent elements [111, 112];

(4) “Confusion principle” [113];

(5) The alloy with a composition close to deep eutectic [53].

It is found that the alloys satisfying these empirical rules have special atomic configurations in the liquid state which is significantly different from those of the corresponding crystalline phases, and the atomic configurations favor the glass formation. The beneficial effects of minor additions on the glass-forming ability and the thermal stability satisfy these empirical rules, and can be understood in terms of thermodynamics, kinetics as well as the microstructural aspects. In the microstructure, the minor additions favor the formation of the unique atomic dense configurations with small free volumes, strong liquid behavior and high viscosity, which are significantly different from those for conventional metallic glasses. Thermodynamically, the minor addition makes the melts energetically closer to the crystalline state than other metallic melts due to their high packing density, in

conjunction with a tendency to develop short-range order. Kinetically, the minor addition makes the melts more viscous which leads to slow crystallization kinetics. Minor additions can also purify the melts and interfere with the nucleation and growth of the competitive crystalline phases of the glass [101].

Not only can the minor additions be used for improving the GFA, but also can be applied to tune the magnetic properties of the bulk metallic glass or its composites. Improvement of the soft magnetic properties in Fe-based bulk metallic glass is reported by adding a small amount of Ni. It is reported that without Ni addition, $Fe_{61}Co_7Zr_{9.5}Mo_{5-x}Ni_xW_2B_{15.5}$ (x=0) BMG doesn't exhibit soft magnetic behavior. However, with only 1 at% Ni addition, the alloy exhibits soft magnetic behavior. For x = 2% and 3% of Ni addition, the soft magnetic properties of the alloy are much improved without sacrificing the high GFA. The improved soft magnetic properties are attributed to the decreasing of antiferromagnetic interaction and the increasing of the exchange length by the addition of Ni [109].

The effect of minor additions is not only observed in magnetically soft bulk metallic glass, but is also found in magnetically hard bulk metallic glasses. The experimental M–H hysteresis loops of the $Pr_{60}Al_{10}Ni_{10}Cu_{20-x}Fe_x$ alloys at room temperature show a variation in coercivity, H_c, remanence, M_r and maximum energy product and $(BH)_{max}$ in a large range scale upon the change of Fe content from 0 to 20% [110]. Without Fe addition, the alloy exhibits a paramagnetic behavior at room temperature. However, only 4% addition of Fe makes the alloy become

ferromagnetic. It is also found that in the investigation, the improvement of the hard magnetic properties of the Pr-based alloy is not necessarily unidirectional with an increase of Fe. The coercivity will reach its maximum for an alloy containing 10% Fe. Any further addition of Fe will bring a decrease in coercivity. Based on the observations of the magnetic structure of the alloy, nanoparticles with similar magnetic orientation are found to be aligned to form a large-scale domain, and the inter-particle exchange coupling is considered to be the origin of magnetic properties in the alloy.

2.2.3.3 Cooling Rate

Among all the factors affecting the microstructure of BMGs, the cooling rate is believed to be the most decisive one. For example, Zhang et al. [114] have showed that different cooling rates can result in significantly different crystalline phases and/or microstructures, from a unique amorphous structure to complicated composites, in a La-based BMG-forming alloy. Loser et al. [115] have studied the cooling rate effects on the microstructure development of a Zr-based BMG forming alloy. Yan et al. [116] have also investigated the cooling rate, involving competition between the formation of the crystalline phase and the amorphous matrix in the microstructure of Zr-based BMGs.

For RE-based hard magnetic BMGs forming alloys, since their microstructure is found to be highly related to their coercivity, the effect of cooling rate on the

coercivity has been extensively investigated. Different cooling rates can be obtained by using different sample preparation methods such as melt-spinning, water-quenching and die casting, or by adjusting the process parameters such as the spinning speed of the melt-spinning process, and the mold diameter of the die casting process. It is worth mentioning that during the die casting process, the cooling rate will also vary from the periphery to the center region of a sample, which may achieve inhomogeneous microstructures..

In 1982, Croat applied the melt-spinning technique to obtain a coercivity about 7~9 kOe in an $Nd_{0.4}Fe_{0.6}$ alloy [117]. The largest coercivity is only obtained when the spinning speed is at a moderate value of about 5m/s. The spinning rate, too fast or too slow, will result in a decrease of the coercivity. It is believed that the dependence of H_c on spinning rate for rare earth-iron alloys is associated with the formation of a finely crystalline microstructure whose particle size changes with the cooling rate. Maximum H_c is considered to be obtained at a cooling rate which can achieve a particle size close to that of a single domain. However, a lower H_c can be obtained at higher or lower cooling rates with the superparamagnetic or multiple-domain effect, respectively.

Generally, magnetic anisotropy is observed in thicker ribbons melt-spun at low wheel speeds and it disappears at higher speeds [118,119]. However, in the investigation of the effect of cooling rate on the microstructure and the magnetic properties of $Nd_{60}Fe_{30}Al_{10}$ ribbons, an unusual magnetic anisotropy was reported by Croat et al. [120], in which the magnetic anisotropy disappeared when crystalline

phases were present in ribbons melt-spun at lower speeds. They have suggested that low cooling rates, i.e. low wheel speeds, will lead to formation of a mixture of Nd crystallites and a more stable Fe-rich amorphous phase. The precipitation of Nd from the amorphous phase results in non-magnetic Nd crystallites with a distinct texture and an isotropic magnetic Fe-rich amorphous phase. Based on the fact that the metastable phase Nd_5Fe_{17} in Mossbauer and X-ray diffraction experiments, which is suggested to be the origin of the large coercivity by others [121] is not detected, Wang et. al, have suggested that the large coercivity in the ribbon melt-spun at low speed is due to the presence of non-magnetic crystalline Nd, which can serve as pinning centers[122]. They have further investigated the microstructure and coercivity of partially amorphous and fully amorphous sample samples. Their results show that the high coercivity is mainly attributed to the amorphous phase from the low cooling rate, which contains Fe-rich clusters with large anisotropy.

The cooling rate induced variations in coercivity of the melt spun Nd-Fe-Si and Nd-Fe-Al ribbons were also discussed by Zhang et al. [123]. Nd-Fe-Si exhibits magnetic hard properties, whereas Nd-Fe-Al shows relative soft magnetic properties. The difference in the magnetic properties is attributed to the difference in the degree of relaxation of the amorphous structure. The amorphous structure is relatively more relaxed in Nd-Fe-Si alloys than in Nd-Fe-Al alloys. The appearance of high density clusters containing Nd-Nd and Nd-Fe pairs in the relaxed amorphous structure is believed to be the reason for high coercivity.

In 2003, more work was conducted by Sun et al. to study the microstructure, and

the thermodynamic and magnetic properties of $Nd_{60}Fe_{30}Al_{10}$ alloys prepared by different methods, i.e., arc melting, centrifugal casting and melt spinning [124]. According to their investigations, although the samples exhibit different morphologies due to the difference in the applied cooling rates, the existence of an “amorphous phase” responsible for the high coercivity is found not to be a single amorphous phase but a structure consisting of two separated amorphous phases with different compositions. This “amorphous phase” is very similar to the Nd-rich A1 phase observed in Nd-Fe binary alloys. The formation of such an A1-like amorphous phase is attributed to the positive heat of mixing between Nd and Fe and the metastability of the $NdFe_2$ intermetalic phase.

2.2.3.4 Low Temperature

Physical properties of some materials at low temperature usually exhibit great differences from those at room temperature. At low temperature, some physical phenomenon that cannot be observed at room temperature will become detectable due to the weakening of the thermal activation energy. There have been some investigations on the properties of BMGs at low temperature, such as electrical resistance and magnetic entropy [125-126]. The low-temperature magnetic behaviour of a series in heat-treated amorphous and nanocrystalline $Fe_{80.5}Nb_7B_{12.5}$ samples, with different volume fractions in the crystalline phase, has also been studied by Skorvanek et al.[127] The measurements of coercivity, initial susceptibility and magnetostriction

have been performed in a temperature range between 1.5 and 300 K. The coercivity of the nanocrystalline samples showed a minimum against the temperature, and the minimum is shifted to lower temperatures with an increasing volume fraction in the crystalline phase. A significant magnetic hardening behaviour, characterized by an abrupt upturn in coercivity, was reported for all nanocrystalline samples in the temperature range below 30 K. A reentrant spin-glass-like behaviour (or some other kinds of spin canting), which affects the soft magnetic properties at low temperatures, is believed to contribute to the changes in coercivity and the spin freezing mechanism can be applied to explain the observed abrupt magnetic hardening below 30 K.

For hard magnetic bulk metallic glass, the temperature dependence of the magnetic properties for $Nd_{60}Al_{10}Fe_{20}Co_{10}$ bulk metallic glass has also been investigated by Li et al.[128]. Their results indicate that $Nd_{60}Al_{10}$ $Fe_{20}Co_{10}$ bulk metallic glass exhibits permanent magnetic behaviour at room temperature. The coercive force and the shape of hysteresis loop changes markedly when the temperature decreases. A peak value is measured in AC magnetic susceptibility at about 18K. The moving of the peak value towards high temperatures with increasing frequency is explained as the results of the existence of spin glass structures in the bulk metallic glass.

2.3 Simulation of the Magnetic Properties of Bulk Metallic Glasses [129-131]

2.3.1 Introduction

With the rapid development of computer simulation, science is no longer simply divided into theoretical based and experimental based areas, and computer simulation as a third area is now independently studied. The importance of computer simulation methods should never be underestimated because computer simulation can fill the gap between theoretical and experimental study and give some useful answers to different problems. Besides, during computer simulation, some extreme conditions, beyond experimental capability, such as ultra-high pressure, and ultra-low temperature, can be easily determined by changing the simulation parameters.

In the field of computer simulation, the Monte Carlo (MC) method belongs to the method of randomization. Another frequently used method is the molecular dynamics method (MD), which resolves the problem in a definite way. The starting point of the MD method is to describe the microscopy of a physical system in a definite way. The MD method can be used to calculate the system properties by kinetic equations, and both the static and dynamic characteristics of the system can be investigated. Due to the dynamic characteristics, all degrees of freedom of the system must be considered in the MD method, and no random factor is allowed

during an MD investigation. However, differing from the MD method, the MC method is a random method built on the laws of statistics and the concepts of statistic mechanics. Besides, the Reverse Monte Carlo (RMC) method has also been employed in investigating the structure of hard magnetic bulk metallic glass, based on experimental results obtained from XRD, neutron and electron radiation experiments.

2.3.2 Monte-Carlo Simulation Method

2.3.2.1 Origin of Monte Carlo Method and its Characteristics

Monte Carlo is the capital city of Monaco, which is on the seashore of the Mediterranean. It is well-known around the world for its gambling industry. The similarity of the random sampling between the simulation methods and gambling is exactly the reason why this method is named after the city.

Although the method of random sampling is not new, it was not extensively applied in resolving real problems until1940s. During World War II, scientists in the Los Alamos Lab strove to produce a real nuclear weapon. However, it seemed not to be an easy task because there were still many complicated problems in the theory and technology. One is related to the neutron transport. In order to describe the process, a great deal of complicated differential and integral-differential coupled equations had to be resolved. The work on the neutron transport was completed by physicists such as von Neumann, Metropolis, Ulam and Kahn in Los Alamos. The

simulation of neutron behavior was performed on a computer by the use of random sampling. This random sampling method was named the Monte-Carlo Method. A report on this method from Metropolis and Ulam in 1949 announced the birth of the Monte Carlo method.

With the rapid development of computer technology, the MC method has been extensively applied to resolve physics problems. For example, it has been applied to simulate the classic statistical problem in equilibrium and non-equilibrium states, thin film growth and magnetic particle interaction problems. Recently, the applications of the MC method have been extensively reported, not only in the engineering discipline, but also in the economics discipline, which also contains the random sampling problems.

2.3.2.2 Mechanisms of Monte Carlo Method

Mathematic Support

Mathematically, the MC method is also called random simulation, random sampling or the statistic testing method. The basic principle of the method is, in order to resolve a mathematical, physical or chemical problem, a probability model or random process should be built, and the settled parameters give the answers to the problem. This process can be understood from the mathematic point of view. If a variable X is the mathematical expectation $E(\xi)$ of a random variable ξ, then in the MC method, N times of importance sampling will be done to the variable ξ,

and an independent value sequence of ξ, i.e., $\xi_1, \xi_2, \xi_3, ..., \xi_N$, will be generated. The arithmetic mean will be:

$$\overline{\xi}_N = \frac{1}{N}\sum_{i}^{N}\xi_i \tag{2-14}$$

according to the law of averages, for any $\varepsilon > 0$,

$$\lim_{N\to\infty} P(\left|\overline{\xi}_N - X\right| \geq \varepsilon) = 0, \tag{2-15}$$

i.e., $\overline{\xi}_N$ can be regarded as the estimated value of X

Random Numbers

During the MC simulation, an independent random sampling sequence should be given. The simplest way to get six random numbers is by casting a dice, or the random numbers can be obtained by special designed devices. With the computer, the random sequence is generated by different arithmetic operators. Two of the most popular methods are based on the linear recurrence methods. One is called the linear congruential generator, and the other is called the linear recurrence generator modulo or pseudo-random noise generator. In fact, the random sequence generator by computer is not strictly a real independent sequence, and it will repeat if enough time is given. However, with suitable parameters, the generated sequence can be used as independent random sequence, hence the sequence generated in this way is also called pseudo-random sequence.

2.3.2.3 Metropolis Algorithm

When studying systems with a great many particles, it becomes clear that the number of possible configurations becomes exceedingly large very quickly. Even for extremely simple binary models, in which each particle may exist in one of two possible states, the number of configurations of the system grows extremely rapidly with N, the number of particles. For example, consider a simple Ising model of magnetic spin. If the system configuration is N=32*32, i.e., 1024 spins in the system, and each spin has two values, 1 or -1 describe two different states of the spin. So for the system, there are 2^{1024}, i.e. about 10^{308} types of states. In fact, the configuration of a real system is exceedingly larger than 1024, and it is far beyond the capability of the most advanced computer to complete a calculation.

In the Metropolis algorithm, a random walk will be performed through the configuration space. The walk is designed so that the points on the walk are distributed according to the required probability distribution. At each point on the walk, a random trial move from the current position in the configuration space is selected. This trial move is then either accepted or rejected according to a simple probabilistic rule. If the move is accepted then the “walker” moves to the new position in the configuration space; otherwise the “walker” remains where it is. Another trial step is then chosen, either from the new accepted position or from the old position if the first move was rejected, and the process is repeated. In this way, it should be possible for the “walker” to explore the whole configuration space of the

problem. The Metropolis algorithm provides a prescription for choosing which moves in the configuration space to accept or reject.

In a system with *D* degrees of freedom, for example, the thermal average of a quantity A associated with each microstate of the system in equilibrium at absolute temperature T is given by

$$< A >= \frac{1}{Z}\int A(x)e^{-\frac{E(x)}{k_B T}}\,dx \qquad (2\text{-}16)$$

where x is a point in *D*-dimensional space and represents the state of the system, $E(x)$ is the energy of state x, $Z = \int e^{-\frac{E(x)}{k_B T}}\,dx$ is the partition function. In order to simplify the calculation, the units of the Boltzmann constant will be set as one (k_B = 1). In the case of particle models where the system space is discrete, the integral in the above equation is replaced by a sum over all space:

$$< A >= \frac{1}{Z}\sum_x A(x)e^{-\frac{E(x)}{T}} \qquad (2\text{-}17)$$

where different states *x* of the system correspond to different positions, and the partition function is

$$Z = \sum_x A(x)e^{-\frac{E(x)}{T}}\ . \qquad (2\text{-}18)$$

In the case of very small systems, all positions can be enumerated and the thermal averages (as well as extensive quantities such as entropy and free energy) can be computed exactly by Eq.2-17. For large systems, however, a complete enumeration of the points in a system is impossible, with contemporary computers.

In MC simulations, this difficulty is solved by replacing the set of positions in Eq. 2-17 by a representative tractable subset of M conformations, where M is much smaller than the total number of conformations, N. An estimate for the thermal average $< A >_{est}$ is then obtained as follows:

$$< A >_{est} = \frac{\sum_{l=1}^{M} A(x_l) e^{-\frac{E(x_l)}{T}}}{\sum_{l=1}^{M} e^{-\frac{E(x_l)}{T}}} \qquad (2\text{-}19)$$

It is clear that the accuracy of the estimate will depend directly on the quality of the representative subset of the M system. In a simple sampling method, for example, where the M are chosen randomly, most of the system will have energy very different from the average energy of the system at a temperature T, and their contribution to the estimate will be insignificant. The estimate obtained by simple sampling would be, therefore, very inaccurate, unless M becomes as big as N, or even larger.

The idea of importance sampling in MC simulations is to choose the representative system set not completely at random, but in such a way that the selection is somehow biased towards a system that is significantly populated at equilibrium. In general, if the probability at a given conformation x_l appears in the sample representative of conformations is $P_{samp}(x_l)$, then Eq. 2-19 becomes:

$$< A >_{est} = \frac{\sum_{l=1}^{M} \frac{A(x_l) e^{-\frac{E(x_l)}{T}}}{P_{samp}(x_l)}}{\sum_{l=1}^{M} \frac{e^{-\frac{E(x_l)}{T}}}{P_{samp}(x_l)}} \qquad (2\text{-}20)$$

In particular, if the conformations are chosen with probability $P_{samp}(x_l) \propto e^{-\frac{-E(x_l)}{T}}$, then the Boltzmann factors cancel out and the estimate for the thermal average becomes:

$$< A >_{est} = \frac{\sum_{l=1}^{M} A(x_l)}{M} \qquad (2\text{-}21)$$

Samples of representative conformations with this particularly convenient property, where the probability of occurrence of a given conformation is proportional to its Boltzmann factor, can be generated by the Metropolis algorithm. The algorithm constructs a Markov chain of conformations, where the first conformation, x_1, is arbitrarily chosen (e.g., randomly) and an appropriate probability function, $W(x_{i-1} \to x_i)$, is used to construct each conformation x_i, from the previous conformation x_{i-1}. $W(x_{i-1} \to x_i)$ is the probability of a "walk" from conformation x_{i-1} to conformation x_i. In general, to make such a chain of conformations converge to the desired canonical distribution which is sufficient (but not necessary) to impose the condition of detailed balance, the following equality must hold for any arbitrary pair of conformations, x_l and x_m,

$$P_{eq}(x_l) W(x_l \to x_m) = P_{eq}(x_m) W(x_m \to x_l) \qquad (2\text{-}22)$$

where $P_{eq}(x) = \frac{e^{-\frac{E(x)}{T}}}{Z}$ is the equilibrium probability of conformation x.

The condition of detailed balance given by Eq. 2-22 implies that, at equilibrium, the average number of moves $x_l \to x_m$ is the same as the average number of inverse moves $x_m \to x_l$. If the system is not in equilibrium then the ratio between the probabilities of any two conformations tends to increase if it is initially below its equilibrium value and to decrease if it is initially above its equilibrium value. It follows that for sufficiently long simulations, the system will reach thermodynamic equilibrium.

It is usually convenient to restrict the possible moves from a particular conformation only to a restricted number of "adjacent" conformations. The condition of detailed balance of Eq.2-22 requires the following for any two conformations x_l and x_m:

1. If $W(x_l \to x_m) = 0$ then

$$W(x_m \to x_l) = 0;$$

2. If $W(x_l \to x_m) \neq 0$ then

$$\frac{W(x_l \to x_m)}{W(x_m \to x_l)} = \exp(-\frac{E(x_m) - E(x_l)}{T}) \qquad (2\text{-}23)$$

So, a walk from one conformation to another is possible if, and only if, the inverse move is also possible, or, in other words, two arbitrary conformations must be necessarily either mutually adjacent or not adjacent. Also if two conformations

are mutually adjacent then the probability of a move between them is related to the probability of an inverse move by a well defined relation, dependent only on the difference in energy between the two conformations.

The rules that determine which conformations are adjacent to any arbitrary conformation are given by the “move set” used in the simulation. As long as the detailed balance is respected, the particular move set should have no effect on the equilibrium canonical distribution reached after a sufficiently long time but it can have drastic effects on the rate at which this equilibrium distribution is reached. An appropriate move set, where adjacent conformations are not very different from each other, also permits a dynamic interpretation of the Markov chain of conformations generated during the simulation, according to which the number of conformations generated is considered to be proportional to time. According to these considerations, therefore, thermodynamic properties of the system are independent of the particular choice of move set but kinetic properties are not.

The Metropolis algorithm can be summarized as follows. The first conformation is randomly generated. At each point in the construction of the chain of conformations, a move is attempted to the current conformation. The move is rejected immediately if the local chain conformation is not compatible with the attempted move or if it violates the excluded volume condition. If these two conditions are satisfied then the so called Metropolis criterion is applied. If the difference between the energy of the resulting conformation and the energy of the

current conformation, ΔE, is negative (i.e. the energy of the resulting conformation is smaller than the energy of the current conformation), then the resulting conformation is accepted and it becomes the new conformation in the chain. If ΔE is positive, however, a (pseudo)random number between 0 and 1, 0<R<1, is generated and the resulting conformation is only accepted if $e^{-\Delta E/T} > R$. If $e^{-\Delta E/T} < R$ then the resulting conformation is rejected. Whenever the conformation resulting from the attempted move is rejected for any of the three possible reasons, then the new conformation of the chain is the same as the current conformation. For sequence selection, the same algorithm is used but the "walk" corresponds to switching the position of two monomers while the conformation is kept fixed.

The Metropolis criterion can be also summarized by the following expression for the probability of acceptance of an attempted conformation:

$$P_{accept} = \min(1, e^{-\Delta E/T}) \qquad (2\text{-}24)$$

Note that the ratio between the acceptance probabilities of a move is related to the acceptance probability for the inverse move by the same relation presented in Eq.2-24. As the transition probability between two conformations is the product of the probability of attempting a given adjacent conformation, $P_{attempt}$, and the probability of accepting the conformation P_{accept}, then the detailed balance condition is only valid with the described algorithm because $P_{attempt}$ is constant. This is the reason why local moves that are not compatible with the chain conformation or violate the excluded volume condition must be considered during the choice of

conformation to be attempted in the simulation in conformational space, even if they will always be rejected. If, for example, the choice of local moves were restricted a priori to moves compatible with the local conformation of the chain at the bead where the move is being attempted, then $P_{attempt}$ would depend on the number of such possible moves and would be different for different conformations.

In the present study, averages estimated from long MC trajectories by Eq. 2-22 are considered to be good estimates for the true thermodynamic average, so that $< A >_{est} \approx < A >$ and the subscript is not used to distinguish estimates from real thermal averages.

2.3.3 Monte-Carlo Simulation in Magnetic Bulk Metallic Glasses

It is well known that magnetic behavior is a very complicated process involving the interaction between magnetic particles and anisotropy of individual particles. The magnetization process is sensitive to many factors such as the particle size, the prevailing temperature, and the external field. Since these factors are not easy to control by experiment, it is useful to use the Monte-Carlo simulation method to investigate the process, as it can describe the random process of the interaction between the particles. Moreover, the random process can be controlled by adjusting the parameters.

Up to now, much simulation work on studying magnetic nanoparticles has been

done by the MC method [132-137]. With respect to bulk metallic glasses, relatively few efforts have been devoted to investigating their hard magnetic properties. The most common approach for the investigation of hard magnetic properties of amorphous materials is the random magnetic anisotropy model proposed by Harris et al.[83]. In their model, the magnetic properties of the amorphous materials are determined by the interaction between spins and the anisotropy energy of the spins. This model has been successfully used to explain the magnetic behavior of many amorphous materials based on the fact that the studied materials must be uniform in amorphous structure.

However, for rare earth based magnetically hard bulk metallic glasses, it is reported that their microstructures are usually not homogeneous. Structure or chemical composition imhomogeneities, such as amorphous phase separation and the precipitation of nanocrystalline or nanoclusters have been reported in these BMGs. Ding et al have improved the random anisotropy model by introducing the anisotropy energy of the clusters and the interaction between the clusters into inhomogeneous amorphous magnetic materials, such as Nd-Fe-Al bulk metallic glass. Based on this model, they have carried out Monte Carlo simulation to study the magnetic cluster behavior. Their simulation results suggested, besides each cluster possessing a certain Curie temperature, two other critical temperatures, the blocking temperature originated from the anisotropy energy of the cluster and the system Curie temperature, are also found in the system. Their simulation results also show that the coercivity at low temperature is determined by the anisotropy energy,

and the interaction between clusters has a little effect on the coercivity [138].

Based on the experimental magnetic results, the microstructure of Nd-Fe-Al bulk metallic glass was simulated by the reverse Monte Carlo method using neutron diffraction data by Lupu et al., in 2004[139, 140]. According to their findings, the microstructure, containing small clusters or medium-range ordered regions of 2-3nm, embeded in an amorphous matrix, is closedly related to the magnetic properties. Their results also show that the distribution of the clusters is more homogeneous in thick samples, which leads to a higher magnetic percolation limit and an increase of the coercivity field from 1 to 2 T for thin samples 25 μm in thickness to 7-8 T for thick samples of 2 mm in diameter. The hypothesis that the iron clusters play a key role in the ditermination of the magnetic properties of the bulk metallic glasses and their temperature dependence also agrees with the experimental observations.

Even though little work has done in the simulation of hard magnetic properties of bulk metallic glasses, it is worthwhile to use the simulation method to gain a better understanding of hard magnetism in bulk metallic glasses.

Chapter 3 Experimental Procedures

3.1 Sample Preparation

3.1.1 As-cast Samples

Conventional metallic glasses prepared by melt spinning are always in ribbon shape due to the necessary high cooling rate (about 10^6K/s) achieved from the melt spinning equipment. However, bulk metallic glasses can be prepared at relative low cooling rates of about several hundred degrees Kelvin per second. Various methods have been developed to prepare bulk metallic glasses, such as water quenching [141], high-pressure die casting [142], and copper mold casting [143] processes. In this study, the arc melting/copper mold casting method is employed to prepare samples in bulk forms. Figure 3-1 shows the schematic diagram of the equipment. Alloy ingots can be melted by an electrode induced arc in the water cooled copper hearth in an argon atmosphere. The molten alloy can be sucked into a copper mold by a negative pressure with respect to the pressure in the heating chamber.

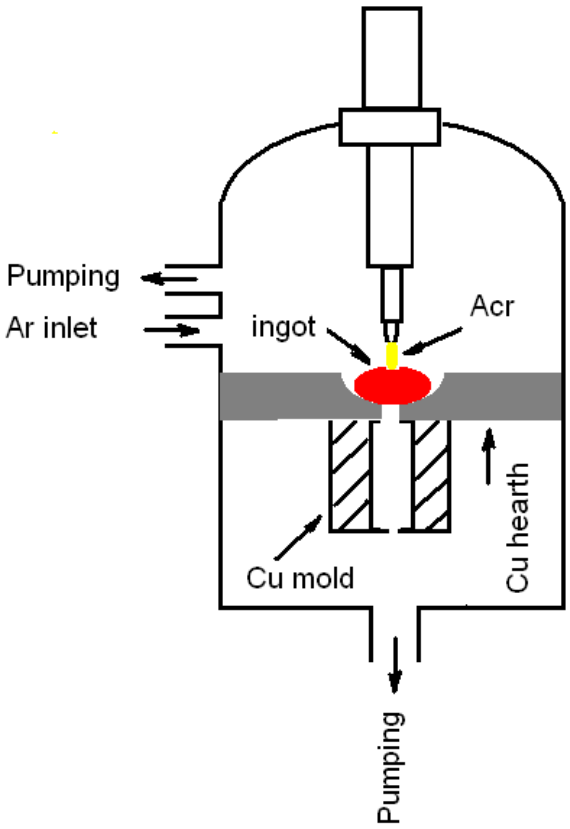

Figure 3-1Schematic diagram of arc melting/copper mold casting

In this project, master alloys with nominal composition $(Nd_{60}Fe_{30}Al_{10})_{100-x}Ni_x$, with X=0, 1, 3, 5, 8, 10, were prepared by arc melting of the raw materials in a Ti-gettered argon atmosphere. The starting materials were Nd, Fe, Al and Ni metals with a purity of 99.9% (wt). Ingots were remelted several times to ensure the homogeneity of the compositions, and then cooled down naturally in the heating chamber. Cylindrical samples of the diameters 3mm and 2mm were synthesized in one copper mold by casting the molten alloy into a water-cooled copper mold in an argon atmosphere. In this project, in order to ensure consistency, only specimens with a diameter of 3mm were selected for detailed investigation. Figure 3-2 shows

the surface appearance of the as-cast $(Nd_{30}Fe_{60}Al_{10})_{100-x}Ni_x$ (x=0, 3, 5, 8, 10)) alloys of diameters 3 and 5 mm.

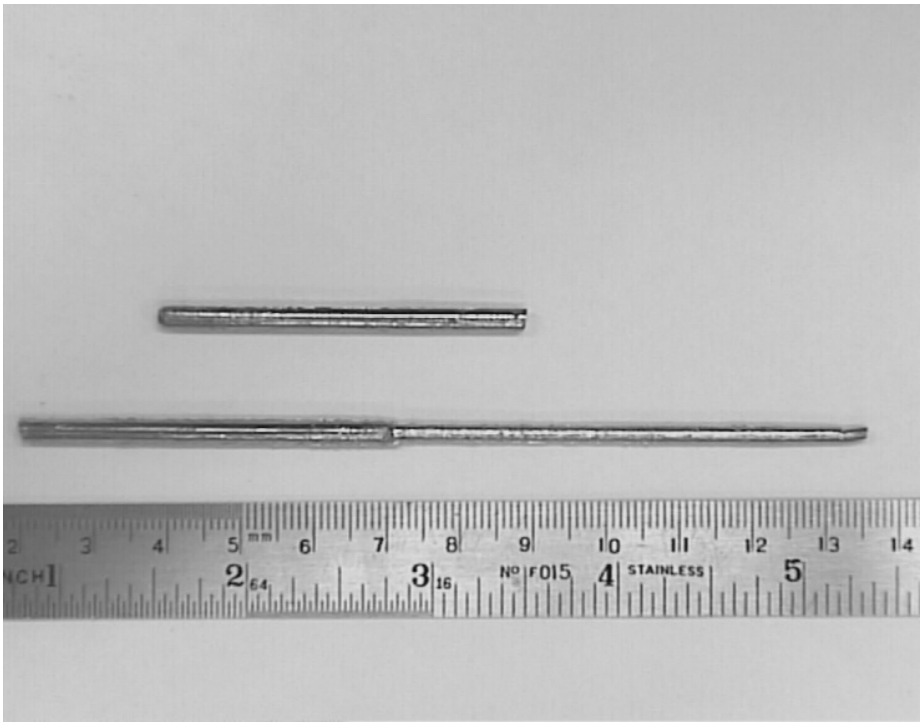

Figure 3-2 The surface appearance of the as-cast $(Nd_{30}Fe_{60}Al_{10})_{100-x}Ni_x$ (x=0, 3, 5, 8, 10)) alloys with diameters of 3 and 5 mm

3.1.2 Annealing Treated Samples

In order to achieve different microstructures, various annealing treatments were applied. In this study, the annealing treatment was conducted in a graphite type resistance-heating furnace. The process is as follows: (1) samples were encapsulated in a vacuumed silicon tube by an acetylene flame; (2) the tube was placed into a furnace at a selected temperature for a designed time scale; (3) the tube was quenched into water.

3.2 Characterization Methods

3.2.1 Microstructure

X-ray Diffraction (XRD)

The structure and phases of BMGs were identified by X-ray diffraction (XRD, Philips Xpert) with the radiation of Cu K α. Samples were crushed into powders by grinding to ensure that the whole structure could be examined.

Optical Microscopy (OM)

As a preliminary observation of the morphology of the samples, optical microscopy was employed. Samples for optical microscopy observation were polished in water without etching.

Scanning Electron Microscopy (SEM) and Energy Dispersive X-ray Spectrum (EDX)

The microstructure was examined by scanning electron microscopy (SEM, Leica Stereoscan 440), in the backscattering mode. The EDX conjunct to SEM was employed to identify and quantify the chemical composition of the samples.

Transmission Electron Microcopy (TEM)

The microstructure was also examined by transmission electron microcopy (TEM, Jole-2010 with energy dispersive spectroscopy (EDX)). In this study, bright

field and dark field images were obtained together with the diffraction patterns for the examination of local microstructures.

Cross-section TEM samples were prepared mainly in three steps. A thin disc, about 1mm in thickness, was cut from 3mm diameter bar by a water cooled diamond blade saw, and then pre-thinned mechanically using a tripod polisher. The final thinning was performed by ion milling, with the protection of liquid N_2.

3.2.2 Thermal Properties

Differential scanning calorimeters (DSC, Perkin Elemer DSC7 for temperature ranging from room temperature to 825K, and Netzch STA 449C for temperatures ranging from room temperature to 1100K) were used to determine the glass transition temperature (T_g), the crystallization temperature (T_x) and the melting temperature (T_m). DSC measurements were performed at constant heating rates of 2K/min, 5K/min, 10K/min, 20K/min, 40K/min and 60K/min in a flowing Ar atmosphere. The DSC curve was substrated by a baseline (DSC scanning curve with empty pans under the same heating process) and then normalized by the mass of the samples.

3.2.3 Magnetic Structure and Properties

Vibrating Samples Magnetometer (VSM)

The basic magnetic properties, such as saturation magnetization (M_s),

remanence (M_r), and coercivity(H_c) can be obtained from a M-H hysteresis loop by a vibrating sample magnetometer (VSM). The VSM used in this study was 7300VSM (Lakeshore), and 9Tesla superconducting VSM (Oxford Instrument). M-H hysteresis loops were measured by the VSM at an applied field of 1.5Tesla at room temperature. Flake like samples of 3mm diameter and 1mm thickness were cut from the alloy by a water-cooled diamond blade saw. Due to the large magnetization and coercity at low temperatures, samples of small size were used during the measurement of magnetic properties at low temperatures to avoid the data overflowing. In this study, powder samples of about 10 mg were obtained by crushing the samples in a grinder. The temperature dependence of magnetization and coercivity, for temperatures ranging from room temperature to a low temperature of 60K, was investigated by using a superconducting VSM under an external field of 5 Tesla.

Magnetic Force Microscopy (MFM)

A study of the domain structure was carried out by using magnetic force microscopy (MFM, Digital Instruments NanoScope IV) [144, 145]. It allows the topographic and magnetic force images to be collected separately and simultaneously in the same area of the sample by using tapping/lift modes. For the dynamic detection mode, the cantilever was vibrated and its resonant frequency f_0 and phase ϕ were modulated by the magnetic forces exerted on the tip from the stray field H which emerged from the magnetic structures in the sample surface layer when the tip was scanning. In the magnetic force images detected by the phase mode, the dark and bright regions correspond to the attractive and repulsive tip-sample

interactions, respectively. In the experiments, the tip was magnetized upwards prior to imaging. The frequency f_0 was 80.6 kHz, and its lift-height during scanning was 100 nm.

Chapter 4 Effect of Minor-alloying Ni on Glass Forming Ability, Microstructure and Magnetic Properties of Nd-Fe-Al Alloys

4.1 Introduction

Among various rare earth-transition metal (RE-TM) based BMGs, Nd based BMGs have been extensively studied. Recently, a Nd based BMG with good GFA (with diameters up to 15mm) has been produced by Inoue et al. [146]. Its high GFA is considered to be related to its high reduced crystallization temperature T_{rx}. Like other Nd-based BMGs, this alloy also exhibits no apparent glass transition temperature or supercooled liquid region [5, 6, 11, 146]. While Sun et al. have proposed that the absence of the glass transition temperature is due to the continuous growth of the Nd nanocrystalline phase [148], Wei et al. [156] have attributed this to the continuous occurrence of glass transition in a large temperature scale.

More recently, minor alloying has been found to be an effective way to improve the properties of different BMG systems [10, 150-152]. For example, Ni has been introduced to some Fe or Zr based alloys to enhance their soft magnetic properties [90], ductility [153] and fatigue resistance [154]. However, the effect of Ni addition on the glass forming ability and magnetic properties of rare earth based BMGs have yet to be examined.

In this chapter, discussion of $(Nd_{60}Fe_{30}Al_{10})_{100-x}$ Ni_x (where x= 0, 3. 5, 8, 10 at%) alloy cylinders, with a diameter of 5mm, prepared by copper mold casting is made. The effect of Ni addition on glass forming ability, thermal stability and magnetic properties of the Nd-based alloys are investigated using X-ray diffraction, scanning electron microscopy, differential scanning calorimetry and vibrating samples magnetometer. The investigation is important for better understanding of the mechanism of forming ability, and the designing of bulk metallic glasses of good thermal stability and properties.

4.2 Results and Discussion

4.2.1 Microstructure

The structure of as-cast $(Nd_{60}Fe_{30}Al_{10})_{100-x}Ni_x$ (where x=0, 5, 8 and 10) alloys with different concentrations of Ni was examined by XRD and is shown in Figure 4-1. Without Ni addition, some weak diffraction peaks were detected over the broad amorphous diffraction hump, suggesting the existence of a small amount of crystalline phases including Nd, Fe in the amorphous matrix. This result is different from that of the alloys with the same composition published by Inoue et al., who reported full amorphous structure in the alloys, with a diameter up to 12mm [35]. This variation might result from the difference in the purity of the starting materials and in the experimental conditions. However, with 5% Ni addition, the diffraction peaks corresponding to the precipitation of Nd crystalline are weakened and the volume of the amorphous phase increases. While adding about 8% of Ni, diffraction peaks corresponding to crystalline phases almost disappear, indicating the formation of a nearly full amorphous structure in the alloy. However, two diffraction humps peak around $2\theta \approx 32^{o}$ and $2\theta \approx 55^{o}$ can be observed in the XRD patterns, suggesting that the alloy involves two kinds of short range ordered structure, including amorphous phases or nanoscale clusters with different compositions. The formation of two short distance ordered structures is probably due to the occurrence of phase separation during the solidification of the molten alloy. A similar result was also

reported previously by Kumar et al [155]. However, with Ni content up to 10%, some new diffraction peaks reappear, illustrating that excessive Ni will weaken the glass forming ability of the base alloy. The new phases are identified to be crystalline Nd and other unknown phases.

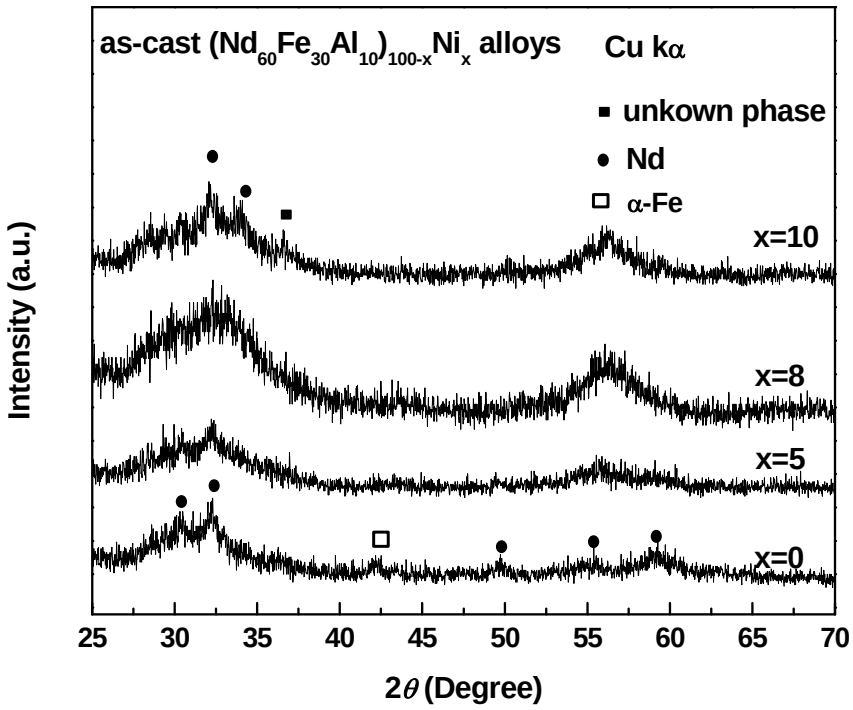

Figure 4-1XRD patterns of the as-cast $(Nd_{60}Fe_{30}Al_{10})_{100-x}Ni_x$ (x=0, 5, 8 and 10) alloys

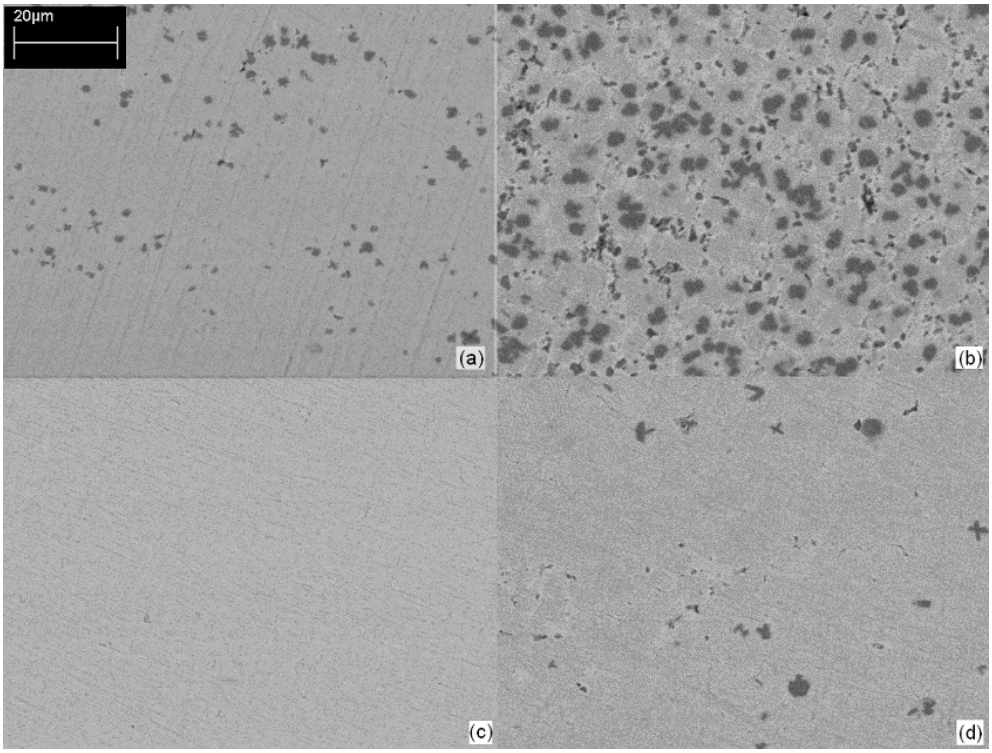

Figure 4-2 Cross-section morphologies of the as-cast $(Nd_{60}Fe_{30}Al_{10})_{100-x}Ni_x$ alloys; (a) x=0, at the periphery of the cross-section; (b) x=0, at the center of the cross-section; (c) x=8, at the periphery of the cross-section ;(d) x=8, at the center of the cross-section

Figure 4-2 shows the morphologies observed at the edge and in the central regions of the specimens, with 0 and 8% of Ni. An apparent transition in structure from the periphery to the center of cross-section is observed in the Ni free alloy. An almost featureless region was found at the periphery of the cross-section, indicating that the amorphous phase is mostly formed in the region (Figure 4-2(a)). While three different phases, namely, a dark phase, a white network-like phase and a gray matrix can be observed in the central region (Figure 4-2 (b)). The dark phase always appears in the center of most of the gray phase. The dark phases enclosed by the gray

phase are about 5μm in size. However, difference in the morphologies is relatively small between the edge and center of the cross-section for the sample with 8% Ni, though a small white phase and an insignificant dark phase are still observed in the center of cross-section (Figure 4-2(c) and (d)). The amount of both dark and white network-like phases is found to decrease with an increasing amount of Ni. As the XRD results have revealed an almost fully amorphous structure for the sample with 8% of Ni and a partial amorphous structure for the Ni free alloy, the gray phase is considered to be the amorphous phase, and the dark and white network-like phases to be Fe and Nd crystalline phases, respectively. The changes of the amorphous phase in the Ni free alloy should be the result of different cooling rates from the surface to the center of the cylindrical sample. The cooling rate in the center of the cylinder is not large enough to freeze the molten alloy into an amorphous structure in this region. Details of the effect of cooling rate on glass forming ability are discussed in Chapter 5.

4.2.2 Thermal Behavior

Figure 4-3 shows DSC scans of the as-cast $(Nd_{60}Fe_{30}Al_{10})_{100-x}Ni_x$ (x=0, 5, 8 and 10) alloys at a heating rate of 10K/min. The inset shows the high temperature DSC curve of the alloy with 8% of Ni. Without Ni, the DSC trace exhibits an obvious exothermal characteristic of crystallization at $T_x \approx 772K$. No appreciable endothermal reaction corresponding to glass transition is found prior to the crystallization

temperature. The melting temperature that was measured by high temperature DSC is about 953K in the alloy without the addition of Ni. However, with 5 % of Ni content, the melting temperature is reduced and is close to the crystallization temperature. With a further increase in the content of Ni to 8%, the temperature of the endothermal peak is found to be even lower than the exothermal peak, which suggests the melting process occurs before the crystallization process. This anomalous result may be due to the phase separation of the amorphous structure in the as-cast alloys, which leads to the formation of two amorphous phases with different crystallization and melting temperatures. During heat scanning, one of the amorphous phases can melt even before the crystallization of another phase. When the content of Ni further increases to 10%, this anomalous phenomenon disappears, although the melting and crystallization temperatures are still very close.

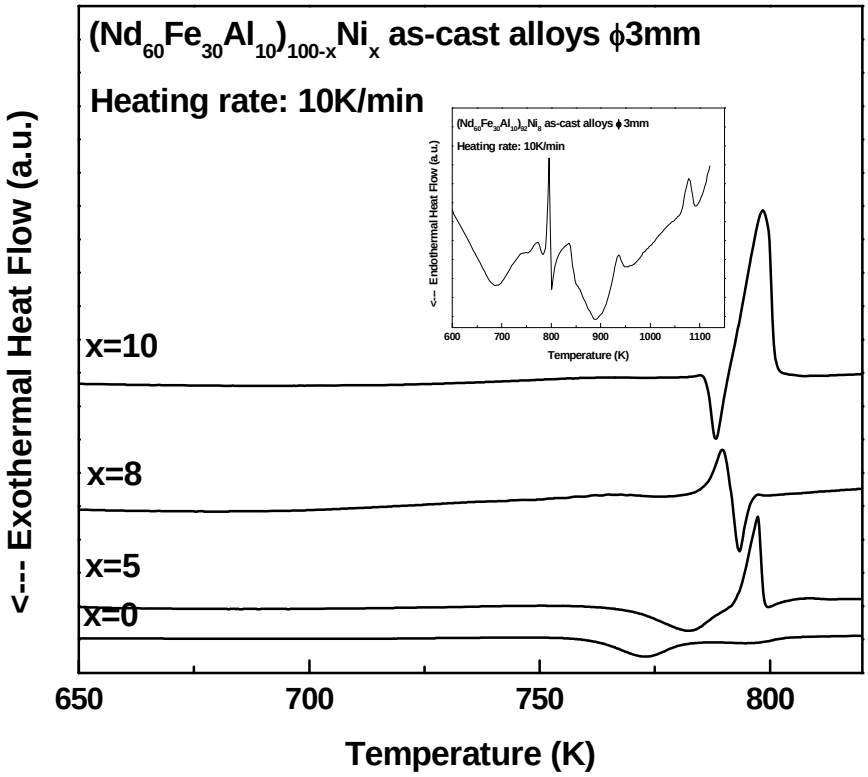

Figure 4-3DSC curves of $(Nd_{60}Fe_{30}Al_{10})_{100-x}Ni_x$ (where x=0, 5, 8 and 10) alloys at a constant rate of 10K/min. Inset shows the high temperature DSC result of $(Nd_{60}Fe_{30}Al_{10})_{92}Ni_8$ alloys

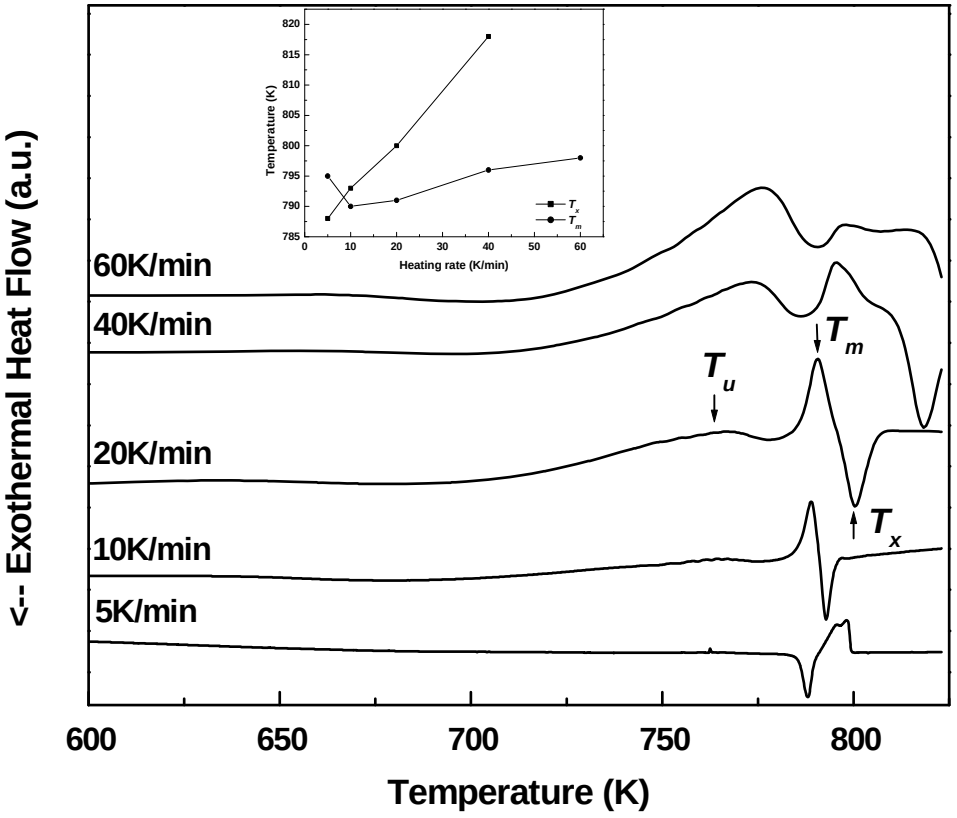

Figure 4-4DSC curves of the as-cast $(Nd_{60}Fe_{30}Al_{10})_{92}Ni_8$ alloys at 5, 10, 20, 40 and 60K/min. Inset shows the variation of T_x and T_m as function of heating rate.

A DSC analysis was also employed to investigate the effect of heating rate on the kinetics of crystallization and the melting of the as-cast $(Nd_{60}Fe_{30}Al_{10})_{92}Ni_8$ alloy. Figure 4-4 shows the DSC scans at heating rates of 5, 10, 20, 40 and 60 K/min. The inset shows the variation of T_x and T_m as a function of heating rate. At a heating rate of 5K/min, the crystallization temperature and the melting temperature are 788K and 795K, respectively. With an increase in the heating rate, the exothermic peak shifts to a temperature higher than the endothermic peak. When the heating rate is 60K/m, the exothermic peak overlaps with the endothermic peak, indicating that the alloy

tends to melt before any exothermal transformation process. It is noted that another endothermic process occurs prior to the exothermal peak appearing, which may result from the glass transition process. It is however, difficult to identify an obvious glass transition temperature at a low heating rate, such as 5K/min, and a continuous glass transition process may account for this phenomenon. As a consequence of the inhomogeneity of the composition of the alloy, glass transition will occur on a large time scale when the heat scanning rate is low, and the whole process will consist of small continuous steps which result in a dispersed peak as shown in Figure 4-4. With an increase in heating rate, the glass transition process has to take place in a relatively short time, which will result in the formation of a more obvious endothermal peak for glass transition.

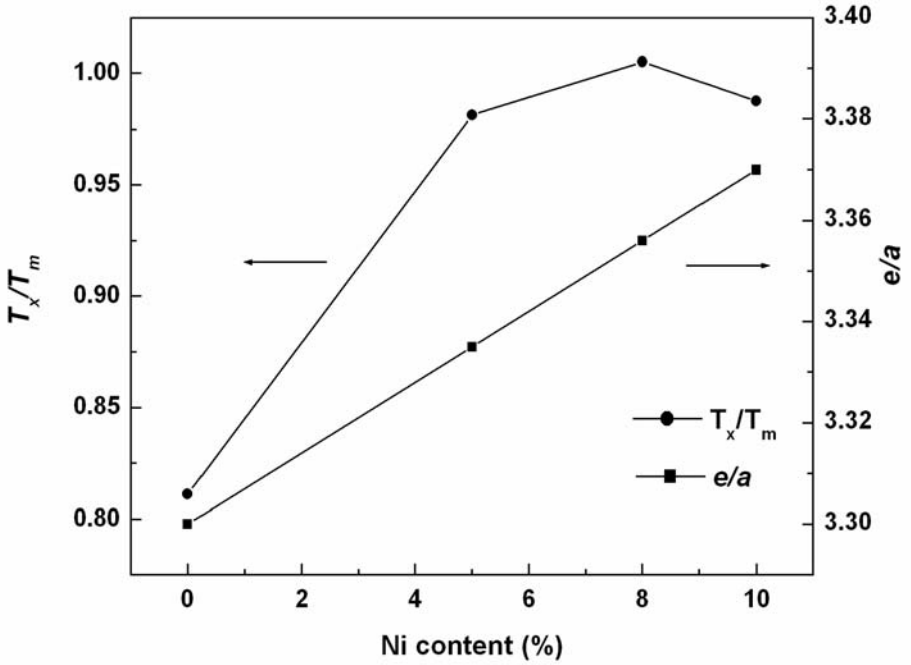

Figure 4-5 Reduced crystallization temperature and valence electron concentration of the as-cast $(Nd_{60}Fe_{30}Al_{10})_{100-x}Ni_x$ (where x=0, 5, 8 and 10) alloys with the variation of the amount of Ni

In order to further understand the thermal stability and glass forming ability of

this bulk metallic forming system, Figure 4-5 shows the change of the reduced crystallization temperature $T_{rx}=(T_x/T_m)$ and the valence electron concentration e/a as a function of Ni in $(Nd_{60}Fe_{30}Al_{10})_{100-x}Ni_x$ alloys. Without the addition of Ni, the value for $Nd_{60}Fe_{30}Al_{10}$ alloys is about 0.81, which is slightly below 0.85, for the same composition reported by Inoue [5]. The difference in T_{rx} might result from the difference in starting materials and/or process conditions. However, T_{rx} has significantly increased to 0.98 when the Ni content is 5%. It even goes up to 1.01 when Ni content increases to 8%. These high T_{rx} values may be related to the high glass-forming ability of the alloys. The GFA of alloys with Ni addition is enhanced as compared to that of Ni-free alloy. It is considered that the anomalous high T_{rx} (>1) value is related to the existence of separated amorphous phases with different thermal stabilities.

4.2.3 **Valence Concentration and Magnetic Properties**

A valence concentration criterion e/a (e and a are the valence and atom number in a unit cell, respectively) was proposed by Jiang to understand the effect of Ni addition on enhancing GFA [48]. Deduced from the Hume-Rothery rule [47], the valence concentration criterion proposed that e/a should be close to 3.5 to form a bulk metallic glass. The valence electron numbers of Nd, Fe, Al and Ni elements are 3, 4, 3 and 4, respectively, and the e/a value for $(Nd_{60}Fe_{30}Al_{10})_{100-x}Ni_x$ is determined by the algebra sum of the compositions of the alloys. The values of e/a are 3.300,

3.335, 3.346 and 3.370, for the alloys with the Ni contents of 0, 5, 8 and 10%, respectively, which shows a tendency to increase with Ni addition. The enhanced GFA may also be understood from the structure aspects. According to the theory of the “confusion principle” proposed by Greer and Desré [156-158], increasing the number of components in a liquid glass forming alloy will inhibit intermetallic nucleation, thus enhancing the glass-forming ability, and the fluctuations in the undercooled liquid can help intermetallic nucleation under an appropriate range of temperature and concentration. The addition of one component is known to lower the probability of creating a nucleation fluctuation by a factor of ten. In this study, with the addition of Ni, the alloy becomes more “confused” from a ternary to a quaternary system and the Ni atoms with different sizes in an alloy will make the redistribution of atoms on a long range scale difficult during the cooling process. However, the GFA cannot be further improved by adding more Ni , and may be the result of the precipitation of Nd evoked by the excessive Ni addition.

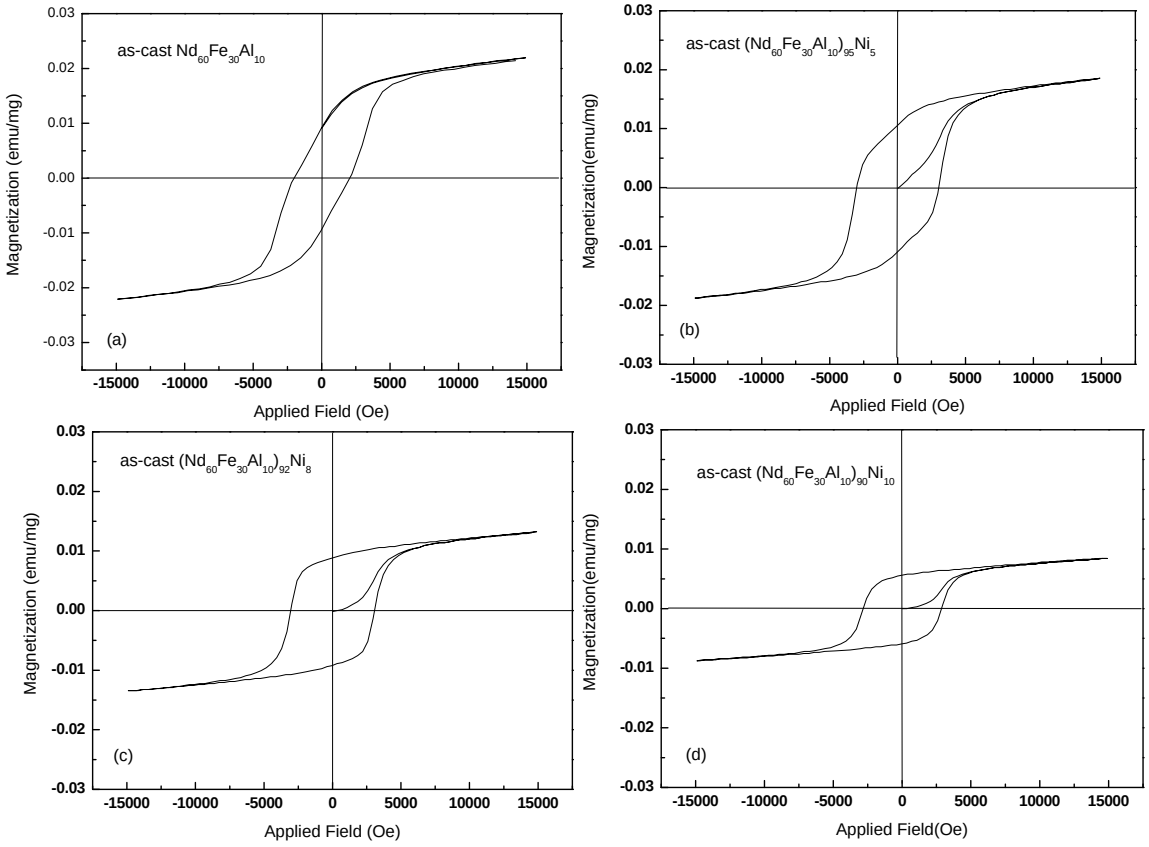

Figure 4-6 Hysteresis loops of the as-cast $(Nd_{60}Fe_{30}Al_{10})_{100-x}Ni_x$, (a) $Nd_{60}Fe_{30}Al_{10;}$ (b) $(Nd_{60}Fe_{30}Al_{10})_{95}Ni5$; $(Nd_{60}Fe_{30}Al_{10})_{92}Ni_8$; $(Nd_{60}Fe_{30}Al_{10})_{90}Ni_{10}$

Figure 4-6 shows the M-H curves of the as-cast $(Nd_{60}Fe_{30}Al_{10})_{100-x}Ni_x$ (x=0, 5, 8 and 10) alloys. It is found that, during the demagnetization, the shape of the hysteresis loop of the Ni free alloy is relative irregular with respective to those alloys with Ni. The irregular shape may be related to the mixture having more than two magnetic phases with different magnetic properties in the Ni free alloy. With the addition of Ni, the magnetization will be weakened. However, the coercivity will increase with the addition of Ni. The change in coercivity may be related to the non-magnetic phases that act as pinning centers or the increase of amorphous phases in the glass forming ability of the improved alloy [92]. With the addition of Ni into

the alloy, the content of the amorphous phases will also increase (see Figure 4-1). At the same time, the non-magnetic phases in the alloy will become more homogeneous in the distribution in the alloy, as shown in Figure 4-2.

4.3 **Conclusions**

The effect of Ni addition on the glass-forming ability and the thermal stability of $(Nd_{60}Fe_{30}Al_{10})_{100-x}Ni_x$ alloys has been investigated. The glass-forming ability of these alloys can be significantly enhanced with the addition of Ni. The proportion of amorphous phase in the as-cast alloys increases with the increase of Ni content. The melting temperature significantly decreases and the crystallization slightly increases with increase of Ni. Especially, T_{rx} is larger than 1 when the content of Ni is 8%. The melting temperature being larger than the crystallization temperature is due to the existence of more than two short range ordered structures including amorphous and/or nano-cluster phases with different thermal stabilities. The magnetic properties of the alloy are also sensitive to the addition of Ni. Without addition of Ni, more than one magnetic phase in the alloy results in the irregular shape in the hysteresis loop. With the addition of Ni, the content of the non-magnetic phases will increase, which will strengthen their effect as a pinning center to the magnetic phase and will increase the coercivity in the alloy.

Chapter 5 Effect of Cooling Rate on Microstructure and Magnetic Structure of Nd-Fe-Al Alloys

5.1 Introduction

Coercivity in metallic glasses has been shown to depend strongly on the cooling rate [122, 159,160], and a cooling related structure transition from the periphery to the center of the cross-section of the as-cast $Nd_{60}Fe_{30}Al_{10}$ alloys is reported in Chapter 4. Little direct evidence has been provided to show the magnetic structure in these alloys, which may result in diverse discussions on the origin of the high coercivity. By examining the changes of magnetic structures of the $Nd_{60}Fe_{30}Al_{10}$ alloy under different cooling rates, it is expected to gain a better understanding of the magnetic structures and properties of the alloys. In this chapter, the cooling rate involved variation in microstructure and magnetic structure will be investigated in detail in the as-cast $Nd_{60}Fe_{30}Al_{10}$ alloy. The magnetic domain structure will be investigated using a magnetic force microscopy, and the effect on the magnetic properties of the alloy will be discussed.

5.2 **Results and Discussions**

5.2.1 Microstructures

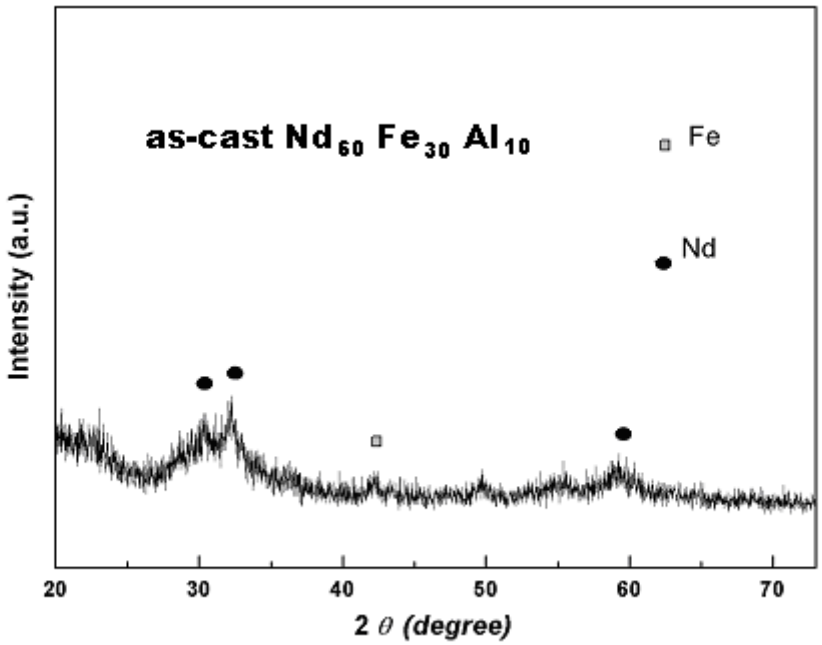

Figure 5-1XRD pattern of the as-cast $Nd_{60}Fe_{30}Al_{10}$ alloy

The structure of the as-cast $Nd_{60}Fe_{30}Al_{10}$ alloy was examined by XRD and is shown in Figure 5-1. Some weak diffraction peaks were detected over the broad amorphous diffraction hump, suggesting that a small amount of crystallite might precipitate in the amorphous matrix. These weak peaks correspond to the diffraction of the Nd and Fe crystalline phases.

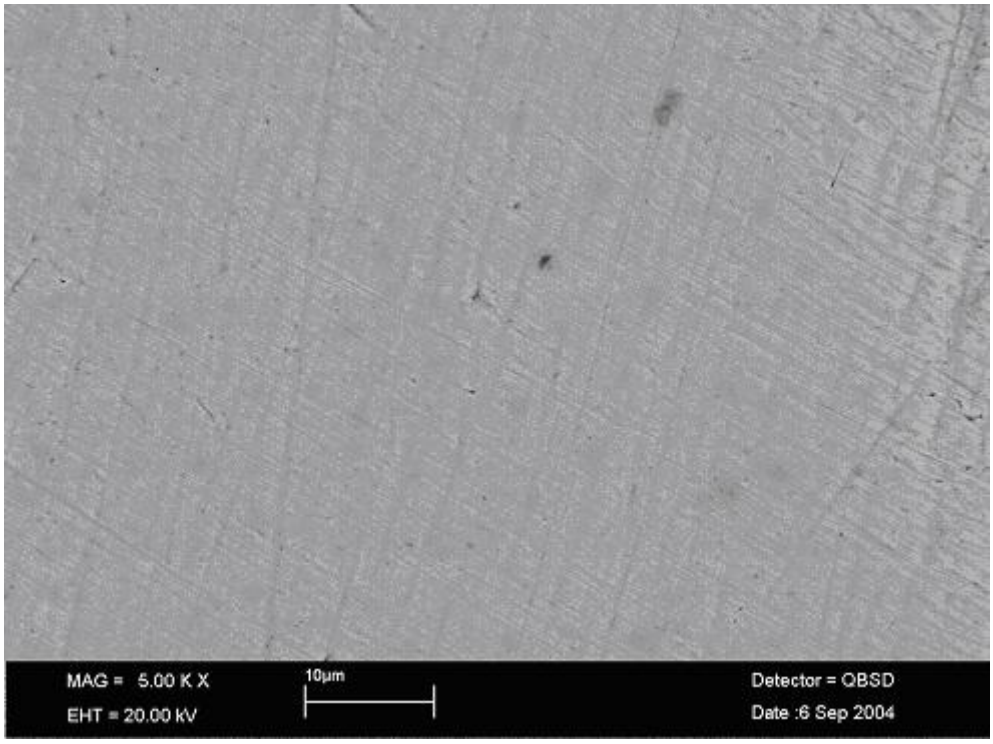
MAG = 5.00 K X
EHT = 20.00 kV
10µm
Detector = QBSD
Date :6 Sep 2004

(a)

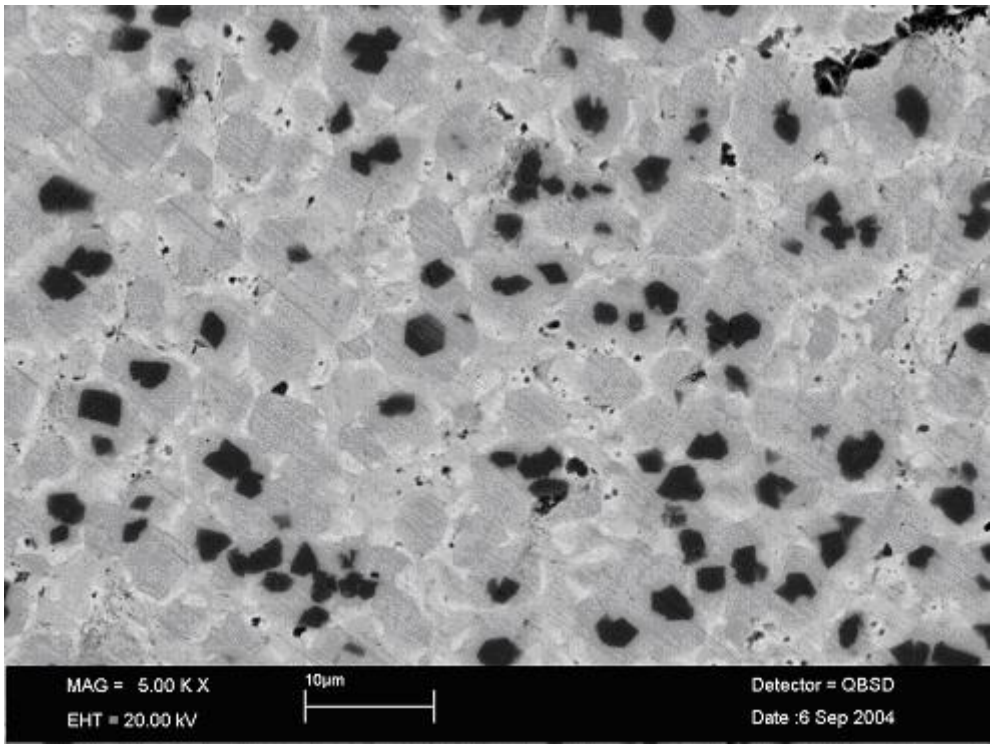
MAG = 5.00 K X
EHT = 20.00 kV
10µm
Detector = QBSD
Date :6 Sep 2004

(b)

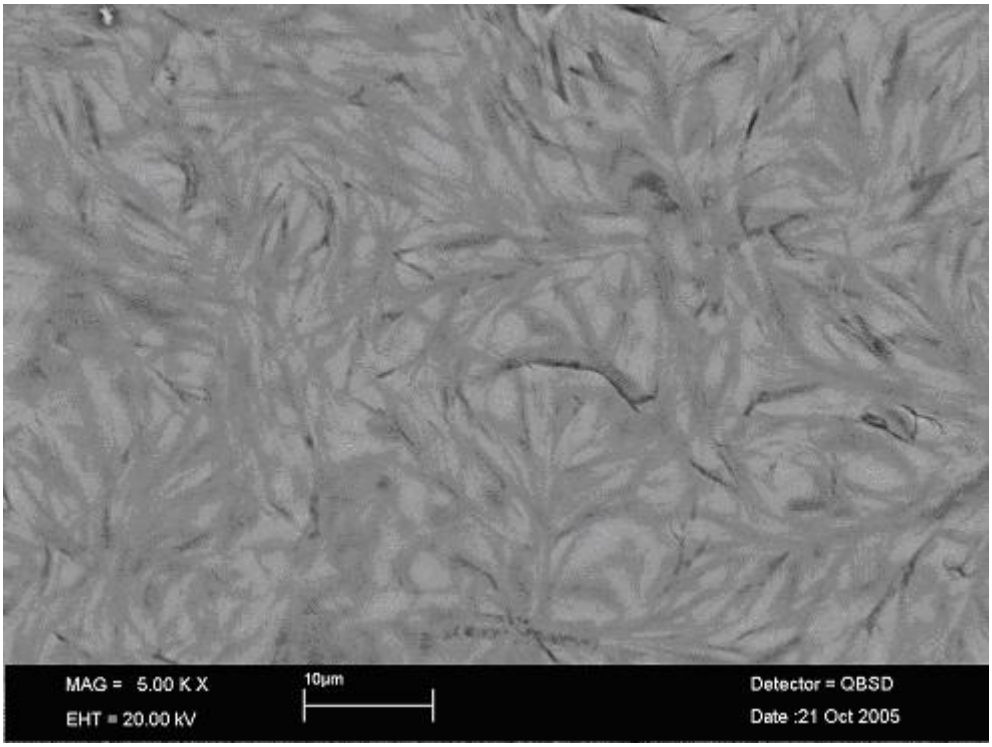

(c)

Figure 5-2 SEM morphologies of the as-cast and the master $Nd_{60}Fe_{30}Al_{10}$ alloy (a) at the periphery of the as-cast alloy; (b) at the center of the as-cast alloy; (c) the master alloy;

Figure 5-2 shows the SEM morphologies of $Nd_{60}Fe_{30}Al_{10}$ alloys, i.e., (a) at the edge of cross-section of the as-cast alloy, (b) at the center of cross-section of the as-cast alloy, and (c) the cross-section of the master alloy. The region at the edge of the cross-section of the as-cast alloy is found to be featureless (Figure 5-2(a)). However, the homogenous distribution of three different phases in white, gray and dark contrast respectively, was observed in the center of cross-section (Figure 5-2(b)). The region enclosed by the gray phase is about 5μm in size. The dark phase area always appears in the center of most gray phases. The changes of microstructure of the as-cast $Nd_{60}Fe_{30}Al_{10}$ alloy should be the result of different cooling rates from

the surface to the center of the cylinders. The cooling rate in the center of cylinder is not large enough to freeze the molten alloy into an amorphous structure in this region. Compared with the as-cast alloy, the master alloy is more homogeneous in morphology, and no apparent structure transitions were observed in the whole cross-section (Figure 5-2(c)). Gray strip-like structures, about 10μm in length, were observed in the cross-section. As is known, the master alloy is arc melted in the chamber of the equipment and cooled down to the room temperature naturally. The atoms in the alloy have enough time to move long distances which may explain the formation of a homogeneous structure in the master alloy.

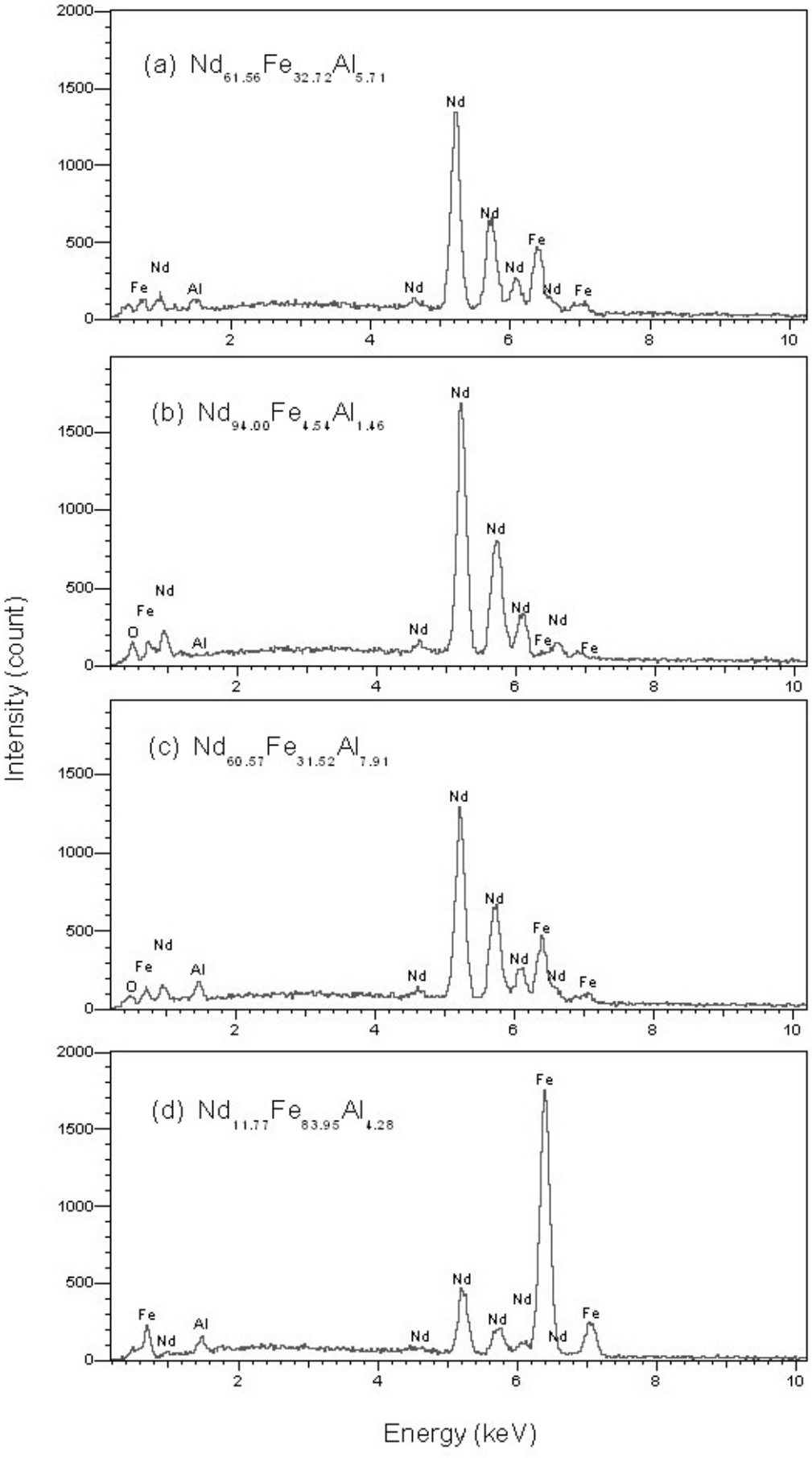
(a) $Nd_{61.56}Fe_{32.72}Al_{5.71}$
(b) $Nd_{94.00}Fe_{4.54}Al_{1.46}$
(c) $Nd_{60.57}Fe_{31.52}Al_{7.91}$
(d) $Nd_{11.77}Fe_{83.95}Al_{4.28}$
Intensity (count)
Energy (keV)

Figure 5-3 EDX profiles and corresponding compositions (a) at the edge, and (b) white phase region, (b) gray phase region and (c) dark phase region at the middle of the cross-sectionof the as-cast $Nd_{60}Fe_{30}Al_{10}$ alloy

In order to identify the composition in different regions, Figure 5-3 shows the EDX profiles and the corresponding compositions of the edge region (Figure5-3 (a)), the white phase area (Figure5-3 (b)), the gray phase region (Figure5-3(c)) and the dark phase region (Figure5-3 (d)) of the centre region of the cross section of the alloy. A significant difference in chemical composition is observed. The network-like white phase is identified as a Nd-rich phase with a composition of $Nd_{94.00}Fe_{4.54}Al_{1.46}$. The dark phase surrounded by the gray phase is identified as a Fe-rich phase with a composition of $Nd_{11.77}Fe_{83.95}Al_{4.28}$. However, there is no significant difference in the composition of the amorphous phases at the edge and the center of the cross-section. Based on the EDX and XRD results, it is considered that the precipitated Nd and Fe crystallites exist mostly in white and dark phases, whereas the gray phases at the periphery and the center of the cross section are mostly observed in the amorphous structure. The chemical compositions of the master alloy in both stripe-like and gray matrix regions were also examined for comparison purposes. The composition of the stripe-like region and the gray matrix was identified as $Nd_{58.00}Fe_{39.24}Al_{2.76}$ and $Nd_{61.46}Fe_{35.62}Al_{2.92}$, respectively. It suggested the structure of the master alloy is more homogeneous than that of the as-cast alloy.

5.2.2 Magnetic Properties

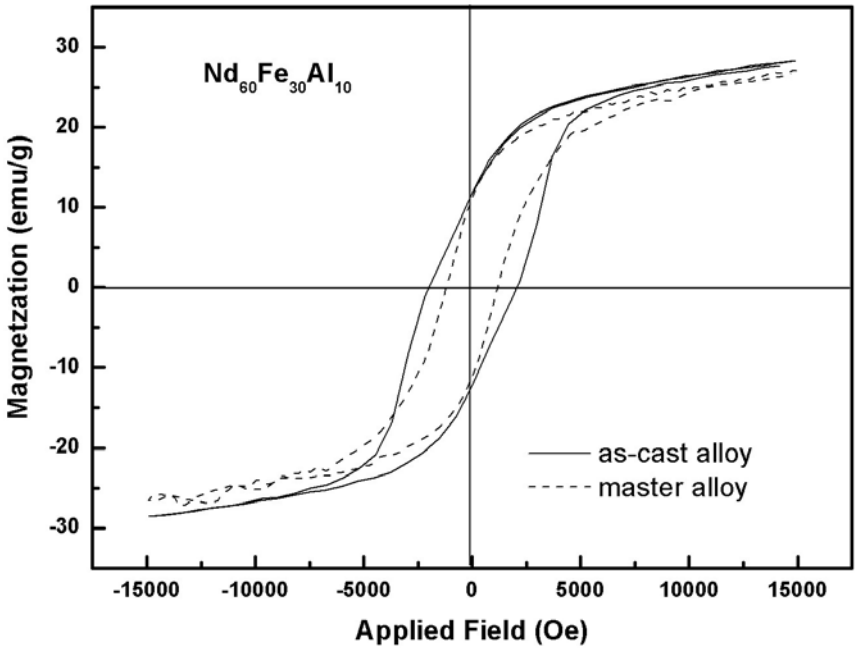

Figure 5-4M-H hysteresis loop of the as-cast and master $Nd_{60}Fe_{30}Al_{10}$ alloys at room temperature

Figure 5-4 shows the M-H hysteresis loop of the as-cast alloy measured under an applied field of 15,000Oe. The M-H loop of the master alloy is also shown in the figure. Both alloys exhibit a hard magnetic behavior. The coericivity H_c is about 1,158Oe for the master alloy and 2,142Oe for the as-cast sample. It is interesting to note that, differing from the smooth hysteresis curve of the master alloy, a minor step in the demagnetization quadrant of the M-H hysteresis loop was observed in the as-cast sample.

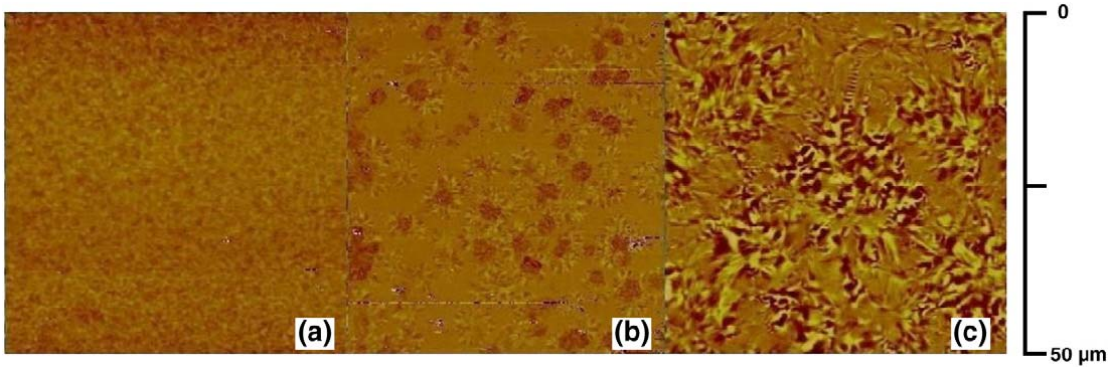

Figure 5-5 Magnetic force morphology of the as-cast and the master $Nd_{60}Fe_{30}Al_{10}$ alloy (a) at the periphery of the as-cast alloy; (b) at the center of the as-cast alloy; (c) the master alloy;

MFM was introduced to examine the magnetic domain structure in the different regions observed in the alloys. The results are shown in Figure 5-5. The dark and bright contrast corresponds to the up and down directions towards the magnetized direction of the magnetic tip, respectively. In the as-cast samples, two kinds of magnetic domains, different in shape, were observed at the periphery and the center of the cross section (Figure 5-5(a) and (b)). At the periphery (Figure 5-5 (a)), fine strip-like domains, characterized by dark regions adjacent to bright regions on a sub-micron scale, are distributed homogeneously in an area of 50x50μm^2. A similar structure was also observed in the as-cast Nd-Fe-Al-Co alloy by Wei [9].

In the center (Figure 5-5 (b)), sunflower-like domains were observed, and dark areas of about 3μm are surrounded by strip-like domains with dark and bright contrast. Most of the sunflower-like domains are isolated from each other by a nonmagnetic region. Though in the MFM image of the master alloy sample (Figure 5-5 (c)), strip-like magnetic domains were also observed and separated by

nonmagnetic boundary, the strip-like domains in the master alloy are more irregular and coarser, with a length about 5μm and a width about 1.5μm.

5.2.3 Discussion

The relationship between the cooling rate, microstructure and magnetic structure has been intensively studied in melt-spinning ribbons of different thicknesses and/or mould-casting cylinders of different diameters [160, 167, 168]. In this investigation, continuous variation in the microstructure was observed in one as-cast alloy, which is closely related to the changes of cooling rates from the surface to the center of the cylinders. Due to the high heat transportation from the melted alloy to the copper mold, the precipitation of the crystalline structure is bypassed and the periphery of the melt alloy is frozen into an amorphous structure. However, the cooling rate in the center of the cylinder is not sufficient to suppress the occurrence of nucleation and the growth of the Nd and Fe crystallites. Comparing the SEM and MFM results of the as-cast alloy, it is found that the amorphous phases, the Fe-rich phases and the Nd-rich phases corresponded to the fine strip-like domains, the dark region of the sunflower-like domains and the white boundary of the sunflower-like domains. The Fe-rich phase seems more easily to be magnetized by the MFM magnetic tip and exhibits a relative softer magnetic property. No apparent response to the magnetic tip of the MFM in the net –like Nd-rich phase implies that the region is mostly paramagnetic. It is interesting to note the strip-like domains are observed both in the

amorphous regions at the periphery and the center of the rod.

In previous reports, a high coericivity is not only available in melt-spinning Nd-Fe binary and Nd-Fe-Al ternary ribbons prepared with a relative slow spinning rate but also in as-cast bulky alloys [159,160]. The cooling rate related variation in coercivity may be understood from the viewpoint of the existence of ordered clusters with a strongly exchange coupling model [65, 138, 161]. According to the model, differing from the melting-spinning ribbons prepared from an ultra high spinning rate, ordered clusters of several nanometers size may be precipitated in the amorphous matrix of as-cast bulky alloys. When the magnetic coherence, which is equivalent to the dimensions of the ordered clusters, is larger than the exchange length, a large coercivity may appear in the alloys. In this study, a small step is observed in the M-H curves, implying the existence of two magnetic structures with different coercivities in the as-cast alloy. Due to the high cooling rate at the periphery, the amorphous phase, containing ordered clusters, may exhibit a large coercivity. However, due to the low cooling rate in the center of the alloy, crystallites of micrometer in dimension instead of nanosized clusters are precipitated, which results in the formation of a magnetic structure with relative small coercivity.

5.3 **Conclusions**

The cooling rate induced evolution in microstructure from amorphous to partial crystalline precipitation was observed in one as-cast $Nd_{60}Fe_{30}Al_{10}$ sample. A featureless amorphous phase was observed at the periphery, and a network-like

structure consisting of the Fe-rich, Nd-rich and amorphous regions was formed in the center of the sample. As a consequence of different microstructures, two magnetic structures, fine strip-like domains characterized by dark regions adjacent to bright regions at the sub-micron scale and sunflower-like domains at the micron scale, were observed at the periphery and the center of the cross section, respectively. The presence of a small step in the hysteresis curve of the as-cast alloy further reveals that the two magnetic domains have different coercivities.

Chapter 6 Temperature Dependence of Dual Magnetic Phase Behavior of Nd based Bulk Metallic Glass

6.1 Introduction

In chapter 4, it was seen that the alloy with the addition of about 8% Ni exhibits the largest glass forming ability. The structural examination using XRD shows that two amorphous phases or short range ordered structures may exist in the alloy. However, only one magnetic phase was detected by VSM at room temperature, which is different from the alloy without Ni addition which showed two apparent magnetic structures in different regions of the cross-section. It is well known that the magnetic phase may exhibit different responses to the temperature due to the competition between the magnetic energy and thermal energy in the magnetic system. It is most worthwhile to investigate the magnetic properties below room temperature. It is of significance to the understanding of the origin of hard magnetism and to tailor the magnetic properties of the Nd-based bulk metallic glass forming alloys.

In order to investigate the temperature dependence of the magnetic properties of the Nd-based alloys, the magnetic properties of the alloy will be measured at low temperatures using low temperature VSM with the temperature ranging from room temperature down to 60K. The microstructure of the as-cast $Nd_{55}Fe_{28}Al_9Ni_8$ alloy will further be examined using high resolution transition electronic microscopy (HRTEM).

6.2 **Results and Discussion**

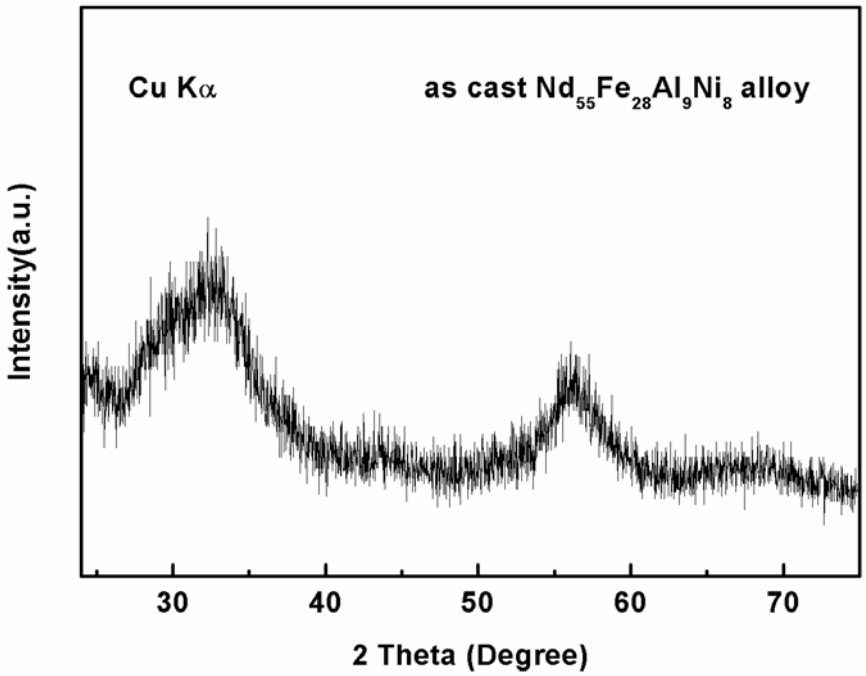

Figure 6-1XRD pattern of the as-cast $Nd_{55}Fe_{28}Al_9Ni_8$ alloy

The structure of the as-cast $Nd_{55}Fe_{28}Al_9Ni_8$ alloy has been examined by XRD and is shown in Figure 6-1. The results indicate that the alloy is almost full in the amorphous structure, characterized by two broad humps around $2\theta \approx 32^o$ and $2\theta \approx 55^o$. No apparent diffraction peaks are detected over the two amorphous diffraction humps. Moreover, the amorphous hump at higher diffraction angles is sharper than the one at lower diffraction angles, suggesting that the alloy involves at least two short-range ordered structures within the detectability of XRD. The formation of two short-range ordered structures probably originated due to the occurrence of phase separation during the solidification of the molten alloy. The separation of the

amorphous phase in both Nd-based bulk metallic glasses and ribbons was also reported previously by Sun et al. [98, 162].

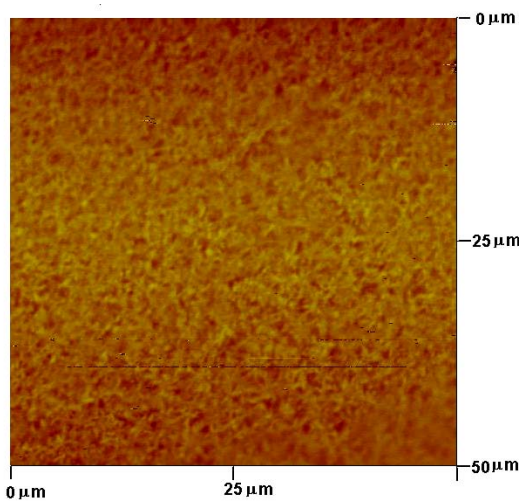

Figure 6-2 MFM image of the as-cast $Nd_{55}Fe_{28}Al_9Ni_8$ alloy at room temperature

MFM is applied to clarify the magnetic morphology of the as-cast $Nd_{55}Fe_{28}Al_9Ni_8$ alloy, and the magnetic domain structure of the alloy is shown in Figure 6-2. The dark and bright contrast corresponds to the up and down directions towards the magnetized direction of the magnetic tip, respectively. It is observed that fine strip-like domains, which are characterized by dark regions adjacent to bright regions of sub-micron scales, distribute homogeneously in an area of $50x50\mu m^2$. The result implies that the single homogenous domain structure is attributed to one magnetic structure.

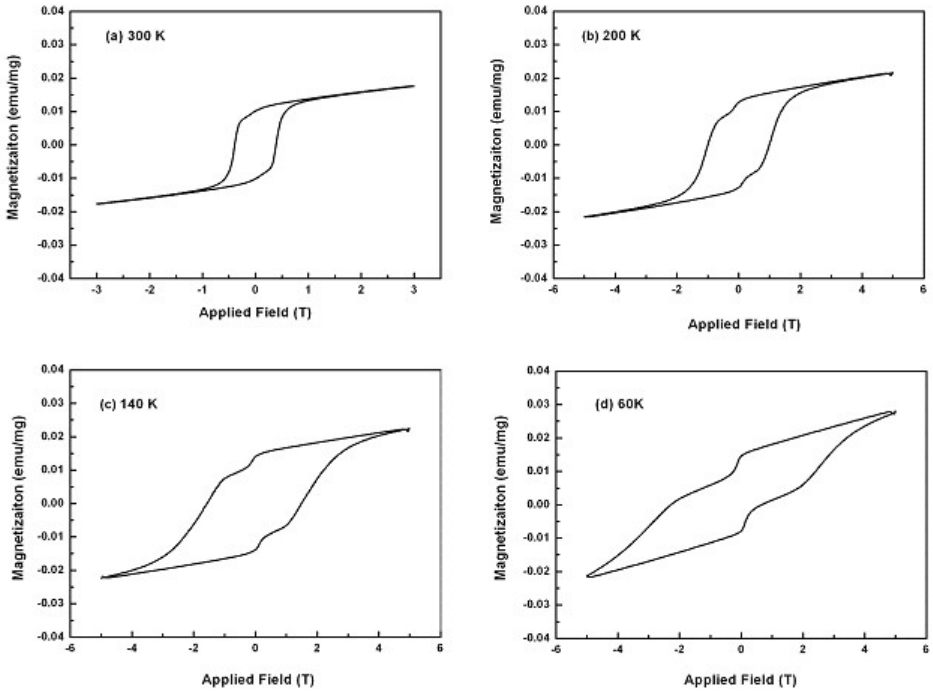

Figure 6-3 Hysteresis curves of the $Nd_{55}Fe_{28}Al_9Ni_8$ alloy at various temperatures

To further reveal the magnetic behavior of the as-cast $Nd_{55}Fe_{28}Al_9Ni_8$ alloy, the hysteresis curves were measured at different temperatures in a range from 60K to 300K and the results are plotted in Figure 6-3. The magnetic parameters such as coercivity and remanent magnetization in the second quadrant are considered and listed in Table 6-1. It is found that the hysteresis at room temperature has the typical shape of a hard magnet with a coercivity of 0.40T, which is slightly larger than that of $Nd_{60}Fe_{30}Al_{10}$ and $Nd_{60}Fe_{20}Al_{10}Co_{10}$ alloys [5, 9]. With the decrease of temperature, a turning point was observed in the curve, implying the appearance of two magnetic phases with different magnetic behavior in the alloy.

Table 6-1Remanence and coercivity of the $Nd_{55}Fe_{28}Al_9Ni_8$ alloy at different temperature.

Temperature (K)	M_r (emu/g)	H_c (T)
300	10.185	0.396
200	12.751	1.003
140	14.053	1.581
80	15.392	2.400
60	14.611	2.287

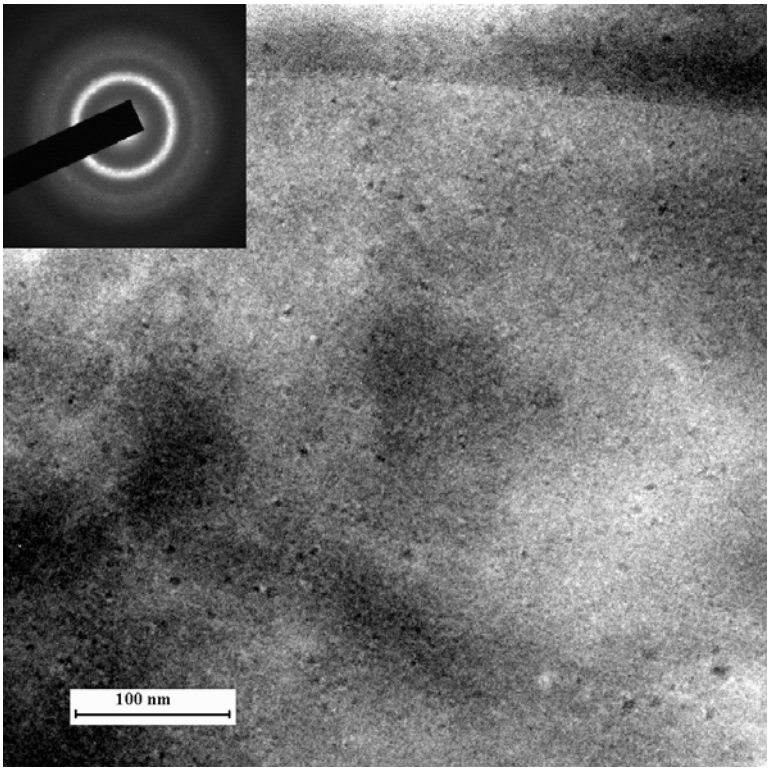

Figure 6-4TEM dark field image of the $Nd_{55}Fe_{28}Al_9Ni_8$ alloy; inset shows the SAED image

A TEM bright field image of the $Nd_{55}Fe_{28}Al_9Ni_8$ alloy (Figure 6-4) shows the presence of numerous nanosized clusters dispersed homogeneously in the amorphous matrix, which is not resolved by XRD (Figure 6-1). The diffraction

pattern of the corresponding region (inset of Figure 6-4) shows a typical amorphous bright halo. Moreover, a broader dim ring was observed outside the bright one, also implying the alloy may consist of more than one kind of short-range ordered structure, i.e. one amorphous matrix and fine clusters, of size several nanometers, in the alloy.

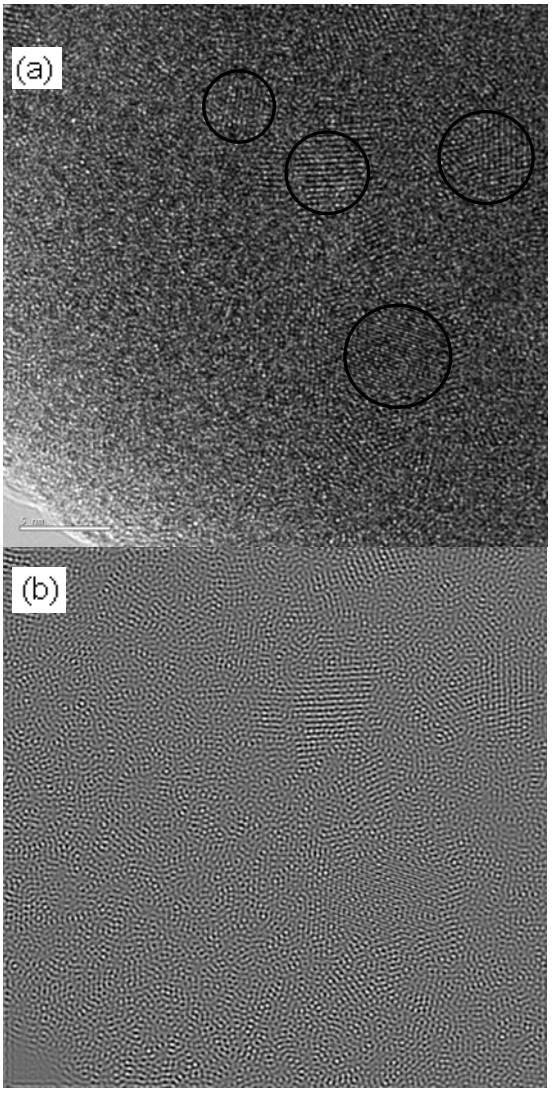

Figure 6-5 (a)HRTEM image of the $Nd_{55}Fe_{28}Al_9Ni_8$ alloy, the circled regions are nanoclusters of size about 5nm; (b) FTT TEM image of the $Nd_{55}Fe_{28}Al_9Ni_8$ alloy in the same region

In order to clarify the microstructure of the cluster-embedded amorphous matrix in the alloy, HRTEM examination was also carried out to show the microstructure characteristics from the atomic scale. Figure 6-5(a) shows the image of the $Nd_{55}Fe_{28}Al_9Ni_8$ sample. The corresponding FTT image is also presented (Figure6-5(b)). It is noted that nanoclusters are not uniform in size and are mainly classified by size, i.e. clusters about 5nm in size and clusters close to 1.5nm in size. For a cluster of about 5nm, the distances between two adjacent fringes in the clusters are not uniform either, which may result from the different crystallographic planes of each cluster. In some 5nm clusters, with perpendicular crystallographic planes, the evaluated ratio of the distance between the normal planes is about 1:3, which implies the cluster may be in the HCP structure. The analysis of the chemical composition shows that the content of Nd atoms in each cluster is mostly more than 60%, which is larger than its mass content (55%) in the alloy. Together with the result of the crystallographic planes calculation, it can be said that the clusters should be Nd riched HCP structures. However, the content of the large clusters (about 5nm) is much smaller that that of amorphous matrix and small clusters (smaller than 5nm). Moreover, due to their relatively low density, the distance between each 5nm clusters is mostly greater than 5nm. For clusters of about 1.5nm, it is hard to identify their chemical composition and structure because they are completely mixed with the amorphous structure and have small dimensions, even though they have high density compared with 5nm clusters.

The existence of numerous nanoclusters in the amorphous matrix in the alloy

may contribute to the high coercivity of the two magnetic phases. The formation of hard magnetic properties can be understood in terms of the magnetic exchange coupling with large random anisotropy [162]. According to the theory, clusters of size several nanometers may be aligned by a strong exchange coupling. If the magnetic coherence length *l*, which can be evaluated from the dimensions of the magnetic clusters, is comparable or larger than the exchange coupling correlation length $L_{ex} = (A/K)^{1/2}$ (*A* is the exchange stiffness and *K* is the crystal anisotropy constant), the direction of the local magnetic moment will be mainly aligned to the anisotropy orientation, which will result in a high coercivity. Following the calculation by Xing [163], the local exchange-coupling correlation length can be evaluated from the *A* and *K* of $Nd_2Fe_{14}B$, where *A* is 7.7×10^{-12}J/m and *K* is 4.3×10^{6}J/m^3. Thus the evaluated L_{ex} is about 1.3nm. Taking L_{ex} as a critical length, the clusters smaller than 1.3nm, including the amorphous matrix, may exhibit paramagnetic properties, and the clusters larger than 1.3nm are expected to exhibit hard coercivity. However, it should be mentioned that the distance between each magnetic cluster will also affect the exchange interaction [163]. In order to obtain a strong exchange coupling, the distance between the clusters should be small. As observed by HRTEM, clusters can be divided into two types, of about 1.5nm and 5nm in size, respectively. Because of their low density, the distance between each cluster of about 5nm is relative large, which might weaken the magnetic interaction. For the case of 1.5nm clusters, because of their high density in the alloy, the distance between two neighbor clusters is much smaller. As a result of the short distance, the

exchange interaction is strengthened. However, further investigation should be done to clarify the specific value of the critical distance in the system.

6.3 **Conclusions**

The as-cast $Nd_{55}Fe_{28}Al_9Ni_8$ alloy is found to consist of nanoclusters, no larger than 5nm, embedded in an amorphous matrix. The clusters can be further classified by size, i.e., clusters about 5nm in size and 1.5nm in size. The clusters with sizes larger than 1.3nm will exhibit hard magnetic properties. With the decrease of temperature, the hysteresis of the as-cast $Nd_{55}Fe_{28}Al_9Ni_8$ exhibits a complex shape, and a step was observed in the hysteresis curves when the temperature was below 140K. Two types of magnetic phase behavior at low temperature are associated to the different distances between these two kinds of magnetic clusters.

Chapter 7 Investigation of Dual Magnetic Phase Behavior in Bulk Metallic Glasses by Monte Carlo Simulation

7.1 Introduction

In Chapter 6, the precipitation of nanoclusters in the amorphous matrix has been observed in an as-cast $Nd_{55}Fe_{28}Al_9Ni_8$ bulk metallic glass alloy. A step was only observed in the hysteresis loop when the alloy was examined by VSM at low temperature. Two kinds of magnetic clusters with different magnetic properties were proposed to contribute to the presence of the step. One magnetically hard phase was observed in the alloy at room temperature and another hard magnetic phase was identified by decreasing the temperature below room temperature.

In this investigation, the Monte Carlo simulation method is applied to study two types of magnetic phase behavior in the alloy. In this method, a magnetic cluster will be used as a basic magnetic unit. The findings should lead to a better understanding of the behaviour of magnetic BMGs.

7.2 Monte Carlo Simulation

In order to model the magnetic ordering in ferromagnetic materials, two main factors determining the magnetism have to be considered: the exchange interaction and the magnetic anisotropy. The external field also needs to be taken into account if

it is applied to the ferromagnetic materials.

The ferromagnetic exchange interaction contributes to the parallel orientation of neighboring magnetic moments and it can be expressed in Hamiltonian form as [78, 79]:

$$E_{exchange} = -\frac{1}{2}\sum_{i \neq j} J_{ij}\vec{m}_i \cdot \vec{m}_j \ , \qquad (7\text{-}1)$$

where $\vec{m}_i$ is the magnetic moment of the i cluster, J_{ij} is the interaction between the i cluster and its neighboring cluster.

On the other hand, although the magnetic anisotropy arising from long-range crystallinity has been investigated extensively, a theory for amorphous materials is still lacking due to the absence of a long-range ordered atom configuration in amorphous materials. In fact, in amorphous materials, the electrostatic field contributing to magnetic anisotropy still forms because of the existence of charges of neighboring atoms or ions, as well as conduction electrons. According to the assumption of Harris et al, randomness of the anisotropy field is the most important characteristic of the amorphous state, which results from the topological disorder of a random close-packing structure in amorphous alloys. With this assumption, Harris, Plischke and Zuckermann proposed a model of random magnetic anisotropy [83], and the electrostatic field interaction is represented in Hamiltonian form,

$$E_{anisotropy} = -K\sum_{i}[\vec{n}_i \cdot \vec{m}_i]^2 \qquad (7\text{-}2)$$

where, $\vec{n}_i$ is a unit vector in the direction of the easy magnetization of the cluster, K is the magnetic anisotropy constant.

On the other hand, the effect of the external field on the magnetic moment can

be expressed in Hamiltonian form as:

$$E_{field} = -\vec{H}\sum_i \vec{m}_i \tag{7-3}$$

where, $\vec{H}$ is the applied magnetic field.

In the simulation, a magnetic BMG is assumed to be a magnetic cluster system consisting of N*N clusters. The system is set as a two dimensional space, and each cluster has four nearest neighbors, during the calculation of the interaction. Each cluster possesses a magnetic moment *m* and uniaxial magnetic anisotropy energy of *Ed*. The anisotropy of each cluster was set as constant and in a given direction, for simplicity. Combining eq. 7-1 to 7-3, then the Hamiltonian energy E of the cluster system is given as

$$E = -K\sum_i [\vec{n}_i \cdot \vec{m}_i]^2 - \frac{1}{2}\sum_{i\neq j} J_{ij}\vec{m}_i \cdot \vec{m}_j - \vec{H}\sum_i \vec{m}_i \,, \tag{7-4}$$

In present study, the simulation will be performed using the standard Metropolis algorithm, which is a kind of importance sampling which is different from the randomized individual sampling.

For a magnetic particle system with 4-degrees of freedom containing N*N particles, the average of A at given temperature T is given by:

$$< A >= \frac{1}{Z}\sum_x A(x)e^{-\frac{E(x)}{T}} \tag{7-5}$$

where $x = 4^{N*N}$ is the total number of system states corresponding to 4 states of N*N clusters; $Z = \sum_x A(x)e^{-\frac{E(x)}{T}}$ is the partition function. It is impossible to take into account all the different states of the system in the calculation of the variable A, because $x = 4^{N*N}$ will increase to an exceedingly large value beyond the calculation

capability of the present-day computer.

So, importance sampling is introduced into the calculation, i.e.,

$$< A >_{est} = \frac{\sum_{l=1}^{M} \frac{A(x_l) e^{-\frac{E(x_l)}{T}}}{P_{samp}(x_l)}}{\sum_{l=1}^{M} \frac{e^{-\frac{E(x_l)}{T}}}{P_{samp}(x_l)}} \tag{7-6}$$

And further introduce a conformation with a probability of $P_{samp}(x_l) \propto e^{-\frac{-E(x_l)}{T}}$, then the estimate for the average of a variable A becomes:

$$< A >_{est} = \frac{\sum_{l=1}^{M} A(x_l)}{M} \tag{7-7}$$

The Metropolis algorithm is realized by the construction of a so-called Markov line, i.e., the each energy state of the system is derived from the last state, under a certain probability. If the sample size is large enough, the system will tend to its lowest energy state, i.e., equilibrium state, at this probability. For a magnetic system, a high enough temperature is given to the magnetic system to make sure the system is in a molten state. Then a rapid cooling is applied to the system to freeze the movement of the particles in the system. If the cooling time is long enough, the system will still be in its equilibrium state.

The algorithm for the simulation is summarized as follows:

1) Choose an i cluster randomly in the system, and a minor vibration is given to this cluster in the magnetization direction;
2) calculate the energy difference $\delta E = E' - E$, where E' is the energy after vibration and E is the energy before vibration;
3) if $\delta E \le 0$, update the energy state of the cluster to the new one;

4) if $\delta E > 0$, the cluster is allowed to change to its new energy state with a probability of $e^{-\frac{\delta E}{kT}}$, otherwise, it remains at its current state;
5) go to 1) and continue the next calculation.

In the simulation, each Monte Carlo simulation step consists of N*N times calculation for the energy difference between a randomized chosen cluster and its neighbors. For the investigation of the relationship between magnetization and temperature, the Monte-Carlo steps S should be larger than 6000 for a system size N<20, to reach its equilibrium state. The first 6000 steps will allow the system to be thermalized and all the data generated in these steps will be discarded. For the remaining steps (S-6000), only the data for each 100th step will be collected. For the investigation of the magnetization and applied field, i.e., M-H hysteresis loop, the magnetic system will be in a non-equilibrium state, so less Monte-Carlo steps will be needed. The simulation also assumes that the interaction only occurs between the cluster and its four nearest neighbors for simplicity.

The definitions of the parameters in this chapter are summarized as follows:

1) N*N is the number of the clusters in the system
2) E is the energy,
3) H is applied magnetic field;
4) $\vec{m}$ is the magnetic moment of the cluster;
5) $\vec{n}$ is a unit vector in the direction of the easy magnetization of the cluster,
6) J is the interaction between the cluster and its neighbor cluster;

7) K is the magnetic anisotropy constant;

8) T is the temperature.

This algorithm is realized using visual C++ language. The interface windows for the setting-up of the parameters and the main source code are given in Appendix I and II, respectively, for reference.

7.3 **Results and Discussion**

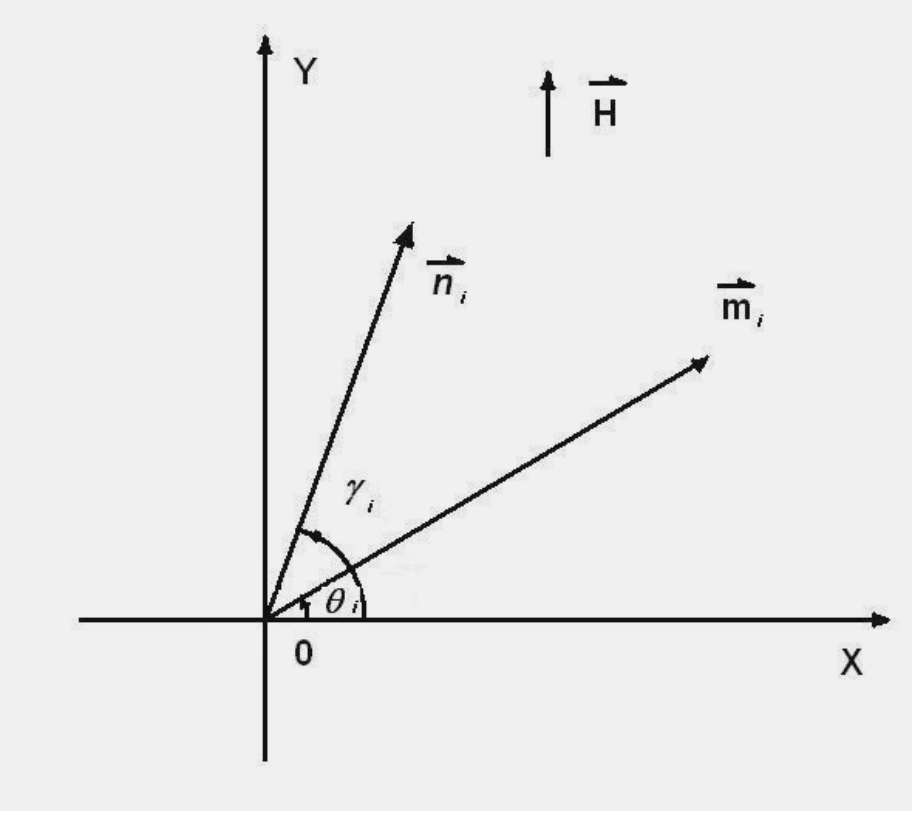

Figure 7-1 The coordination system

The coordinate system used in present investigation and the definition of a given cluster are shown in Figure 7-1. The applied field $\vec{H}$ is set always along the y axis. The angles of the magnetization direction and the easy direction of the i^{th} cluster is

θ and γ respectively.

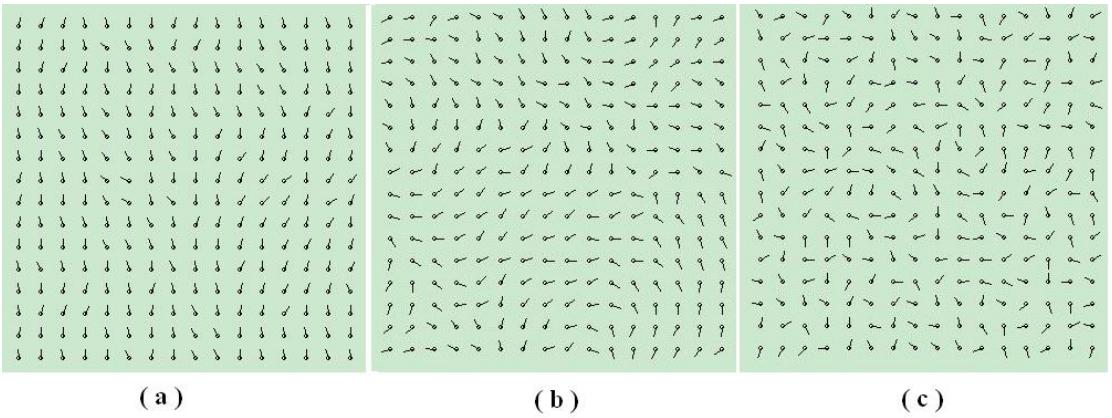

Figure 7-2Typical spin configurations of the system with N*N=16*16, m=1, J=0.5, K=0, H=0 at different temperatures, i.e., T=0.001K, 100K and 900K, respectively.

Figure 7-2 shows the state configuration of a system with N*N=16*16, m=1, J=0.5, K=0, H=0 and temperatures of T=0.001K, 100K and 900K, respectively. Each cluster is represented by a dark dot with a short line. The short line shows the direction of each cluster. From these three configurations, it can be seen, at T=0.001K, the configuration directions are almost parallel. When the temperature increases to T=100K, the direction of each cluster does not necessarily align in one direction. For T=900K, the direction of each cluster seems to be more diverse, and the system is almost in a disordered state. Based on these findings, the system has transformed from a disordered to an ordered state with a decrease in temperature.

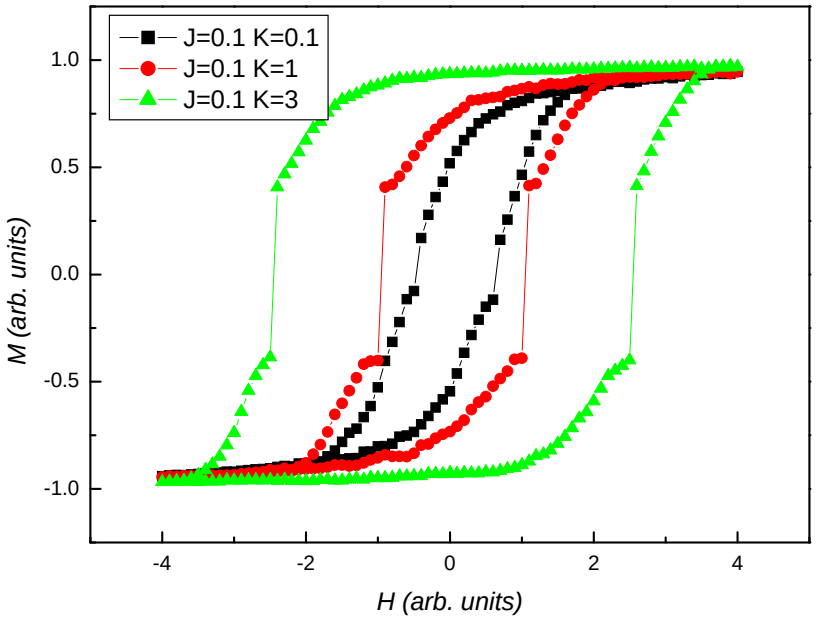

Figure 7-3Simulated M-H curves of one cluster system with different anisotropy

Figure 7-3 shows the simulated hysteresis loops of the systems with different anisotropy constants K, i.e., K=0.1, 1 and 3, respectively, at a temperature of T=300K. It can be seen that these systems with different cluster anisotropies have different responses to the applied field. With increase of K, the coercivity of the system also increases. For the cluster with K=0.1, the coercivity decreases simultaneously with a decrease in the applied field, implying that the magnetization of system has a low resistance against a change in the applied field. However, for the cluster with K=3, the hysteresis exhibits a typical square shape, illustrating its strong resistance against the applied field.

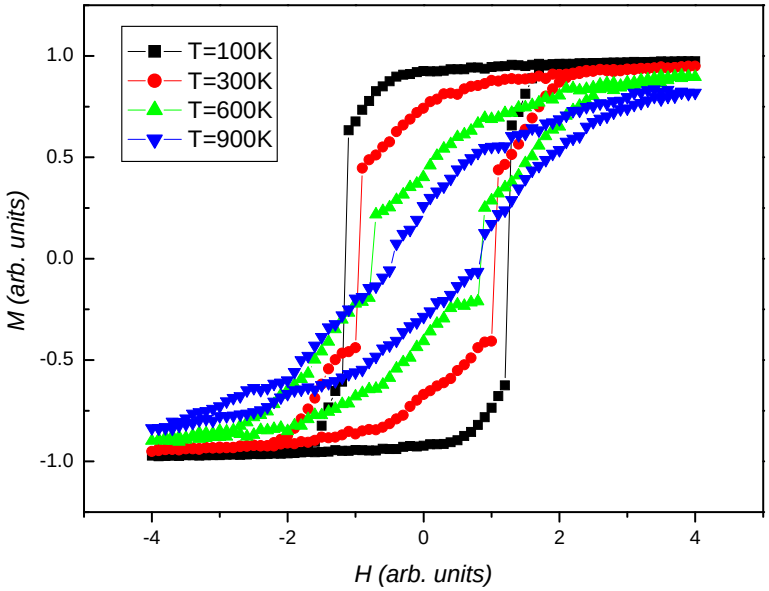

Figure 7-4Simulated M-H curves of one cluster system at temperatures of T=100K, 300K, 600K and 900K

In order to investigate the effect of changing the temperature in the system, the hysteresis loops of the cluster system at different temperatures were also simulated, and are given in Figure 7-4. At low temperatures, such at T=100K, the loop is perfectly square. With an increase of temperature to a medium value, such as T=300K, the loop still has a square shape. However, with a further increase in temperature to T=600K, the hysteresis loop exhibits an apparent drop in the value of remanence. If the temperature is further increased to say T=900K, the remanence of the system decreases dramatically. The decrease in remanence with the decrease of temperature is due to the strengthening of the thermal energy of the system over the exchange interaction energy in the system.

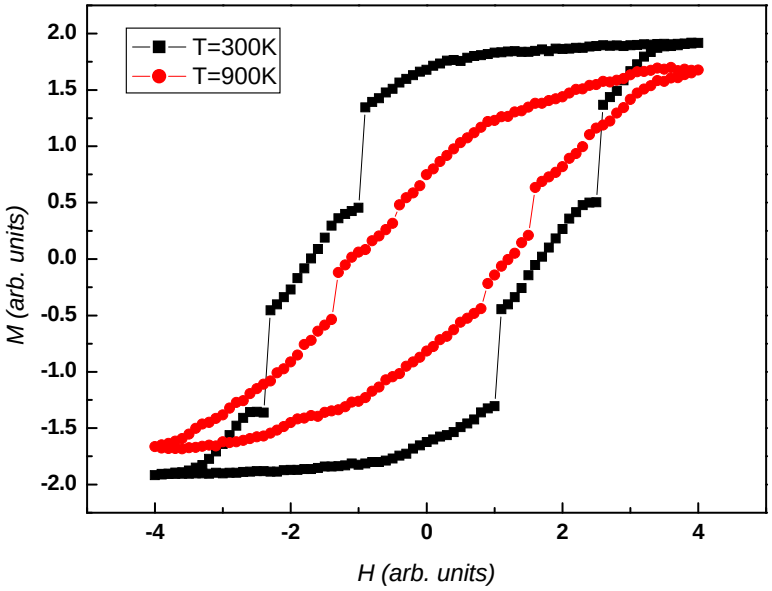

Figure 7-5 Overlapping M-H curve of two systems at different temperatures, i.e., T=300K and T=900K.

Considering the effect of both the cluster properties and temperature on the magnetic properties, Figure 7-5 shows the overlapping hysteresis loop of the two kinds of clusters, i.e., K=1 and 3 respectively, at temperatures T=300K and 900K. For the loop of the two clusters at a higher temperature such as T=900K, the magnetization of the system decreases more dramatically because the thermal energy of the system is larger than the exchange interaction energy between the clusters. At T=300K, the hysteresis loop shows a more complex shape. A step is observed when the applied field is decreased from H to –H, implying both clusters have responded to the applied field. Combining the effects of changing anisotropy and changing temperature on the coercivity, it is shown that the cluster with K=3 exhibits a strong

response to the applied field and a stronger resistance to the change of temperature. However, for the cluster with K=1, it only has an apparent response to the applied field when the temperature is at T=300K. The observed step during the demagnetization process contributes to the strengthened magnetization of the cluster with K=1 and T=300K.

For the magnetic behavior of the as-cast $Nd_{55}Fe_{28}Al_9Ni_8$ alloy, the hysteresis curves have been investigated at different temperatures in a range from 60K to 300K, as reported in Chapter 6. The hysteresis loops measured at T=300K and T=140K are given in Figure6-3. At 300K, the hysteresis loop has a shape typical of a hard magnetic phase. However, by decreasing the temperature down to 140K, a step was observed in the hysteresis curves during the process of demagnetization. This suggests that two different hard magnetic phases exist in the as-cast sample, which can be distinguished at a low temperature. Kong et al have also observed the step in the hysteresis loop of the $Nd_{55}Fe_{30}Al_{10}B_5$ BMG [10]. It was reported that the step was caused by the presence of the second hard magnetic phase, and the loop with step can be resolved into a hard magnetic phase and a stronger hard magnetic phase.

Compared with the experimental results, it can be seen that a cluster system containing two kinds of magnetic clusters of different anisotropy, i.e., different magnetic properties, exhibits similar behavior to the $Nd_{55}Fe_{28}Al_9Ni_8$ bulk metallic glasses, with a microstructure of nanocluster precipitation in an amorphous matrix at different temperatures.

7.4 **Conclusions**

Based on the Monte Carlo simulation, hysteresis loops of various cluster systems have been investigated. It has been found that the coercivity of the cluster is closely related to the change of temperature and anisotropy of the system. By overlapping the hysteresis loops of the two cluster systems, with different anisotropy at different temperatures, a step is only observed when the system is at a low temperature. The result of the temperature related occurrence of the step in the hysteresis loop is consistent with that observed in experimental examinations of bulk metallic glass based alloys.

Chapter 8 Overall Conclusions

In this project, the dependence of magnetic properties on the different microstructure in magnetically hard bulk metallic glass has been investigated. Based on the findings, the following conclusions can be drawn.

(1) The effect of Ni addition on the glass-forming ability and thermal stability of $(Nd_{60}Fe_{30}Al_{10})_{100-x}Ni_x$ alloys has been investigated. The glass-forming ability of these alloys can be significantly enhanced with the addition of Ni. The proportion of the amorphous phase in the as-cast alloys increases with the increase of Ni content. The melting temperature significantly deceases and the crystallization slightly increases with the increase of Ni. Specially, T_{rx} is greater than 1 when the content of Ni is 8%. The melting temperature is higher than the crystallization temperature, and is due to the existence of more than two kinds of short range ordered phases, including amorphous and/or nanocluster phases with different thermal stabilities. Further microstructure examination shows that the alloy with 8% Ni contains nanoclusters of size no larger than 5nm, dispersed in the amorphous matrix. The magnetic properties of the alloy are also sensitive to the addition of Ni. Without the addition of Ni, more than one magnetic phase in the alloy results in the irregular shape of the hysteresis loop. With the addition of Ni, the content of the non-magnetic phases will increase, which will strengthen their effect as pinning centers for the magnetic phase and will increase the coercivity in the alloy.

(2) The cooling rate induced evolution in the microstructure from amorphous to partial crystalline precipitation was observed in one as-cast $Nd_{60}Fe_{30}Al_{10}$ sample. A featureless amorphous phase was observed at the periphery, and a network-like structure consisting of the Fe-rich, Nd-rich and amorphous regions was formed in the center of the sample. As a consequence of the different microstructures, two magnetic structures, fine strip-like domains characterized by a dark region adjacent to a bright region at a sub-micron scale and sunflower-like domains at a micron scale, were observed at the periphery and the center of the cross section, respectively. The presence of a small step in the hysteresis curve of the as-cast alloy further revealed that the two magnetic domains have different coercivity.

(3) The magnetic behavior of an as-cast $Nd_{55}Fe_{28}Al_9Ni_8$ alloy, consisting of nanoclusters, no larger than 5nm, embedded in the amorphous matrix, was investigated at different temperatures. Only one magnetic phase was detected at room temperature. However, another magnetic phase was also identified by the step observed in the hysteresis loop at low temperature. The two types of magnetic phase behavior was associated with the different response of magnetic phases to the external field, during the temperature change.

(4) The magnetic behavior in Nd-based bulk metallic glass was further understood through Monte Carlo simulation. The hysteresis loops of various cluster systems have been investigated. It was found that the coercivity of a cluster system is closely related to the change of temperature and anisotropy of the system. By overlapping the hysteresis loops of two cluster systems with different anisotropy at

different temperatures, a step is only observed when the system is at a low temperature. The result of the temperature related occurrence of the step in the hysteresis loop is consistent with the observation in the experimental examination in bulk metallic glass based alloy.

In a nutshell, this study not only provides a better understanding of the origin of the hard magnetic properties in bulk metallic glasses but also proposes possible solutions, such as minor-alloying, changing the cooling rate, as well as choosing the most suitable working temperature for improvement of the magnetic properties.

Chapter 9 Future Work

In the present investigation, the magnetic behavior of Nd-based bulk metallic glasses containing of two kinds of short range ordered structures, i.e., the nanocluster and amorphous phase, has been studied. The interaction between the two magnetic phases has yet to be examined, and it would be very interesting to examine, by simulation, if interaction exits between the two magnetic phases. The results will definitely help in fully understanding the magnetism in rare earth based bulk metallic glasses.

Besides, the dependence of magnetic behaviour with different particle sizes is a topic of current interest in the research of nanoparticle systems. Too large or too small particle sizes will weaken the magnetic properties of the magnetic nanoparticles. Up to now, little work has been done on the effect of nanocluster size on the magnetic properties of the BMGs. According to the findings of the present study, nanoclusters of sizes no larger than 5nm have been observed. However, the size effect has yet to be investigated in details and it is most worthwhile to study because the findings are important in developing a magnetic BMG with enhanced properties for a variety of applications.

Chapter 10 Statement of Originality and Contribution to Knowledge

In the past decades, a considerable number of investigations have been carried out on the understanding the origin of magnetic properties in RE-based bulk metallic glasses. However, the mechanism is still not very clear. In order to have a better understanding of magnetism in RE-based bulk metallic glasses, the dependence of magnetic properties on the microstructure of RE-based bulk metallic glasses have been investigated in this project, and the main contribution of this work to knowledge are summarized as follows:

1) A new kind of RE-TM bulk metallic glass with good glass forming ability and hard magnetic properties, was prepared by the addition of Ni, and the microstructure and magnetic properties were examined for the first time in this project.

2) An apparent transition from an almost featureless amorphous structure to partial precipitation was first observed from the edge to the center of the cross-section of one sample. In the corresponding regions, a transition in magnetic structure was also observed.

3) In present study, the existence of one magnetic phase was observed at room temperature, which is consistent to the observation of other researchers. However, at low temperature, another magnetic phase was

detected for the first time from the evidence of a step in the hysteresis loop. Monte Carlo simulation was also applied for the first time to understand the magnetic behavior of the two magnetic phases at different temperatures. The findings were consistent with the experimental results.

References

[1] R. H. J. Fastenau and E. J. V. Loenen, Application of rare earth permanent magnets, *Journal of Magnetism and Magnetic Materials*, 157-158 (1996) 1-6

[2] A. Inoue, A. Kojima, A. Takeuchi, T. Masumoto and A. Makino, Hard and soft magnetic properties of nanocrystalline Fe-Nd-Zr-B alloys containing intergranular amorphous phase, *Journal of Applied Physics*, 79 (1996) 4836

[3] S. Hirosawa, Y. Shigemoto, T. Miyoshi, and H. Kanekiyo, Direct formation of $Fe_3B/Nd_2Fe_{14}B$ nanocomposite permanent magnets in rapid solidification, *Scripta Materialia*, 48 (2003) 839-844

[4] A. Inoue, Bulk amorphous alloys with soft and hard magnetic properties, *Materials Science and Engineering A*, 226-228 (1997) 357-363

[5] A. Inoue, T. Zhang, W. Zhang and A.Takeuchi, Bulk Nd-Fe-Al amorphous alloys with hard magnetic properties, *Materials Transactions, JIM.*, 37 (1996) 99-108

[6] A. Inoue, T.Zhang and A.Takeuchi, Preparation of bulk Pr-Fe-Al amorphous alloys and characterization of their hard magnetic properties, *Materials Transactions, JIM.*, 37 (1996) 1731-1740

[7] A.Inoue, T.Zhang and A.Takeuchi, Hard magnetic bulk amorphous alloys, *IEEE Transactions on Magnetics*, 33 (1997) 3814-3816

[8] H. Chiriac, N. Lupu, K.V. Rao and R.E. Vandenberghe, Magnetic behavior of

$Nd_{50}Fe_{40}Al_{10}$ bulk amorphous alloys, *IEEE Transactions On Magnetics*, 37 (2001) 2509-2511

[9] B.C. Wei, W. H. Wang, M. X. Pan, B. S. Han, Z. R. Zhang and W. R. Hu, Domain structure of a $Nd_{60}Al_{10}Fe_{20}Co_{10}$ bulk metallic glass, *Physical Review B*, 64 (2001) 012406/1-4

[10] H. Z. Kong, Y. Li and J. Ding, Effect of boron addition to the hard magnetic bulk $Nd_{60}Fe_{30}Al_{10}$ amorphous alloy, *Journal of Magnetism and Magnetic Materials*, 217 (2000) 65-73

[11] G. J .Fan, W. Loser, S. Roth, J. Eckert and L. Schultz, Glass-forming ability and magnetic properties of $Nd_{70-x}Fe_{20}Al_{10}Co_x$ alloys, *Journal of Materials Research*, 15 (2007) 1556-1563

[12] W. Klement, R. Willens and P. Duwez, Non-crystalline structure in solidified gold-silicon alloys, *Nature*, 187 (1960) 869-870

[13] R. Haseqawa, Soft magnetic properties of metallic glasses, *Journal of Magnetism and Magnetic Materials*, 41(1983) 79-85

[14] S.K. Sharma, P. Mukhopadhyay, P.K. Chaohan and S. K. Kulkarni, Studies on the corrosion of two multicomponent iron base metallic glasses in potassium sulphate solution, *Corrosion Science*, 30(1990) 313-324

[15] A. Pratap, K.G. Raval, A. Gupta and S.K. Kulkarni, Nucleation and growth of a multicomponent metallic glass, *Bulletin of Materials Science*, 23 (2000) 185-188

[16] H. Chiriac, T.A. Ovari, G. Pop and F. Barariu, Magnetic behavior of

nanostructured glass covered metallic wires, *Journal of Applied Physics*, 81(1997) 5817-5819

[17] Y. Watanabe, Y. Nakamura, J.T. Dickinson, D.M. Kulawansa and S.C. Langford, Nanometer-scale observations of metallic glass fracture surfaces, *Materials Science and Engineering A*, A176 (1994) 411-415

[18] A. Nafalski, A. Wac-Wlodarczyk and H. Stryczewska, Metallic glass cores for airborne equipment, *Journal of Magnetism and Magnetic Materials*, 112 (1992) 325-327

[19] J.B. Suck, P.A. Egelstaff, R. A. Robinson, D.S. Sivia and A.D. Taylor, Neutron Brillouin scattering in a metallic glass , *Journal of Non-Crystalline Solids*, 150 (1992) 245-250

[20] H. S. Chen and D. Turnbull, Formation, stability and structure of palladium-silicon based alloy glasses, *Acta Metalurgical*, 17 (1969) 1021-1031

[21] H. S. Chen, Thermodynamic considerations on the formation and stability of metallic glasses, *Acta Metallurgica*, 22 (1974) 1505-1511

[22] H. W. Kui, A. L. Greer and D. Turnbull, Formation of bulk metallic glass by fluxing, *Applied Physics Letters*, 45(1984)615-616

[23] H. W. Kui and D. Turnbull, The melting of $Ni_{40}Pd_{40}P_{20}$ glass, *Applied Physics Letters* , 47 (1985) 796-797

[24] A. Inoue, M. Kohinata, A. P. Tsai and T. Masumoto, Mg-Ni-La amorphous alloys with a wide supercooled liquid region, *Materials Transaction.,JIM*. 30(1989) 378-381

[25] A. Inoue, T Zhang and T. Masumoto, Al-La-Ni amorphous alloys with a wide supercooled liquid region, *Materials Transaction JIM*, 30 (1989) 965-972

[26] A. Inoue, T. Zhang and T. Masumoto, Zr-Al-Ni amorphous alloys with high glass transition temperature and significant supercooled liquid region, *Materials Transaction.,JIM* 31 (1990) 177-183

[27] A. Inoue and J. S. Gook, Fe-based ferromagnetic glassy alloys with wide supercooled liquid region, *Materials Transaction.,JIM*, 36 (1995) 1180-1183

[28] A. Inoue, T. Zhang, T. Itoi and A. Tackeuchi, New Fe-Co-Ni-Zr-B amorphous alloys with wide supercooled liquid regions and good soft magnetic properties, *Materials Transaction.,JIM* , 38 (1997) 359-362

[29] A. Inoue, T. Zhang and A Tackeuchi, Bulk amorphous alloys with high mechanical strength and good soft magnetic properties in Fe-TM-B (TM=IV-VII group transition metal) system, *Applied Physics Lettesr* , 71 (1997) 464-466

[30] A. Inoue, M. Koshiba, T. Itoi and A. Makino, Ferromagnetic Co-Fe-Zr-B amorphous alloys with glass transition and good high-frequency permeability, *Applied Physics Letters*, 73 (1998) 744-746

[31] D. H. Xu, B. Lohwongwatana, G. Duan, W.L. Johnson and C. Garland, Bulk metallic glass formation in binary Cu-rich alloy series $Cu_{100-x}Zr_x$ (x=34 , 36, 38.2, 40 at.%) and mechanical properties of bulk $Cu_{64}Zr_{36}$ glass, *Acta Materialia*, 52 (2004) 2621-262

[32] D. Wang, Y. Li, B.B. Sun, M.L. Sui, K. Lu and E. Ma, Bulk metallic glass formation in the binary Cu-Zr system, *Applied Physics Letters*, 84 (2004)

4029-4031

[33] L. Xia, S.T. Shan, D. Ding and Y. D. Dong, Binary bulk metallic glass $Ni_{62}Nb_{38}$ with high compressive strength of 3100 MPa, *Intermetallics*, 15 (2007) 1046-1049

[34] X.F. Liu, R. J. Wang, D.Q. Zhao, M.X. Pan and W.H. Wang, Bulk metallic glasses based on binary cerium and lanthanum elements, *Applied Physics Letters*, 91(2007) 041901

[35] A. Inoue, T. Zhang, A. Takeuchi and W. Zhang, Hard magnetic bulk amorphous Nd-Fe-Al alloys of 12 mm in diameter made by suction casting, *Materials Transactions, JIM.*, 37 (1996) 636-640

[36] B.C. Wei, Y. Zhang, Y. X. Zhuang, D. Q. Zhao, M. X. Pan and W. H. Wang, $Nd_{65}Al_{10}Fe_{25-x}Co_x$ (x=0,5,10) bulk metallic glasses with wide supercooled liquid regions, *Journal of Applied Physics*, 89 (2001) 3529-3531

[37] L. Xia, M.B. Tang, H. Xu, M.X. Pan, D.Q. Zhao, W.H. Wang and Y.D. Dong, Kinetic nature of hard magnetic $Nd_{50}Al_{15}Fe_{15}Co_{20}$ bulk metallic glass with distinct glass transition, *Journal of Materials Research*,19 (2004) 1307-1310

[38] P.G. Debenedetti and F. H. Stillinger, Supercooled liquids an the glass transition, *Nature*, 410 (2001) 259-267

[39] A. Inoue, Stabilization of metallic supercooled liquid and bulk amorphous alloys, *Acta Materialia*, 48 (2000) 279-306

[40] A. Peker and W.L. Johnson, A highly processable metallic glass: $Zr_{41.2}Ti1_{3.8}Cu1_{2.5}Ni_{10.0}Be_{22.5}$, *Applied Physics Letters*, 63 (1993) 2342-2344

[41] Jürn, W. P. Schmelzer, Nucleation theory and applications, Weinheim : Wiley-VCH, 2005

[42] J. W. Mullin, Crystallization, Butterworth Heinemann, 2001

[43] D. R. Uhlmann, Kinetic treatment of glass formation, *Journal of Non-crystalline Solids*, 7 (1972) 337-348

[44] S. R. Nagel and J. Taue, Nearly-free-electron approach to the theory of metallic glass alloys. *Physical Review Letters*, 35 (1975) 380–383

[45] N. F. Mott and H. Jones, The theory of the properties of metals and alloys, Oxford University Press, Oxford, U.K., 1936

[46] C. Barret and T. B. Massalski, Structure of metals, McGraw Hill, New York, 1966

[47] T. B. Massalski and U. Mizutani, Electronic structure of Hume-Rothery phases, *Progress in Materials Science*, 22 (1978) 151-262

[48] Q. Jiang, B. Q. Chi and J. C. Li, A valence electron concentration criterion for glass-forming ability of metallic liquids, *Applied Physics Letters*, 82 (2003) 2984-2986

[49] Y. M. Wang, J. B. Qiang, C. H. Wong and C. H. Chek, C. Dong, Composition rule of bulk metallic glasses and quasicrystals using electron concentration criterion, *Journal of Materials Research*, 18 (2003) 642-648

[50] W. Chen, Y. Wang, J. Qiang and C. Dong, Bulk metallic glasses in Zr-Al-Ni-Cu system, *Acta Materialia*, 51 (2003) 1899-1907

[51] Y. M. Wang, C. H. Shek, J. B. Qiang, C. H. Wong, W. R. Chen and C. Dong, The

e/a factor governing the formation and stability of (Zr76Ni24)1-xAlx bulk metallic glasses, *Scripta Materiala*, 48 (2003) 1525-1529

[52] Y. M. Wang, X. F. Zhang, J. B. Qiang, Q. Wang, D. H. Wang, D.J. Li, C. H. Shek and C. Dong, Composition optimization of the Al-Co-Zr bulk metallic glasses, *Scripta Materiali*a, 50 (2004) 829-833

[53] D. Turnbull, Under what conditions can a glass be formed? *Contemporary Physics* 10 (1969) 473-488

[54] Z. P. Lu and C. T. Liu, A new glass-forming ability criterion for bulk metallic glasses, *Acta Materialia*, 50 (2002) 3501-3512

[55] P. Hassen, *Physical Metallurgy* 3rd ed. Cambridge: Cambridge University Press; 1996: 110-148

[56] A. Inoue, High strength bulk amorphous alloys with low critical cooling rates, *Materials Transactions, JIM*, 36 (1995) 866-875

[57] A. Inoue and A. Takeuchi, Recent progress in bulk glassy alloys, *Materials Transaction, JIM.*, 43 (2002) 1892-1906

[58] R. Wang, Short-Range structure for amorphous intertransition metal alloys, *Nature*, 278 (1979) 700-704

[59] A. Inoue, Stabilization of metallic supercooled liquid and bulk amorphous alloys, *Acta Materialia*, 48 (2000) 279-306

[60] J. Eckert, N. Mattern and M. Seidel. Crystallization behavior and phase formation in Zr-Al-Cu-Ni metallic glass containing oxygen, *Materials Transaction. JIM.*, 39 (1998) 623-632

[61] W. H. Wang, E. Wu, R.J. Wang, S. J. Kennedy and A. J. Studer, Phase transformation in a $Zr_{41}Ti_{14}Cu_{12.5}Ni_{10}Be_{22.5}$ bulk amorphous alloy upon crystallization, *Physical Review B*, 66 (2002) 104205/1-5

[62] J. Saida, M. Matsushita and A. Inoue, Direct observation of icosahedral cluster in $Zr_{70}Pd_{30}$ binary glassy alloy, *Applied Physics Letters*, 79 (2001) 412-414

[63] T. A. Waniuk, J. Schroers and W.L. Johnson, Timescales of crystallization and viscous flow of the bulk glass-forming Zr-Ti-Ni-Cu-Be alloys, *Physical Review B*, 67 (2003) 184203-1842039

[64] D. Holland-Moritz, Observation of the undercoolability of quasicrystal-forming alloys by electromagnetic levitation, *Physical Review Letters*, 71 (1993) 1196-1199

[65] A. Inoue, A. Takeuchi and T. Zhang, Ferromagnetic bulk amorhous alloys, *Metallurgical and Materials Transactions*, 29A (1998) 1779-1793

[66] S. Schneider, A. Bracchi, K. Samwer, M. Seibt and P. Thiyagarajan, Microstructure-controlled magnetic properties of the bulk glass-forming alloy $Nd_{60}Fe_{30}Al_{10}$, *Applied Physics Letters*, 80(2002) 1749-1751

[67] Z.G. Sun, G. Kumar, W. Löser, J. Eckert, K.H. Müller and L. Schultz, Glass forming ability of $Nd_{60}TM_{30}Al_{10}$ (TM = Fe, Co, Ni, Cu, Mn) alloys, *Materials Science and Engineering A*, 375-377 (2004) 403-406

[68] F. J. G Landgraf, F. P. Missell, G. Knoch, B. Grieb and E.-Th.Henig, Binary Fe-Nd metastable phases in the solidification of Fe-Nd-B alloys, Journal of Applied Physics, 70 (1991) 6107-6109

[69] K.V. Rao, R. Malmhall, G. Backstron and S. M. Bhagat, Hall effect in amorphous magnetic materials-Metglas 2826 and 2826B, *Solid State Communications*, 19 (1976) 193-195

[70] E. Figueroa, L.Lundgren, O. Beckman and S. M. Bhagat, The anomalous magnetisation of amorphous Metglas 2826-A, *Solid State Communications*, 20 (1976) 961-964

[71] R. Malmhall, G. Backstrom, K.V. Rao, S. M. Bhagat, M. Meichle and M. B. Salamon, Metglas 2826B-transport, magnetic and thermal properties, *Journal of Applied Physics*, 49 (1978) 1727-1729

[72] W.H. Wang, C. Dong and C.H. Shek, Bulk metallic glass, *Materials Science Engineering R*, 44 (2004) 45-89

[73] www.liquidmetals.com

[74] M. Telfold, The case for bulk metallic glass, *Materials Today*, 7 (2004) 36-43

[75] A. Inoue, K. Hashimoto, Amorphous and nanocrystaline Materials: Preparation, Properties, and Applications, *Advances in Materials Research*, Springer, Tokyo, 2001

[76] D. Jiles, *Introduction to magnetism and magnetic materials*, 1st ed, London, Chapman and Hall, 1991, 74

[77] P.Weiss, L'Hypothese du Champ Moléculaire et la Pro- priété Ferromagnétique, *Journal de Physique Théorique et Appliquée*, 6 (1907) 661–690

[78] J.A. Fernandez-Baca and W. Y. Ching, *The magnetism of amorphous metals and alloys*, Singapore, World Scientific Publishing Co.Pte.Ltd, 1995, 143

[79] H. Kronmülle and M. Fähale, *Micromagnetism and the microstructure of ferromagnetic solids*, Cambridge, Cambridge University Press, 2003, 320

[80] K.A. Gschneidner Jr and L. Eyring, *Handbook on the Physics and Chemistry of Rare-Earths* 24, Amsterdam, 1997, 339

[81] N.H. Duc, T.D. Hien, D. Givord, J.J.M. Franse and F.R. de Boer, Exchange interactions in rare earth-transition metal compounds, *Journal of Magnetism and Magnetic Materials*, 124 (1993) 305-311

[82] N.H. Duc and D. Givord, Exchange interactions in amorphous Gd-Co alloys, *Journal of Magnetism and Magnetic Materials*, 157–158 (1997) 169-170

[83] R. Harris, M. Plischke and M.J.Zuckermann, New Model for Amorphous Magnetism, *Physical Review Letters*, 31 (1973) 160-162

[84] K. G. Knoch, B. Grieb, E. T. Henig, H. Kronmuller and G. Petzow, Upgraded Nd-Fe-B-AD (AD = Al, Ga) magnets: Wettability and microstructure, *IEEE Transactions on Magnetics*, 26 (1990) 1951-153

[85] J. Ding, Y. Li and X. Z. Wang, The coercivity of rapidly quenched $Nd_{60}Fe_{30}Al_{10}$ alloys, *Journal of Physics D: Applied Physics*, 32 (1999) 713-716

[86] X. Z. Wang, Y. Li, J. Ding, L. Si and H. Z. Kong, Structure and magnetic characterization of amorphous and crystalline Nd-Fe-Al alloys, *Journal of Alloys and Compounds*, 290 (1999) 209-215

[87] H. Chiriac and N. Lupu, New bulk amorphous magnetic materials, *Physica B*, 299(2001) 293-301

[88] R. Alben, J. J. Becker and M. C. Chi, Random anisotropy in amorphous

ferromagnets, *Journal of Applied Physics*, 49 (1978) 1653-1658

[89] G. Kumar, J. Eckert, S. Roth, K. -H. Müller and L. Schultz, Coercivity mechanism in mold-cast $Nd_{60}Fe_xCo_{30-x}Al_{10}$ bulk amorphous alloys, *Journal of Alloys and Compounds*, 348 (2003) 309-313

[90] A. Bracchi, K. Samwer, S. Schneider and J. F. Löffler, Random anisotropy and domain-wall pinning process in the magnetic properties of rapidly quenched $Nd_{60}Fe_{30}Al_{10}$, *Applied Physics Letters*, 82 (2003) 721-723

[91] R. W. McCallum, L. H. Lewis, M. J. Kramer and K. W. Dennis, Magnetic aspects of the ferromagnetic "bulk metallic glass" alloy system Nd-Fe-Al, *Journal of Magnetism and Magnetic Materials*, 299 (2006) 265-280

[92] R. Sato Turtelli, D. Triyono, R. Grossinger, H. Michor,J. H. Espina, J. P. Sinnecker, H. Sassik, J. Eckert, G. Kumar,Z. G. Sun and G. J. Fan, Coercivity mechanism in $Nd_{60}Fe_{30}Al_{10}$ and $Nd_{60}Fe_{20}Co_{10}Al_{10}$ alloys, *Physical Review B*, 66 (2002) 054441/1-8

[93] E. Olivetti, E. Ferrara, P. Tiberto and M. Baricco, Magnetic and structural characterization of partially amorphous $Nd_{70}Fe_{20}Al_{10}$, *Journal of Magnetism and Magnetic Materials*, 272-276 (2004) e1949-e1951

[94] E. Olivetti, M. Baricco, E. Ferrara, P. Tiberto and L. Martino, Effect of annealing on the magnetic properties of $Nd_{70}Fe_{20}Al_{10}$ bulk metallic glasses, *Journal of Magnetism and Magnetic Material*, 290-291 (2005) 1214-1216

[95] J.F. Löffler, Bulk metallic glasses, *Intermetallics*, 11 (2003) 529-540

[96] X. Hu, S.C. Ng, Y.P. Feng and Y. Li, Glass forming ability and in-situ

composite formation in Pd-based bulk metallic glasses, *Acta Materialia*, 51 (2003) 561-572

[97] X.H. Lin, W.L. Johnson and W.K. Rhim, Effect of oxygen impurity on crystallization of an undercooled bulk glass forming Zr-Ti-Cu-Ni-Al alloy, *Materials Transaction JIM.*, 38 (1997) 473-477

[98] Y. Liu, H. Bei, C. T. Liu, E. P. George, Cooling-rate induced softening in a Zr50Cu50 bulk metallic glass, *Applied Physics Letters*, 90 (2007) 71909/1-3

[99] W.H. Wang, R.J. Wang, D.Y. Dai, D.Q. Zhao, M.X. Pan and Y.S. Yao, Pressure-induced amorphization of ZrTiCuNiBe bulk glass-forming alloy, *Applied Physics Letters*, 79 (2001) 1106-1108

[100] S. Flege, H. Hahn and R. S. Averback, Thermal and radiation-enhanced diffusion in the bulk metallic glass $Ni_{23}Zr_{62}Al_{15}$, *Physical Review B*, 69 (2004) 14303/1-7

[101] W. H. Wang, Roles of minor additions in formation and properties of bulk metallic glasses, *Progress in Materials Science*, 52 (2007) 540-596

[102] B. Zhang, D. Q. Zhao, M. X. Pan, W. H. Wang and A. L. Greer, Amorphous metallic plastic, *Physical Review Letters*, 94 (2005) 205502/1-4

[103] P. Yu, H. Y. Bai, M.B. Tang and W. L. Wang, Excellent glass-forming ability in simple $Cu_{50}Zr_{50}$ based alloys, *Journal of Non-Crystalline Solids*, 351 (2005) 1328-1332

[104] X.K. Xi, D.Q. Zhao, M.X. Pan and W.H. Wang, Highly processable $Mg_{65}Cu_{25}Tb_{10}$ bulk metallic glass, *Journal of Non-Crystalline Solids*, 344

(2004) 189-192

[105] H. Choi-Yim, R. Busch, U. Koster and W.L. Johnson, Synthesis and characterization of particulate reinforced $Zr_{57}Nb_5Al_{10}Cu_{15.4}Ni_{12.6}$ bulk metallic glass composites, *Acta Materialia*, 47 (1999) 2455-2462

[106] W.H. Wang and H.Y. Bai, Carbon-addition-induced bulk ZrTiCuNiBe amorphous matrix composite containing ZrC particles, *Materials Letters*, 43 (2000) 59-63

[107] W. H. Wang, Q. Wei and H. Y. Bai, Enhanced thermal stability and microhardness in Zr–Ti–Cu–Ni–Be bulk amorphous alloy by carbon addition, *Applied Physics Letters*, 71 (1997) 58-60

[108] X.J. Gu, A.G. McDermott, S.J. Poon and G.J. Shiflet, Critical Poisson's ratio for plasticity in Fe-Mo-C-B-Ln bulk amorphous steel, *Applied Physics Letters*, 88 (2006) 211905/1-3

[109] W.H. Wang, M.X. Pan, D.Q. Zhao, Y. Hu and H.Y. Bai, Enhancement of the soft magnetic properties of FeCoZrMoWB bulk metallic glass by microalloying, *Journal of Physics: Condens Matter*, 16 (2004) 3719-3723

[110] Y.T. Wang, Z.Y. Pang, R.J. Wang, D.Q. Zhao, M.X. Pan, B.S. Han, W.L. Wang and W.H. Wang , Doping-induced formation of bulk nanocrystalline alloy from metallic glass with controllable microstructure and properties, *Journal of* Non-Crystalline Solids, 352 (2006) 444- 449

[111] A. Inoue, T. Zhang and T. Masumoto, Glass-forming ability of alloys, *Journal of Non-Crystalline Solids*, 156-158 (1993) 473-480

[112] A. Inoue, High Strength Bulk Amorphous Alloys with Low Critical Cooling Rates, *Materials Transactions, JIM*, 36 (1995) 866-875

[113] A.L. Greer, Confusion by design, *Nature*, 366 (1993) 303-304

[114] Y. Zhang, W. Xu, H. Tan and Y. Li, Microstructure control and ductility improvement of La-Al-(Cu, Ni) composites by Bridgman solidification, *Acta Materialia*, 53 (2005) 2607-2616

[115] W. Löser, J. Das, A. Güth, H.-J. Klauβ, X, C. Mickel, U. Kühn, J. Eckert, S.K. Roy and L. Schultz, Effect of casting conditions on dendrite-amorphous/nanocrystalline Zr-Nb-Cu-Ni-Al in situ composites, *Intermetallics*, 12 (2004) 1153-1158

[116] M. Yan, J. Zou and J. Shen, Cooling rate effects on the microstructure and phase formation in $Zr_{51}Cu_{20.7}Ni_{12}Al_{16.3}$ bulk metallic glass, *Science and Technology of Advanced Materials*, 7 (2006) 806–811

[117] J. J. Croat, Permanent magnetic properties of rapid quenched rare earth-iron alloys, *IEEE, Transaction on Magnetics*, Mag-18(1982)1442-1447

[118] Y. Li, J. Ding, S. C. Ng and X. Z. Wang, Unusual magnetization anisotropy in amorphous Nd-Fe-Al ribbons, *Journal of Magnetism and Magnetic Materials*, 187 (1998) L273- L277

[119] R. C. Taylor, T. R. McGuire, J. M. D. Coey and A. Gangulee, Magnetic properties of amorphous neodymium-transition-metal films, *Journal of Applied Physics*, 49 (1978) 2885-2893

[120] J. J. Croat, J. F. Herbst, R. W. Lee and P.E. Pinkerton, High-energy product

Nd-Fe-B permanent magnets, *Applied Physics Letters*, 44 (1984) 148-149

[121] F. R. Missell, H. R. Rechenberg, V. Villas-Boas, F.J.G. Landgraf, in Magnetism, magnetic materials and their applications : proceedings of the international workshop, Section III, edited by F. Leccabue, J.L. Sanchez Llamazares, La Habana, Cuba, 21-29 1991; 287

[122] X. Z. Wang, Y. Li, J. Ding, L. Si and H. Z. Kong, Structure and magnetic characterization of amorphous and crystalline Nd-Fe-Al alloys, *Journal of Alloys and Compounds*, 290 (1999) 209-215

[123] W. Zhang, A. Takeuchi and A. Inoue, Amorphous Nd-Fe-Si thick ribbons and their hard magnetic properties, *Materials Transactions, JIM*, 38 (1997) 1027-1030

[124] Z. G. Sun, W. Loser, J. Eckert, K. H. Muller and L. Schultz, Effect of cooling rate on microstructure and magnetic properties of $Nd_{60}Fe_{30}Al_{10}$ hard magnetic alloys. *Journal of Magnetism and Magnetic Materials*, 261 (2003) 122-130

[125] R. Gupta, A. Gupta, A. K. Nigam and G. Chandra, Effect of induced disorder on low temperature resistivity of some non-magnetic and magnetic metallic glasses, *Journal of Alloys and Compounds*, 326 (2001) 275-279

[126] H. Fu, X. Y. Zhang, H. J. Yu, B. H. Teng and X. T. Zu, Large magnetic entropy change of Gd-based ternary bulk metallic glass in liquid-nitrogen temperature range, *Solid State Communications*, 145 (2008) 15-17

[127] I. Skorvanek, P. Duhaj and R. Grossinger, Low-temperature magnetic

behaviour in amorphous and nanocrystalline Fe-Nb-B alloys, *Journal of Magnetism and Magnetic Materials*, 215-216 (2000)431-433

[128] Z. Li, H. Y. Bai, Z. J. Chen, M. X. Pan, D. Q. Zhao, W. L. Wang and W. H. Wang, Investigation of magnetic properties at low temperatures on permanent magnetic $Nd_{60}Al_{10}Fe_{20}Co_{10}$ bulk metallic glass, *Acta Physica Sinica*, 52 (2003) 1461-1464 (in Chinese)

[129] K. Binder and D.W. Heermann, Monte Carlo simulation in statistical physics : an introduction, Berlin ; New York : Springer, 2002.

[130] Rubinstein, Reuven Y. Simulation and the Monte Carlo method, Hoboken, N.J.; John Wiley & Sons, 2008.

[131] M. E. J. Newman and G.T. Barkerma, *Monte Carlo Methods in Statistical Physics*, Clarendon, Oxford, (1999)

[132] P. Vargas, D. Altbir and J. d'Albuquerque e Castro, Fast Monte Carlo method for magnetic nanoparticles, *Physical Review B*, 73 (2006) 92417/1-3

[133] H. K, Lee, T. C. Shulthess, D. P. Landau, G. Brown, J. P. Pierce, Z. Gai, G.. Farnam and J. Shen, Monte Carlo simulations of interacting magnetic nanoparticles, *Journal of Applied Physics*, 91(2002) 6926-6928

[134] W. Figueiredo and W. Figueiredo, Magnetic properties of interacting nanoparticles in a triangular lattice: Monte Carlo simulations, *Physical Review B*, 77(2008) 104419/1-9

[135] J. Mazo-Zuluaga, J. Restrepo and J. Mejia-Lopez, Effect of surface anisotropy on the magnetic properties of magnetite nanoparticles: a

Heisenberg-Monte Carlo study, *Journal of Applied Physics*, 103 (2008)113906/1-8

[136] Y. Laosiritaworn, S. Ananta and R. Yimnirun, Temperature effects in the magnetic properties of two-dimensional Ising square lattices: a Monte Carlo investigation, *Physical Review B* ,75(2007)54417/1-9

[137] B. Molina Concha, E. De Biasi and R.D. Zysler, Monte Carlo simulation of Fe-Co amorphous nanoparticles magnetization, *Physica B: Condensed Matter*, 403 (2008) 390-393

[138] L.Wang, J. Ding, H. Z. Kong, Y. Li and Y. P. Feng, Monte Carlo simulation of a cluster system with strong interaction and random anisotropy, Physical Review B, 64 (2001) 214410/1-10

[139] N. Lupu, R.L. McGreevy and H Chiriac, Magnetic structure determination for $Nd_{90-x}Fe_xAl_{10}$ glassy hard magnets using RMC modeling of neutron diffraction data, *Materials Science and Engineering A*, A375-A377 (2004) 1105-1109

[140] D. Cimpoesu, L. Stoleriu, A.Stancu, N. Lupu and H. Chiriac, Simulation of magnetic properties versus temperature for RE-TM based amorphous alloy, IEEEE Transaction on Magnetics, 40 (2004) 2730-2732

[141] A. Inoue, Slowly-cooled bulk amorphous alloys, *Materials Science Forum*, 179-181(1995) 691-700

[142] A. Inoue, T. Nakamura, T. Sugita, T. Zhang and T. Masumoto, Bulky La-Al-TM (TM = transition metal) amorphous alloys with high tensile strength

produced by a high-pressure die casting method, *Materials Transaction., JIM*, 34(1993) 351-358

[143] A. Inoue, Y. Shinohara, Y. Yokoyama and T. Masumoto, Solidification analyses of bulky $Zr_{60}Al_{10}Ni_{10}Cu_{15}Pd_5$ glass produced by casting into wedge-shape copper mold, *Materials Transaction., JIM*, 36(1995)1276-1281

[144] User's manual of Digital Instruments NanoScope V for magnetic force microscopy part

[145] M. X. Pan, B. C. Wei, L. Xia, W. H. Wang, D. Q. Zhao, Z. Zhang and B. S. Han, Magnetic properties and microstructural characteristics of bulk Nd-Al-Fe-Co glassy alloys, *Intermetallics*, 10(2002) 1215-1219

[146] A. Inoue and T. Zhang, Thermal stability and glass-forming ability of amorphous Nd-Al-TM (TM=Fe, Co, Ni or Cu) alloys, *Materials Science and Engineering A*, A 226-228 (1997) 393-396

[147] B. L. Shen, H. Koshiba, T. Mizushima and A. Inoue, Bulk amorphous Fe-Ga-P-B-C alloys with a large supercooled liquid region, *Materials Transactions JIM.*, 41 (2000) 873-876

[148] Z.G. Sun, G. Kumar, W. Löser, J. Eckert, K.H. Müller and L. Schultz, Glass forming ability of $Nd_{60}TM_{30}Al_{10}$ (TM = Fe, Co, Ni, Cu, Mn) alloys, *Materials Science and Engineering A*, 375-377 (2004) 403-406→76

[149] B.C. Wei, W. Löser, L. Xia, S. Roth, M.X. Pan, W. H. Wang and J. Eckert, Anomalous thermal stability of Nd-Fe-Co-Al bulk metallic glass, Acta Materialia 50 (2002) 4357-4367

[150] Z.P. Lu, C.T. Liu and W.D. Porter, Role of yttrium in glass formation of Fe-based bulk metallic glasses, *Applied Physics Letters*, 83(2003) 2581-2583

[151] X.S. Xiao, S.S. Fang, G.M. Wang, H. Qin and Y.D. Dong, Influence of beryllium on thermal stability and glass-forming ability of Zr-Al-Ni-Cu bulk amorphous alloys, *Journal of Alloys and Compounds*, 376 (2004) 145-148

[152] L. Liu, C. L. Qiu, H. Zou and K.C. Chan, The effect of the microalloying of Hf on the corrosion behavior of ZrCuNiAl bulk metallic glass, *Journal of Alloys and Compounds*, 399(2005)144-148

[153] Y. Yokoyama, A. Kobayashi, K. Fukaura and A. Inoue, Oxygen embrittlement and effect of the addition of Ni element in a bulk amorphous Zr-Cu-Al alloy, *Materials Transactions*, 43 (2002) 571-574

[154] Y. Yokoyama, K. Fukaura and A. Inoue, Effect of Ni addition on fatigue properties of bulk glassy $Zr_{50}Cu_{40}Al_{10}$ alloys, *Materials Transactions*, 45 (2004) 1672-1768

[155] G. Kumar, J. Eckert, L. Schultz and S. Ram, Formation and thermal stability of cluster structure in $Nd_{55}Cu_{15}Ni_{10}Co_5Al_{15}$ bulk amorphous alloy, *Materials Letters*, 53 (2002) 305-315

[156] A L Greer, Metallic glasses, *Science*, 267(1995) 1947-1953

[157] P. J. Desré, Confusion principle and thermodynamics, *Materials Science Forum*, 179-181(1995) 713-722

[158] P. J. Desré, On the effect of the number of components on glass-forming ability of alloys from the liquid state: application to the new generation of

multicomponent bulk glasses, *Materials Transactions, JIM*, (1997) 583-588

[159] J .J. Croat, Magnetic hardening of Pr-Fe and Nd-Fe alloys by melt-spinning, *Journal of Applied Physics*, 53(1982) 3161-3169

[160] A. Takeuchi and A. Inoue, Size dependence of soft to hard magnetic transition in (Nd, Pr)-Fe-Al bulk amorphous alloys, *Materials Science and Engineering A*, A375-377 (2004) 1140-1144

[161] H. Chiriac and N. Lupu, Coercivity and phase transitions of clustered $Nd_{90-x}Fe_xAl_{10}$ bulk hard magnets, *Materials Transactions*, 43(2002)1992-1999

[162] Z. G. Sun, W. Löser, J. Eckert, K.H. Muller and L. Schultz, Phase separation in $Nd_{60-x}Y_xFe_{30}Al_{10}$ melt-spun ribbons, *Applied Physics Letters*, 80(2002) 772-774

[163] L. Q. Xing, J. Eckert, W. Löser, S. Roth and L. Schultz, Atomic ordering and magnetic properties in $Nd_{57}Fe_{20}B8Co_5Al_{10}$ solids, *Journal of Applied Physics*, 88 (2000) 3565-3569

Appendix I Set-up windows for the Monte Carlo Simulation

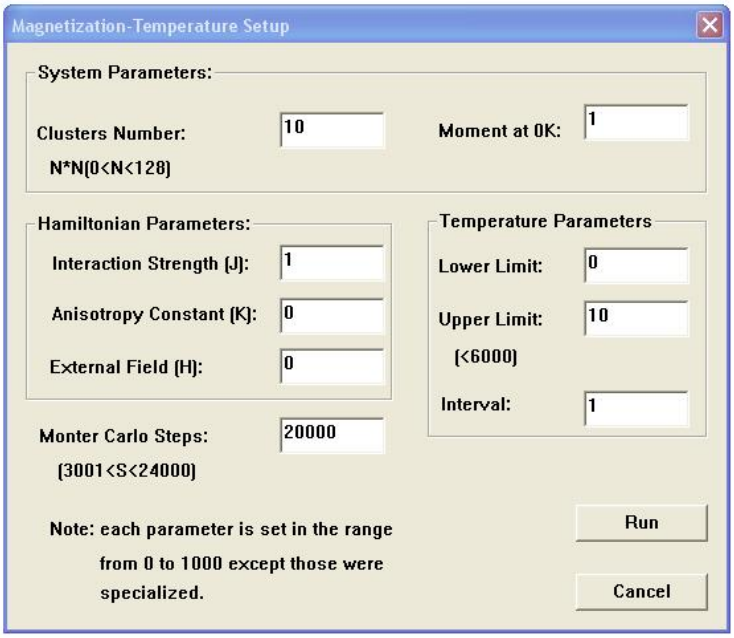

Figure Appx.-1 Set-up window for the investigation of the relationship between magnetization and temperature

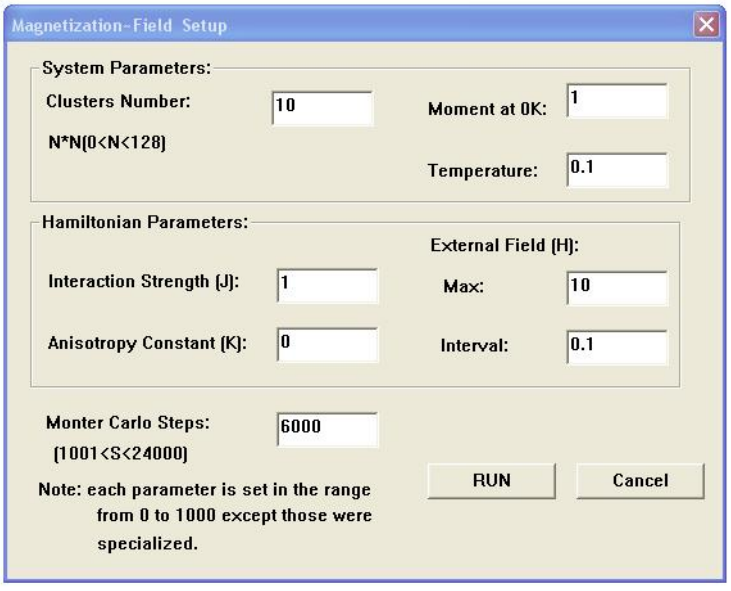

Figure Appx.-2 Set-up window for the investigation of the relationship between magnetization and applied field.

Appendix II Main Resource Code of Monte Carlo Simulation

```
// MagnSimView.cpp : implementation of the CMagnSimView class
//

#include "stdafx.h"
#include "MagnSim.h"

#include "MagnSimDoc.h"
#include "MagnSimView.h"

#include "MTSet.h"
#include "MHSet.h"
#include "math.h"
#include "fstream.h"

#ifdef _DEBUG
#define new DEBUG_NEW
#undef THIS_FILE
static char THIS_FILE[] = __FILE__;
```

```
#endif



double m_dMagAg[128][128][5];

CMTSet Mtdlg;

CMHSet Mhdlg;

CString str;


/////////////////////////////////////////////////////////////////////////////

// CMagnSimView


IMPLEMENT_DYNCREATE(CMagnSimView, CView)


BEGIN_MESSAGE_MAP(CMagnSimView, CView)

    //{{AFX_MSG_MAP(CMagnSimView)

    ON_COMMAND(IDM_MT_SETUP, OnMtSetup)

    ON_COMMAND(IDM_MH_SETUP, OnMhSetup)

    //}}AFX_MSG_MAP

    // Standard printing commands

    ON_COMMAND(ID_FILE_PRINT, CView::OnFilePrint)

    ON_COMMAND(ID_FILE_PRINT_DIRECT, CView::OnFilePrint)

    ON_COMMAND(ID_FILE_PRINT_PREVIEW, CView::OnFilePrintPreview)
```

```
END_MESSAGE_MAP()

////////////////////////////////////////////////////////////////////////////
// CMagnSimView construction/destruction

CMagnSimView::CMagnSimView()
{
	// TODO: add construction code here

}

CMagnSimView::~CMagnSimView()
{
}

BOOL CMagnSimView::PreCreateWindow(CREATESTRUCT& cs)
{
	// TODO: Modify the Window class or styles here by modifying
	//  the CREATESTRUCT cs

	return CView::PreCreateWindow(cs);
}
```

```
////////////////////////////////////////////////////////////////////////////
// CMagnSimView drawing

void CMagnSimView::OnDraw(CDC* pDC)
{
	CMagnSimDoc* pDoc = GetDocument();
	ASSERT_VALID(pDoc);
	// TODO: add draw code for native data here

}

////////////////////////////////////////////////////////////////////////////
// CMagnSimView printing

BOOL CMagnSimView::OnPreparePrinting(CPrintInfo* pInfo)
{
	// default preparation
	return DoPreparePrinting(pInfo);
}

void CMagnSimView::OnBeginPrinting(CDC* /*pDC*/, CPrintInfo* /*pInfo*/)
```

```
{
    // TODO: add extra initialization before printing
}

void CMagnSimView::OnEndPrinting(CDC* /*pDC*/, CPrintInfo* /*pInfo*/)
{
    // TODO: add cleanup after printing
}

/////////////////////////////////////////////////////////////////////////////
// CMagnSimView diagnostics

#ifdef _DEBUG
void CMagnSimView::AssertValid() const
{
    CView::AssertValid();
}

void CMagnSimView::Dump(CDumpContext& dc) const
{
    CView::Dump(dc);
}
```

```
CMagnSimDoc* CMagnSimView::GetDocument() // non-debug version is inline
{
	ASSERT(m_pDocument->IsKindOf(RUNTIME_CLASS(CMagnSimDoc)));
	return (CMagnSimDoc*)m_pDocument;
}
#endif //_DEBUG


/////////////////////////////////////////////////////////////////////////////
// CMagnSimView message handlers



//*****************************************************************//
//*****************************************************************//
//*****************************************************************//
//*****************************************************************//
//Randomnumber generating.....................
double CMagnSimView::m_dRandomNumber()
{
	double d=rand(); // Giving a random number between    0 and RAND_MAX;
	d=d/(double) RAND_MAX;    //Giving a random number between 0 and 1;
	return d;
```

```
}



//*************************************************************//
//*************************************************************//
//*************************************************************//
//*************************************************************//


//The Magnetization vs Temperature function
void CMagnSimView::OnMtSetup()  //The settiing up dialogue, showing the parameters should be input.

{
    // TODO: Add your command handler code here
    if(Mtdlg.DoModal()==IDOK)
    {
        CClientDC dc(this);
        ofstream outFile("MTData.dat", ios::ate);          // open a file to record data;
        double m_dDiffEnergy;          // Energy after a vibration;
        double m_dRawEnergy;          // Energy before a vibration;
```

```
        double m_dVarEnergy;        // Energy difference;
        double m_dtempT;            // Present temperature;
        double m_dMagnTemY;         // Magnetization in the direction of Y
axile;
        double m_dMagnTemX;         // Magnetization in the direction of X
axile;
        double m_dMagnTem;          // Magnetization at present temperature;
        double m_dVarAg;            // Switching angle after vibration;
        double m_dAllMagnTem;       // All Magnetizion  after S step calcluation,
for mean value calculation;
        double m_dAniAg;            // Anistropy Angle;

        int i;
        int j;
        int x;
        int y;
        int s;

        double top;
        double bottom;
        double left;
        double right;
```

```
        double randvalue;

//*************************************************************//
//Parameters Information.....................
//
    outFile<<"\n"<<"\n"<<"*********************************************
**********";
//          outFile<<"\n"<<"\n";
            outFile<<"Parameters Information......"<<"\n";
            outFile<<"Number of magmetic moment:"<<Mtdlg.m_iN<<"\n";
            outFile<<"Momement Value:"<<Mtdlg.m_dM<<"\n";
            outFile<<"J:"<<Mtdlg.m_dJ<<"\n";
            outFile<<"K:"<<Mtdlg.m_dK<<"\n";
            outFile<<"H:"<<Mtdlg.m_dH<<"\n";
            outFile<<"Monte Carlo Steps:"<<Mtdlg.m_iS<<"\n";

    outFile<<"T_UP:"<<Mtdlg.m_dUT<<"\t"<<"T_LOW:"<<Mtdlg.m_dLT<<"\t"<
<"T_Int:"<<Mtdlg.m_dIT<<"\n";
```

```
            outFile<<"Tem\t";
            outFile<<"Magn\n";




//*************************************************************//
//The Monte Carlo Performance
            //Cooling Down the system

      for(m_dtempT=Mtdlg.m_dUT;m_dtempT>Mtdlg.m_dLT;m_dtempT-=Mtdlg.m
_dIT)
            {
                  m_dMagnTemY=0;
                  m_dMagnTemX=0;
                  m_dMagnTem=0;
                  m_dAllMagnTem=0;

                  m_dAniAg=3.14159/4;    //The anisotropy angle is set in 3.14159/4 of
the direction of the external field;

//Initialization of the magentization and Anisotropic direction
                  for(i=0; i<Mtdlg.m_iN;++i)// direction of magnetization angle
```

```
                {
                    for(j=0;j<Mtdlg.m_iN;++j)
                        {
                            randvalue=m_dRandomNumber();
                            m_dMagAg[i][j][0]=3.14159*2*randvalue;
    //Testing.....
                            //m_dMagAg[i][j][0]=3.14159*((int)(8*randvalue))/4;
                        }
                }


//Judging the boundary and the possibility of fluctuation
                for(s=1;s<=Mtdlg.m_iS;++s)//Monte Carlo steps
                    {
                        for(i=0;i<Mtdlg.m_iN*Mtdlg.m_iN;++i)
                            {
                                //randomly selecting the moment
                                x=(int)(m_dRandomNumber()*(Mtdlg.m_iN));
                                y=(int)(m_dRandomNumber()*(Mtdlg.m_iN));
                                //judging the neighbor cluster with the considering of
system boundary
                                if(x==0)
```

```
top=m_dMagAg[Mtdlg.m_iN-1][y][0];
else
top=m_dMagAg[x-1][y][0];
if(x==(Mtdlg.m_iN-1))
bottom=m_dMagAg[0][y][0];
else
bottom=m_dMagAg[x+1][y][0];
if(y==0)
left=m_dMagAg[x][Mtdlg.m_iN-1][0];
else
left=m_dMagAg[x][y-1][0];
if(y==(Mtdlg.m_iN-1))
right=m_dMagAg[x][0][0];
else
right=m_dMagAg[x][y+1][0];

if(randvalue<0.5)
    m_dVarAg= 3.14159/64;
else
    m_dVarAg=-3.14159/64;
```

```
                    //Energy difference between two states

    m_dRawEnergy=m_dNormalMTJ()*pow(Mtdlg.m_dM,2)*(cos(m_dMagAg[x][
y][0]-left)+cos(m_dMagAg[x][y][0]-right)+cos(m_dMagAg[x][y][0]-top)+cos(m_d
MagAg[x][y][0]-bottom))+Mtdlg.m_dK*pow(Mtdlg.m_dM,2)*pow(cos(m_dAniAg
-m_dMagAg[x][y][0]),2)+Mtdlg.m_dH*Mtdlg.m_dM*sin(m_dMagAg[x][y][0]);

    m_dVarEnergy=m_dNormalMTJ()*pow(Mtdlg.m_dM,2)*(cos(m_dMagAg[x][y
][0]+m_dVarAg-left)+cos(m_dMagAg[x][y][0]+m_dVarAg-right)+cos(m_dMagAg[
x][y][0]+m_dVarAg-top)+cos(m_dMagAg[x][y][0]+m_dVarAg-bottom))+Mtdlg.m_
dK*pow(Mtdlg.m_dM,2)*pow(cos(m_dAniAg-m_dMagAg[x][y][0]-m_dVarAg),2)
+Mtdlg.m_dH*Mtdlg.m_dM*sin(m_dMagAg[x][y][0]+m_dVarAg);
                    m_dDiffEnergy=-(m_dVarEnergy-m_dRawEnergy);


                    //Judging the possibility of fluctuation
                    randvalue=m_dRandomNumber();
                    if(m_dDiffEnergy<=0)

    m_dMagAg[x][y][0]=m_dMagAg[x][y][0]+m_dVarAg;
                    else
if(m_dRandomNumber()<exp(-m_dDiffEnergy/(1.38*pow(10,-3)*m_dtempT)))
```

```
m_dMagAg[x][y][0]=m_dMagAg[x][y][0]+m_dVarAg;
                }

                //Demostration of the fluctuation of cluster
                if(s>3000 && (s%100==0))
                {
                    RedrawWindow();
                    //Displaying the animation of fluctuation
                    for(i=0;i<Mtdlg.m_iN;++i)// direction of magnetization angle
                        {
                            for(j=0;j<Mtdlg.m_iN;++j)
                                {

dc.Ellipse(48+i*20,48+j*20,52+i*20,52+j*20);
                                    dc.MoveTo(50+i*20,50+j*20);

dc.LineTo(50+i*20+(int)(10*cos(m_dMagAg[i][j][0])),50+j*20+(int)(10*sin(m_dMagAg[i][j][0])));
                                }
                        }
```

```
                }

                if(s>3000)
                {

                    for(i=0;i<Mtdlg.m_iN;++i)// direction of magnetization angle
                    {
                        for(j=0;j<Mtdlg.m_iN;++j)
                        {
                            //Calculating the magnetization value

    m_dMagnTemY+=sin(m_dMagAg[i][j][0]);

    m_dMagnTemX+=cos(m_dMagAg[i][j][0]);
                        }
                    }
                }
```

```
        m_dMagnTemY=m_dMagnTemY/(Mtdlg.m_iN*Mtdlg.m_iN);

        m_dMagnTemX=m_dMagnTemX/(Mtdlg.m_iN*Mtdlg.m_iN);

        m_dMagnTem=sqrt(m_dMagnTemY*m_dMagnTemY+m_dMagnTemX*m_dM
agnTemX);
                                m_dAllMagnTem+=m_dMagnTem;
                }

                        m_dMagnTem=m_dAllMagnTem/(Mtdlg.m_iS-3000);

                        //Output the data to screen and file
                        str.Format("Temperature: %.3f",m_dtempT);
                        dc.TextOut(10,500, str);
                        str.Format("Magnetizatin:%.3f",m_dMagnTem);
                        dc.TextOut(10,550, str);
                        outFile<<m_dtempT;
                        outFile<<"\t";
                        outFile<<m_dMagnTem;
                        outFile<<"\n";
```

```
                    UpdateData(FALSE);
            }
        }
}




//*************************************************************//
//*************************************************************//
//*************************************************************//
//*************************************************************//
//The Magnetization vs External Field function


void CMagnSimView::OnMhSetup()
{
    // TODO: Add your command handler code here
        if(Mhdlg.DoModal()==IDOK)
        {
            CClientDC dc(this);
            ofstream outFile("MHData.dat", ios::ate);
            double m_dDiffEnergy;
            double m_dRawEnergy;
```

```
double m_dVarEnergy;

double m_dtempH;

double m_dMagnFld;

double m_dVarAg;

double m_dAniAg;

double m_dMagnFldY;

double m_dMagnFldX;

double m_dAllMagnFld;


int i;

int j;

int x;

int y;

int s;


double top;

double bottom;

double left;

double right;

double randvalue;
```

```
//*************************************************************/
//Parameters Information.....................

      outFile<<"\n"<<"\n"<<"*********************************************
**********";
                outFile<<"\n"<<"\n";
                outFile<<"Parameters Information......"<<"\n";
                outFile<<"Number of magmetic moment:"<<Mhdlg.m_iN<<"\n";
                outFile<<"Momement Value:"<<Mhdlg.m_dM<<"\n";
                outFile<<"J:"<<Mhdlg.m_dJ<<"\n";
                outFile<<"K:"<<Mhdlg.m_dK<<"\n";
                outFile<<"H:"<<Mhdlg.m_dH<<"\n";
                outFile<<"H_Interval:"<<Mhdlg.m_dIH<<"\n";
                outFile<<"Monte Carlo Steps:"<<Mhdlg.m_iS<<"\n";
                outFile<<"T:"<<Mhdlg.m_dT<<"\n";
                outFile<<"Field\t";
                outFile<<"Magn\n";



//*************************************************************/
```

```
//*************************************************************//
//The Monte Carlo Performance
//Initialization of the magentization and Anisotropic direction
                for(i=0; i<Mhdlg.m_iN;++i)// direction of magnetization angle
                    {
                    for(j=0;j<Mhdlg.m_iN;++j)
                        {
                            randvalue=m_dRandomNumber();
                            //m_dMagAg[i][j][0]=3.14159*((int)(4*randvalue))/2;
                            m_dMagAg[i][j][0]=3.14159*2*randvalue;
                        }
                    }

                m_dAniAg=3.14159/4;




//*************************************************************/
//Magnetizating the system Part(I) 0-->H

     for(m_dtempH=0;m_dtempH<=Mhdlg.m_dH;m_dtempH+=Mhdlg.m_dIH)
                {
```

```
m_dMagnFld=0;
m_dMagnFldY=0;
m_dMagnFldX=0;
m_dAllMagnFld=0;



for(s=1;s<=Mhdlg.m_iS;++s)//Monte Carlo steps
{
    //scanning over all the moments
    for(i=0;i<Mhdlg.m_iN*Mhdlg.m_iN;++i)
    {
        //randomly selecting the moment
        x=(int)(m_dRandomNumber()*(Mhdlg.m_iN));
        y=(int)(m_dRandomNumber()*(Mhdlg.m_iN));
        //judging the neighbor cluster with the considering of
system boundary
        if(x==0)
        top=m_dMagAg[Mhdlg.m_iN-1][y][0];
        else
        top=m_dMagAg[x-1][y][0];
        if(x==(Mhdlg.m_iN-1))
        bottom=m_dMagAg[0][y][0];
```

```
else
bottom=m_dMagAg[x+1][y][0];
if(y==0)
left=m_dMagAg[x][Mhdlg.m_iN-1][0];
else
left=m_dMagAg[x][y-1][0];
if(y==(Mhdlg.m_iN-1))
right=m_dMagAg[x][0][0];
else
right=m_dMagAg[x][y+1][0];
//Giving an fluctuation angle
randvalue=m_dRandomNumber();
if(randvalue<0.5)
m_dVarAg=3.14159/64;
else
m_dVarAg=-3.14159/64;

//Energy difference between two states

m_dRawEnergy=m_dNormalMHJ()*pow(Mhdlg.m_dM,2)*(cos(m_dMagAg[x]
[y][0]-left)+cos(m_dMagAg[x][y][0]-right)+cos(m_dMagAg[x][y][0]-top)+cos(m_d
```

```
MagAg[x][y][0]-bottom))+Mhdlg.m_dK*pow(Mhdlg.m_dM,2)*pow(cos(m_dAniA
g-m_dMagAg[x][y][0]),2)-m_dtempH*Mhdlg.m_dM*sin(m_dMagAg[x][y][0]);

    m_dVarEnergy=m_dNormalMHJ()*pow(Mhdlg.m_dM,2)*(cos(m_dMagAg[x][
y][0]+m_dVarAg-left)+cos(m_dMagAg[x][y][0]+m_dVarAg-right)+cos(m_dMagAg
[x][y][0]+m_dVarAg-top)+cos(m_dMagAg[x][y][0]+m_dVarAg-bottom))+Mhdlg.m
_dK*pow(Mhdlg.m_dM,2)*pow(cos(m_dAniAg-m_dMagAg[x][y][0]-m_dVarAg),
2)-m_dtempH*Mhdlg.m_dM*sin(m_dMagAg[x][y][0]+m_dVarAg);
                    m_dDiffEnergy=-(m_dVarEnergy-m_dRawEnergy);
                    //Judging the possibility of fluctuation
                    if(m_dDiffEnergy<=0)
                    m_dMagAg[x][y][0]=m_dMagAg[x][y][0]+m_dVarAg;
                    else
if(m_dRandomNumber()<exp(-m_dDiffEnergy/(1.38*pow(10,-3)*(Mhdlg.m_dT))))
                    m_dMagAg[x][y][0]=m_dMagAg[x][y][0]+m_dVarAg;
                }



                //Displaying the animation of fluctuation
                if(s>100 && (s%10==0))
                {
```

```
                    RedrawWindow();
                    //Displaying the animation of fluctuation
                    for(i=0;i<Mhdlg.m_iN;++i)// direction of magnetization
angle
                        {
                            for(j=0;j<Mhdlg.m_iN;++j)
                                {

    dc.Ellipse(48+i*20,48+j*20,52+i*20,52+j*20);
                                        dc.MoveTo(50+i*20,50+j*20);

    dc.LineTo(50+i*20+(int)(10*cos(m_dMagAg[i][j][0])),50+j*20+(int)(10*sin(m
_dMagAg[i][j][0])));
                                }
                        }
                }

            if(s>100)
                {
                    for(i=0;i<Mhdlg.m_iN;++i)
                        for(j=0;j<Mhdlg.m_iN;++j)
```

```
                                {
                                    m_dMagnFldY+=sin(m_dMagAg[i][j][0]);
                                    m_dMagnFldX+=cos(m_dMagAg[i][j][0]);
                                }
                        }

    m_dMagnFldY=m_dMagnFldY/(Mhdlg.m_iN*Mhdlg.m_iN);

    m_dMagnFldX=m_dMagnFldX/(Mhdlg.m_iN*Mhdlg.m_iN);

    m_dMagnFld=sqrt(m_dMagnFldY*m_dMagnFldY+m_dMagnFldX*m_dMagn
FldX);
                                m_dAllMagnFld+=m_dMagnFld;
                    }
                    m_dMagnFld=m_dAllMagnFld/(Mhdlg.m_iS-100);
                    outFile<<m_dtempH;
                    outFile<<"\t";
                    outFile<<m_dMagnFld;
                    outFile<<"\n";
                }
```

```
//*********************************************************
//Magnetizating the system Part(II) H-->-H

    //for(m_dtempH=Mhdlg.m_dH;m_dtempH>-Mhdlg.m_dH;m_dtempH-=m_dDe
ltaH)

    for(m_dtempH=Mhdlg.m_dH;m_dtempH>-Mhdlg.m_dH;m_dtempH-=Mhdlg.
m_dIH)
            {

                m_dMagnFld=0;
                m_dMagnFldY=0;
                m_dMagnFldX=0;
                m_dAllMagnFld=0;
                for(s=1;s<=Mhdlg.m_iS;++s)//Monte Carlo steps
                {

                    //scanning over all the moments
                    for(i=0;i<Mhdlg.m_iN*Mhdlg.m_iN;++i)
                    {
                        //randomly selecting the moment
```

```
x=(int)(m_dRandomNumber()*(Mhdlg.m_iN));
y=(int)(m_dRandomNumber()*(Mhdlg.m_iN));
//judging the neighbor cluster with the considering of system boundary
if(x==0)
top=m_dMagAg[Mhdlg.m_iN-1][y][0];
else
top=m_dMagAg[x-1][y][0];
if(x==(Mhdlg.m_iN-1))
bottom=m_dMagAg[0][y][0];
else
bottom=m_dMagAg[x+1][y][0];
if(y==0)
left=m_dMagAg[x][Mhdlg.m_iN-1][0];
else
left=m_dMagAg[x][y-1][0];
if(y==(Mhdlg.m_iN-1))
right=m_dMagAg[x][0][0];
else
right=m_dMagAg[x][y+1][0];
//Giving an fluctuation angle
randvalue=m_dRandomNumber();
```

```
if(randvalue<0.5)
m_dVarAg=3.14159/64;
else
m_dVarAg=-3.14159/64;
//Energy difference between two states

m_dRawEnergy=m_dNormalMHJ()*pow(Mhdlg.m_dM,2)*(cos(m_dMagAg[x][y][0]-left)+cos(m_dMagAg[x][y][0]-right)+cos(m_dMagAg[x][y][0]-top)+cos(m_dMagAg[x][y][0]-bottom))+Mhdlg.m_dK*pow(Mhdlg.m_dM,2)*pow(cos(m_dAniAg-m_dMagAg[x][y][0]),2)-m_dtempH*Mhdlg.m_dM*sin(m_dMagAg[x][y][0]);

m_dVarEnergy=m_dNormalMHJ()*pow(Mhdlg.m_dM,2)*(cos(m_dMagAg[x][y][0]+m_dVarAg-left)+cos(m_dMagAg[x][y][0]+m_dVarAg-right)+cos(m_dMagAg[x][y][0]+m_dVarAg-top)+cos(m_dMagAg[x][y][0]+m_dVarAg-bottom))+Mhdlg.m_dK*pow(Mhdlg.m_dM,2)*pow(cos(m_dAniAg-m_dMagAg[x][y][0]-m_dVarAg),2)-m_dtempH*Mhdlg.m_dM*sin(m_dMagAg[x][y][0]+m_dVarAg);
m_dDiffEnergy=-(m_dVarEnergy-m_dRawEnergy);
//Judging the possibility of fluctuation
if(m_dDiffEnergy<=0)
m_dMagAg[x][y][0]=m_dMagAg[x][y][0]+m_dVarAg;
else
```

```
if(m_dRandomNumber()<exp(-m_dDiffEnergy/(1.38*pow(10,-3)*(Mhdlg.m_dT))))
                        m_dMagAg[x][y][0]=m_dMagAg[x][y][0]+m_dVarAg;



                    }

                    //Displaying the animation of fluctuation
                    if(s>100 && (s%10==0))
                    {
                        RedrawWindow();
                        //Displaying the animation of fluctuation
                        for(i=0;i<Mhdlg.m_iN;++i)// direction of magnetization
angle
                            {
                                for(j=0;j<Mhdlg.m_iN;++j)
                                    {


    dc.Ellipse(48+i*20,48+j*20,52+i*20,52+j*20);
                                                dc.MoveTo(50+i*20,50+j*20);


    dc.LineTo(50+i*20+(int)(10*cos(m_dMagAg[i][j][0])),50+j*20+(int)(10*sin(m
_dMagAg[i][j][0])));
```

```
                                    }
                                }
                            }


                        if(s>100)
                            {
                                for(i=0;i<Mhdlg.m_iN;++i)
                                    for(j=0;j<Mhdlg.m_iN;++j)
                                        {
                                            m_dMagnFldY+=sin(m_dMagAg[i][j][0]);
                                            m_dMagnFldX+=cos(m_dMagAg[i][j][0]);
                                        }
                            }

        m_dMagnFldY=m_dMagnFldY/(Mhdlg.m_iN*Mhdlg.m_iN);

        m_dMagnFldX=m_dMagnFldX/(Mhdlg.m_iN*Mhdlg.m_iN);

        m_dMagnFld=sqrt(m_dMagnFldY*m_dMagnFldY+m_dMagnFldX*m_dMagn
FldX);
                                    m_dAllMagnFld+=m_dMagnFld;
```

```
                    }
                    m_dMagnFld=m_dAllMagnFld/(Mhdlg.m_iS-100);
                    outFile<<m_dtempH;
                    outFile<<"\t";
                    outFile<<m_dMagnFld;
                    outFile<<"\n";

            }
//*************************************************************
//Magnetizating the system Part(II) H-->-H

     //for(m_dtempH=Mhdlg.m_dH;m_dtempH>-Mhdlg.m_dH;m_dtempH-=m_dDe
ltaH)

     for(m_dtempH=-Mhdlg.m_dH;m_dtempH<=Mhdlg.m_dH;m_dtempH+=Mhdlg
.m_dIH)
                {

                    m_dMagnFld=0;
                    m_dMagnFldY=0;
                    m_dMagnFldX=0;
                    m_dAllMagnFld=0;
```

```
for(s=1;s<=Mhdlg.m_iS;++s)//Monte Carlo steps
{

    //scanning over all the moments
    for(i=0;i<Mhdlg.m_iN*Mhdlg.m_iN;++i)
    {
        //randomly selecting the moment
        x=(int)(m_dRandomNumber()*(Mhdlg.m_iN));
        y=(int)(m_dRandomNumber()*(Mhdlg.m_iN));
        //judging the neighbor cluster with the considering of
system boundary
        if(x==0)
        top=m_dMagAg[Mhdlg.m_iN-1][y][0];
        else
        top=m_dMagAg[x-1][y][0];
        if(x==(Mhdlg.m_iN-1))
        bottom=m_dMagAg[0][y][0];
        else
        bottom=m_dMagAg[x+1][y][0];
        if(y==0)
        left=m_dMagAg[x][Mhdlg.m_iN-1][0];
        else
```

```
left=m_dMagAg[x][y-1][0];
if(y==(Mhdlg.m_iN-1))
right=m_dMagAg[x][0][0];
else
right=m_dMagAg[x][y+1][0];
//Giving an fluctuation angle
randvalue=m_dRandomNumber();
if(randvalue<0.5)
m_dVarAg=3.14159/64;
else
m_dVarAg=-3.14159/64;
//Energy difference between two states
```

```
m_dRawEnergy=m_dNormalMHJ()*pow(Mhdlg.m_dM,2)*(cos(m_dMagAg[x][y][0]-left)+cos(m_dMagAg[x][y][0]-right)+cos(m_dMagAg[x][y][0]-top)+cos(m_dMagAg[x][y][0]-bottom))+Mhdlg.m_dK*pow(Mhdlg.m_dM,2)*pow(cos(m_dAniAg-m_dMagAg[x][y][0]),2)-m_dtempH*Mhdlg.m_dM*sin(m_dMagAg[x][y][0]);
```

```
m_dVarEnergy=m_dNormalMHJ()*pow(Mhdlg.m_dM,2)*(cos(m_dMagAg[x][y][0]+m_dVarAg-left)+cos(m_dMagAg[x][y][0]+m_dVarAg-right)+cos(m_dMagAg[x][y][0]+m_dVarAg-top)+cos(m_dMagAg[x][y][0]+m_dVarAg-bottom))+Mhdlg.m
```

```
_dK*pow(Mhdlg.m_dM,2)*pow(cos(m_dAniAg-m_dMagAg[x][y][0]-m_dVarAg),
2)-m_dtempH*Mhdlg.m_dM*sin(m_dMagAg[x][y][0]+m_dVarAg);
                        m_dDiffEnergy=-(m_dVarEnergy-m_dRawEnergy);
                        //Judging the possibility of fluctuation
                        if(m_dDiffEnergy<=0)
                        m_dMagAg[x][y][0]=m_dMagAg[x][y][0]+m_dVarAg;
                        else
if(m_dRandomNumber()<exp(-m_dDiffEnergy/(1.38*pow(10,-3)*(Mhdlg.m_dT))))
                        m_dMagAg[x][y][0]=m_dMagAg[x][y][0]+m_dVarAg;



                    }
/*********************************************************************/
                    //Displaying the animation of fluctuation
                    if(s>100 && (s%10==0))
                    {
                        RedrawWindow();
                        //Displaying the animation of fluctuation
                        for(i=0;i<Mhdlg.m_iN;++i)// direction of magnetization
angle
                            {
                                for(j=0;j<Mhdlg.m_iN;++j)
```

```
                                        {

    dc.Ellipse(48+i*20,48+j*20,52+i*20,52+j*20);

                                                dc.MoveTo(50+i*20,50+j*20);

    dc.LineTo(50+i*20+(int)(10*cos(m_dMagAg[i][j][0])),50+j*20+(int)(10*sin(m
_dMagAg[i][j][0])));
                                        }
                                    }
                                }



                            if(s>100)
                                {
                                    for(i=0;i<Mhdlg.m_iN;++i)
                                        for(j=0;j<Mhdlg.m_iN;++j)
                                            {
                                                m_dMagnFldY+=sin(m_dMagAg[i][j][0]);
                                                m_dMagnFldX+=cos(m_dMagAg[i][j][0]);
                                            }
                                }
```

```
        m_dMagnFldY=m_dMagnFldY/(Mhdlg.m_iN*Mhdlg.m_iN);


        m_dMagnFldX=m_dMagnFldX/(Mhdlg.m_iN*Mhdlg.m_iN);


        m_dMagnFld=sqrt(m_dMagnFldY*m_dMagnFldY+m_dMagnFldX*m_dMagn
FldX);
                                m_dAllMagnFld+=m_dMagnFld;
                }
                m_dMagnFld=m_dAllMagnFld/(Mhdlg.m_iS-100);
                outFile<<m_dtempH;
                outFile<<"\t";
                outFile<<m_dMagnFld;
                outFile<<"\n";


        }
}
}



/*************************************************************************/
/*************************************************************************/
/*************************************************************************/
```

```
//Normal Distribution of exchange interaction parameter.....
//In this function, J will be considered as value with normal distribution. So variation,
cutting radius, fluctuation ratio will be given a default value.

double CMagnSimView::m_dNormalMTJ()
{

    int i;
    double d;
    double dJ;
    double rcut;
    double rflu=0.1;
    double var=0.15;


    rcut=rflu*Mtdlg.m_dJ;

    do
    {
     d=0;
     dJ=0;
     for(i=0;i<48;++i)
```

```
        {
                d+=m_dRandomNumber();
        }
       dJ=Mtdlg.m_dJ+(d-24)*var;
      }
      while(fabs(Mtdlg.m_dJ-dJ)>rcut);

      return dJ;

}

double CMagnSimView::m_dNormalMHJ()
{




      int i;
      double d;
      double dJ;
      double rcut;
      double rflu=0.1;
      double var=0.15;
```

```
    rcut=rflu*Mtdlg.m_dJ;


    do
    {
     d=0;
     dJ=0;
     for(i=0;i<12;++i)
       {
            d+=m_dRandomNumber();
       }
     dJ=Mhdlg.m_dJ+(d-6)*var;
    }
    while(fabs(Mhdlg.m_dJ-dJ)>rcut);


    return dJ;


}
```